Università degli Studi di Padova
Dipartimento di Scienze Chimiche
Corso di Laurea Magistrale in Scienza dei Materiali

TESI DI LAUREA MAGISTRALE

Development of NbTi and Nb_3Sn thin films for innovative superconducting axion haloscopes

Relatore: Dott. Cristian Pira
Controrelatore: Prof. Davide De Salvador

Laureando: Alessandro Salmaso

Matricola: 1242454

anno accademico 2021 / 2022

Abstract

The axion is a hypothetical particle introduced as solution to the strong CP problem; its mass is predicted to be in the range of $10 - 10^3$ μeV. Due to its weak interaction it is a candidate cold dark matter particle. This particle can be detected by resonant cavities, or haloscopes, immersed in an intense static magnetic field and tuned to the axion frequency - in the microwave range - exploiting the axion-photon coupling described by the inverse Primakoff effect. Superconducting (SC) materials offer the possibility to enhance the sensitivity of the resonator because of their higher quality factor in a magnetic field compared to copper. The ones eligible for this application are the type-II superconductors, which can sustain high magnetic fields - up to several teslas - without breaking the SC state.

The objective of this work is the development of NbTi and Nb_3Sn films for SC haloscopes coated via magnetron sputtering. The Nb_3Sn critical magnetic field of 30 T makes it a suitable replacement for NbTi, whose critical field is 12 T.

For NbTi, several tests on planar samples have been made to investigate some deposition parameters. The obtained composition is around 50 % in weight of Ti, which is in the desired range to have the maximum upper critical magnetic field. Copper interdiffusion in the film has been addressed with a niobium diffusion barrier. Four copper haloscopes (a total of eight half cells) have been coated with a 2.5 μm NbTi film, one of which also with the Nb diffusion barrier of 1 μm. The cavity of nominal frequency 7GHz have been tested in a cryogenic environment and immersed in a magnetic field up to 11 T. The axion-photon coupling factor resulted, at 8 T and 4.2 K, one order of magnitude higher than a copper cavity. The quality factor of the resonator results limited by the uncoated part of the cavity. XRD and third harmonic AC magnetic susceptibility revealed the presence of a single SC phase.

An ultra high vacuum deposition chamber dedicated to Nb_3Sn has been set up to operate at the high temperature required for the formation of the Nb_3Sn phase. XRD and EDS analysis confirmed the presence of the SC phase. The composition of the films is sub-stoichiometric: about 22 atomic % of Sn. A thermal treatment of the sample at different temperatures and a higher deposition pressure demonstrated to increase the critical temperature. The Nb diffusion barrier has been implemented also for Nb_3Sn to reduce the Cu content in the film. It showed to increase the composition, by blocking the Sn diffusion towards the substrate, and the critical temperature. Moreover, it allows to obtain higher T_c at a lower deposition temperature compared to the copper substrate. This is a noticeable result in the optics of SRF cavities, which cannot sustain high temperature treatments.

Abstract (italiano)

Gli assioni sono particelle teorizzate per spiegare la mancata osservazione della violazione della simmetria CP nell'interazione forte, anche noto come *strong CP problem.* Il range di massa previsto è $10 - 10^3$ μeV. Sono anche considerati come potenziali costituenti della materia oscura viste le deboli interazioni di cui risentono. Queste particelle possono essere rivelate con cavità risonanti, o aloscopi, immerse in un forte campo magnetico e impostate sulla frequenza dell'assione, che ricade nel range delle microonde. Questo è possibile grazie all'accoppiamento assione-fotone descritto dall'effetto Primakoff inverso. I materiali superconduttori possono notevolmente aumentare la sensibilità del risonatore grazie all'elevato fattore di qualità, anche in alto campo magnetico, rispetto al rame. I materiali adatti a questa applicazione sono i superconduttori di tipo II, che possono mantenere lo stato superconduttivo anche in presenza di campi magnetici di diversi tesla.

L'obiettivo di questa tesi è lo sviluppo di film di NbTi e Nb_3Sn depositati via *magnetron sputtering* per aloscopi superconduttivi. Il campo magnetico critico di 30 T del Nb_3Sn , lo rende un possibile sostituto del NbTi il cui campo critico è di 12 T.

Riguardo la parte sul NbTi, sono stati effettuati diversi test su campioni planari per investigare alcuni parametri di deposizione. La composizione ottenuta risulta essere attorno al 50 % in peso di Ti, quindi nel range ideale per avere il più alto campo magnetico critico. La diffusione del rame nel film è stata mitigata con un barriera di Nb. Quattro aloscopi (per un totale di otto semicelle) sono state depositate con un film di NbTi dello spessore di 2.5 μm; una è stata depositata anche con una barriera di Nb di 1 μm. La cavità da 7 GHz è stata testata in ambiente criogenico e in campo magnetico fino a 11 T. Il fattore di accoppiamento assione-fotone risulta essere, a 8 T e 4.2 K, un ordine di grandezza superiore al rame. Il fattore di qualità risulta limitato dalle zone non ricoperte dal film SC. Analisi XRD e di suscettività magnetica AC alla terza armonica mostrano la presenza di un'unica fase superconduttiva.

La camera da ultra alto vuoto dedicata al Nb_3Sn è stata ottimizzata per lavorare alle alte temperature necessarie per la formazione della fase corretta. Analisi XRD ed EDS hanno confermato la presenza della fase Nb_3Sn . La composizione dei film ottenuti è intorno al 22 % atomico di Sn. Trattamenti termici a diverse temperature e alte pressioni di deposizione hanno l'effetto di aumentare la temperatura critica. La barriera di Nb è stata implementata per ridurre la diffusione di rame nel film. Quest'ultima ha l'effetto di aumentatre il contenuto di Sn, perchè blocca la sua diffusione verso il substrato, e temperatura critica. Inoltre, permette di ottenere T_c più alte che su rame ma a più bassa temperatura, questo risultato è di notevole interesse per le cavità SRF in quanto non possono subire trattamenti termici ad elevata temperatura.

For my beloved Veronica.

Contents

1

Introduction

There are many intriguing open questions in physics that occupy and fascinate the minds of countless researchers. The Standard Model of particle physics encloses three of the four forces, or interactions, that govern the universe: electromagnetism, weak and strong - gravity is not included. It is possibly one of the most famous theories in physics and has been capable of successful predictions, but it presents gaps that need to be filled in order to be complete, one of which is the strong CP problem, related to the CP symmetry violation in the strong force. Cosmological observations indicate that an invisible density of matter is present and actually constitutes 26% of the total energy density of the universe, while ”ordinary” matter accounts for just 5%. This is called Dark Matter, due to its non-interaction with light, which makes it invisible to our eyes and challenging to detect.

A solution to both these problems may be a particle named axion. The axion has been introduced as a solution to the strong CP problem by Peccei and Quinn in 1977 [1], but due to weekly coupling properties, it is also a dark matter particle candidate. So if the axion is discovered, it would be a double win.

The most promising experiments focusing on axion detection, like the ADMX collaboration and the QUAX experiment [2, 3], make use of microwave resonant cavities called haloscopes placed in a high magnetic field to enhance the axion-photon coupling and probe the axion's parameter space in the mass range of μeV. Such resonators are commonly made of high purity copper, but their performance can be improved by exploiting the excellent yet uncommon properties of superconductors.

Superconductors (SC) are a class of materials that is becoming more and more important in modern society. They are famously used in high energy physics and in quantum computing, but also in medical devices and in the transportation industry [4–8]. New superconducting materials are being investigated to overcome the intrinsic limits reached in particle accelerators, used in high energy physics to explore the universe at the sub-atomic scale. In the framework of axion detection experiments, superconducting resonant cavities are able to reach higher quality factors with respect to the pure copper ones, achieving better sensitivity. But they come with a challenge: not every SC is suitable for this task. The high static magnetic fields used limit the choice of the material to the ones that have a high critical magnetic field, which represent the maximum value of magnetic field a superconductor can withstand. Over this threshold, the material returns to the normal conducting state - even at low temperatures - with drastic consequences on the performance. The materials feasible for this application are the so called type-II superconductors, among which niobium - the workhorse SC for accelerating cavities - appears, but having a low critical field (about 0,4 T) it is actually not a good choice. A possible material is the Nb-Ti alloy, with a critical field of approximately 12 T. This has already been proven to give good results by enhancing the quality factor of the resonator by almost an order of magnitude when operated at 2 T [9]. Another choice is Nb_3Sn that has a critical field more than double that of NbTi: about 30 T, allowing to reach even higher sensitivity. This material is also being studied for accelerating cavities. With respect to niobium, it could provide twice the accelerating field and it would not require liquid helium thanks to its "high" transition temperature - dramatically reducing the cryogenics costs.

1.1 Objectives

In this work, two superconducting materials have been developed for coating axion haloscopes via DC magnetron sputtering. A more mature research activity is that of NbTi, that aims at optimizing the deposition process and the performance of the device. A new line of research regarding Nb_3Sn has been opened with a new dedicated Ultra High Vacuum coating system designed in this work. The two researches are in the framework of a recent INFN collaboration: SAMARA (Superconducting Alternative Materials for Accelerating cavities and haloscope Resonators for Axions). Moreover, the Nb_3Sn line of research is also inserted in the international project I.FAST (Innovation Fostering in Accelerator Science and Technology), specifically work package 9 [10], focused on superconducting accelerating cavities technologies. The knowledge acquired in the production of Nb_3Sn coatings is applicable in both projects, allowing for a synergy in this work.

2

Superconductivity and SRF basis

In this chapter an overview of superconductivity fundamentals will be given, drawing attention on the key properties and on the superconducting (SC) materials. Also, the basic behavior of normal conductors and superconductors in radio-frequency fields (SRF) will be outlined. General references for this chapter are [11–13].

2.1 Introduction to superconductivity

Heike Kamerlingh-Onnes successfully liquefied helium in 1908, securing himself the 1913 Nobel Prize in Physics. He was, at that time, the director of the Low Temperature Laboratory at the University of Leiden, Netherlands. A more than appropriate name since the boiling point of He at atmospheric pressure is $4,2\ K$, the lowest of all gases, and can be reduced by decreasing the pressure. This ended the race to the liquefaction of gasses, started long before with the making of liquid chlorine, in 1823, by Michael Faraday [14].

The discovery of superconductivity is strictly related to liquid helium and it is attributed, again, to Onnes (1911). His research focused on the properties of matter at low temperatures. In particular, on the electrical resistance of metals, whose behaviour was experimentally determined down to $\sim 10\ K$ and only theorized at lower temperatures.

2.1.1 Zero electrical resistance

Materials manifest a SC behaviour below their critical temperature T_c. Their first observed property is the disappearance of the DC electrical resistance in purified mercury as it passes its T_c of about $4\ K$, illustrated in figure 2.1. Most pure metals present a T_c below $10\ K$, the highest being that of niobium $\simeq 9,3\ K$. This is the reason why the cryogenic technology developed by Onnes has been the cornerstone for superconductivity. In the following years, the same behaviour has been found in many other metals like lead and tin, with T_c of approximately $7,2\ K$ and $3,7\ K$ respectively, and later also in many alloys.

A strong implication of this phenomenon is that in superconductors a permanent

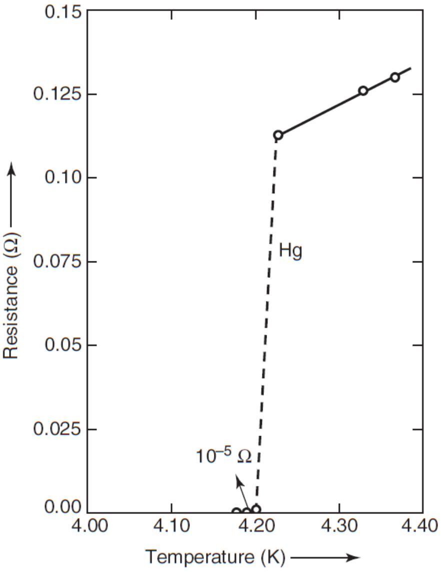

Figure 2.1: *Fall of DC resistance in mercury reported by Onnes, from* [13].

current can subsist but, having a null resistivity ρ, such current can be generated via induction in SC rings. It is important to underline the intrinsic difficulty in measuring a null quantity, or its infinite inverse (if $\rho \to 0$ then $\sigma = \rho^{-1} \to \infty$). Since measuring the decay time τ of a permanent current results, effectively, in a *non change*, it is possible to set a lower bound for τ and an upper bound for the resistivity by appealing to the instrumental resolution. In a ring of pure aluminium, via an inductive method, it is found: $\tau_{Al} > 10^{13}\ s \sim 10^{6}\ years$ and $\rho_{Al} < 10^{-25}\ \Omega m$ (more or less 17 orders of magnitude lower than the resistivity of gold at room temperature). These values, although variable when using more sensitive technologies, justify the treating of the DC electrical resistance of SC materials as *zero* [11]. As it will be discussed in section 2.5, when an AC electrical field is applied other phenomena occur and at high frequency (namely above radio frequency) a surface resistance appears and become relevant.

2.1.2 Perfect diamagnetism

Another property of SC materials is that of the Meissner effect, observed by Meissner and Ochsenfeld in 1933 [15]. If a magnetic field H is applied to a superconductor when in the normal-conducting (NC) state, it would be completely expelled when transitioning to the SC state. This means that inside the material

$$B = \mu_0(H + M) = 0 \Rightarrow M = -M \tag{2.1}$$

so the magnetic susceptibility is

$$\chi = \frac{dM}{dH} = -1 \tag{2.2}$$

where M is the magnetization field. This property of the SC state is defined as perfect diamagnetism: $\chi = -1$.

The Meissner effect is different from what it would be observed with a hypothetical *ideal conductor*, i.e. a material characterized by just zero resistivity. Applying a magnetic field to such material before or after cooling it below a certain temperature at which it has $\rho = 0$, and then removing it, leads to different results: the former being that of trapped flux and the latter of no trapped flux. Instead, with a SC material it is observed the same result in both cases: spontaneous super-currents appear in the surface of the sample causing a magnetization opposite to H and ultimately, the magnetic field expulsion. Thus, superconductors in the Meissner state do not resent of the temporal sequence of magnetic field application.

2.1.3 Type I and type II superconductors

It is important now to distinguish between the two classes of superconductors and to define their thermodynamic state.

The Meissner state is stable up to a critical value of H_c, above which, materials like mercury and lead return to the NC state. These are called type-I superconductors.

There are other materials where the SC state does not break down in a magnetic field higher than H_{c1} (lower critical field): they remain superconducting but allow a partial penetration of magnetic flux trough vortexes. This is called the mixed state, or Shubnikov state, attributed to type-II superconductors, and was predicted by Abrikosov in 1957. When increasing the intensity of H, the magnetic flux penetrates more and more until it reaches the upper critical field H_{c2} at which full penetration is achieved and the SC state breaks down. In figure 2.2 is illustrated the behaviour of both types of superconductors.

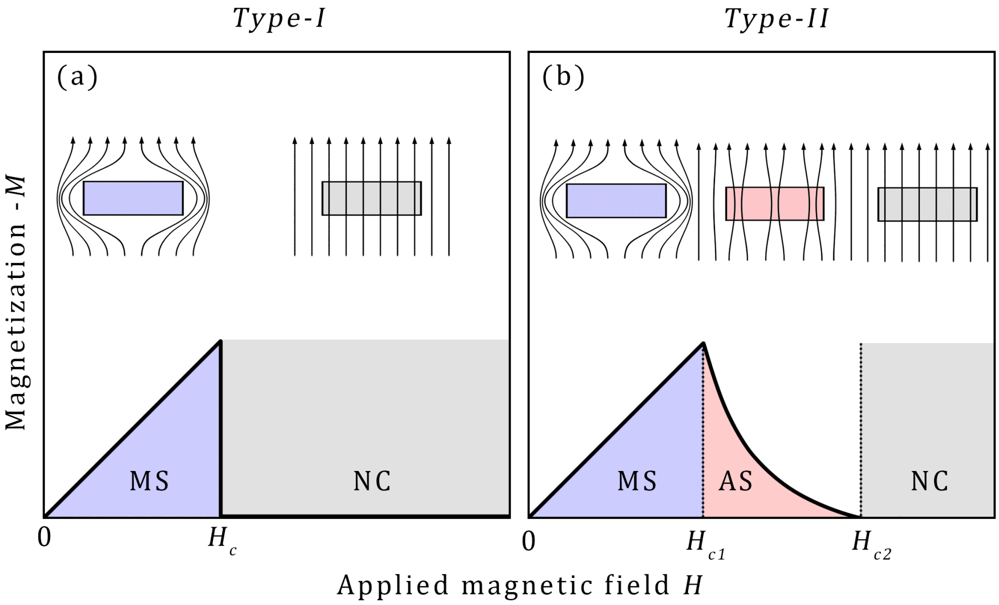

Figure 2.2: *(a) describes the behaviour of type-I superconductors: the Meissner state (MS) is table below H_c. (b) shows the type-II behaviour: above H_{c1} the material switches from the MS to the Shubnikov state (SS) that allows partial magnetic flux penetration up to H_{c2} where it becomes NC. Note that the vertical axis is inverted so it represent a negative magnetization.*

Only few materials are Type-I and the majority of them are elemental pure metals such as mercury, lead, tin and aluminium. Examples of Type-I SC compounds are heavily boron-doped silicon carbide SiC:B ($T_c \simeq 1,4\ K$) and $TaSi_2$ ($T_c \simeq 0,4\ K$) [16, 17]. Type-II superconductors are far more common: they are mainly compounds and alloys like the A15 materials and the Nb-Ti alloy, described more in depth in sections 3.2 and 3.1. Examples of pure metals are vanadium ($T_c \simeq 5,5\ K$) and the already mentioned niobium. A more formal definition of the two types of superconductors, based on two crucial parameters of superconductors, will be given in section 2.3.

2.2 Thermodynamic aspects of the SC state

Since the SC state is a thermodynamic state, it is useful to calculate simple relations between measurable quantities by analyzing, as always, the Gibbs' free energy. In a magnetic field

$$dG(H,T) = -\mu_0 M(H,T)dH \tag{2.3}$$

Integrating this relation to calculate the difference in free energy between the NC (G_n) and SC (G_s) state for Type-I and exploiting that in NC $\chi \ll 1 \Rightarrow G_n(H_c,T) = G_n(0,T)$ it is obtained

$$\Delta G = G_n(0,T) - G_s(0,T) = \frac{\mu_0}{2} H_c^2(T) \tag{2.4}$$

The meaning of a positive ΔG is that it represent a *condensation energy* since the energy density in the SC state is lower. Empirically it is possible to calculate the temperature dependence of H_c for type-I SC, it is found to be

$$H_c(T) = H_c(0)\left(1 - \frac{T}{T_c}\right)^2 \tag{2.5}$$

In figure 2.3 is reported a schematic representation of the two critical fields in function of the temperature for a type-II superconductor.

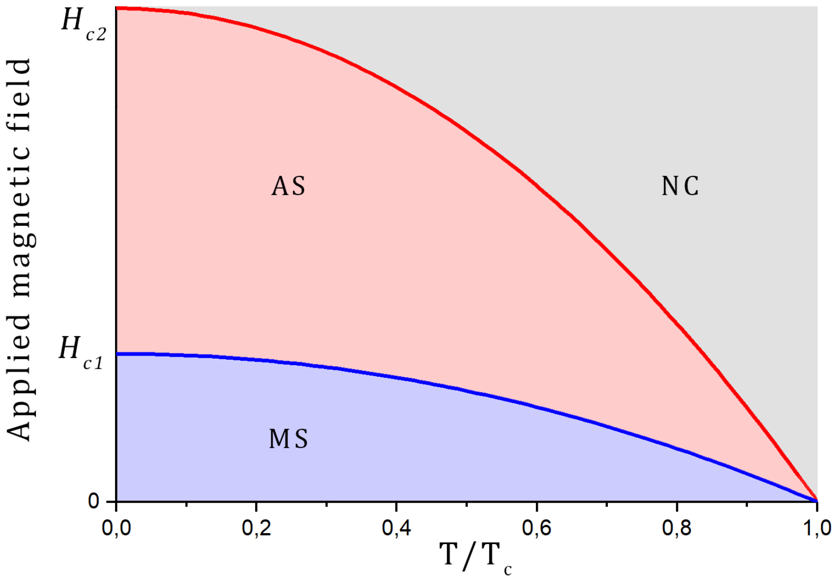

Figure 2.3: *Pictorial representation of the temperature dependence of the critical fields B_{c1} and B_{c2} for a type-II superconductor. For a type-I the graph is similar, with just the Meissner state (MS) below the critical field H_c.*

Also, the variation of entropy can be easily calculated

$$\Delta S = S_n(0,T) - S_s(0,T) = -\mu_0 H_c(0)\frac{dH_c}{dT} \tag{2.6}$$

Since $\frac{dH_c}{dT} < 0$, the entropy of the SC state is lower than the NC state. The BCS theory allows to explain such greater order with the formation of Cooper pairs and the phase coherence of the wavefunction.

This leads to the heat capacity at T_c

$$\Delta C = C_n(T_c) - C_s(T_c) = \mu_0 T_c \left(\frac{dH_c}{dT}\right)^2_{T_c} \tag{2.7}$$

Again, a positive quantity but this time, at the transition temperature, it defines a discontinuity. This is true in low-T_c superconductors, the ones that are well described by the BCS theory. In high-T_c SC materials, with $T_c > 77\ K$ (the boiling point of nitrogen), like cuprates, the heat capacity shows no discontinuity with a maximum at the critical temperature.

It is possible to conclude that, since at $T = T_c$ $\Delta S = 0$ and $\Delta C \neq 0$ for low-T_c superconductors, the SC transition can be treated as a 2^{nd}-order phase transition.

2.3 London equations and Ginzburg-Landau theory

Gorter and Casimir were the first to propose a simple model that describes the zero resistivity and perfect diamagnetism phenomena of superconductors. It is the two fluid model and it is based on the separation of the charge carriers into two electron fluid: one normal and the other superconducting with density n_n and n_s, respectively, such that: $n_0 = n_n + n_s$. The temperature dependence, shown in figure 2.4, is as follow

$$n_s = n_0\left(1 - \frac{T^4}{T_c^4}\right) \tag{2.8}$$

Based on this model, the current density attributed to n_s is: $\mathbf{J_s} = -n_s e\mathbf{v}$.

2.3.1 London equations

The Meissner effect is commonly described with the London equations, developed by the Fritz and Heinz London brothers in 1935 [18]. The magnetic field expulsion can only be caused by surface electrical currents, but in order to avoid the need of an infinite density of SC carriers, they would penetrate in the material to a certain depth λ_L

$$\lambda_L = \sqrt{\frac{m_e}{\mu_0 n_s e^2}} \tag{2.9}$$

where m_e is the electron mass, e its charge and n_s is the SC carriers density.

The first London equation describes the zero resistivity property

$$\frac{d\mathbf{J_s}}{dt} = \frac{n_s e^2}{m_e}\mathbf{E} \tag{2.10}$$

this implies that there is no need of an electrical field to sustain a current, since supercurrents do not decay: $\dot{\mathbf{J}}_\mathbf{s} = 0$.

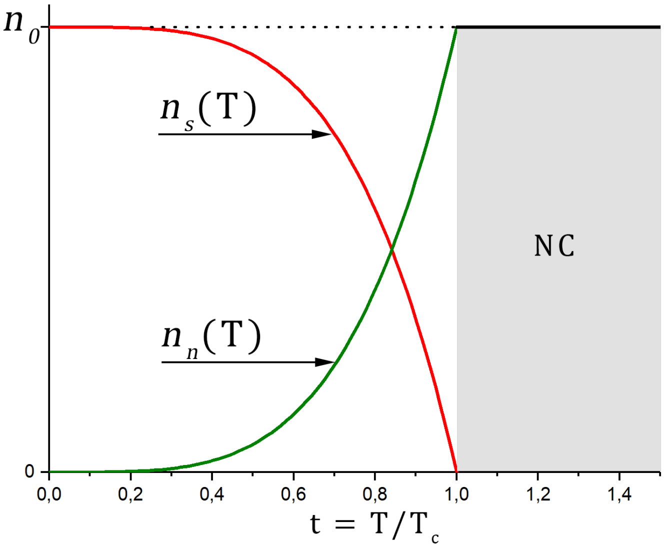

Figure 2.4: *Temperature dependence of normal n_n and superconducting n_s charge carriers density in the two fluid model. For $t < 1$, n_s varies from zero to one. For $t > 1$, all the carriers are in the NC state: $n_n = n_0$.*

The second London equation correlates the $\mathbf{J_s}$ to the magnetic field penetrating the material's surface $\mathbf{B}$

$$\nabla \times \mathbf{J_s} = -\frac{n_s e^2}{m_e}\mathbf{B} = -\frac{1}{\mu_0 \lambda_L^2}\mathbf{B} \tag{2.11}$$

Using Maxwell's equation $\nabla \times \mathbf{B} = \mu_0 \mathbf{J_s}$, and reducing the problem to a simple mono dimensional case, the solution for $B(z)$ is

$$B(z) = B_0 e^{-\frac{z}{\lambda_L}} \tag{2.12}$$

where B_0 is correlated to the applied field H through $B_0 = \mu_0 H$. The London penetration depth represents the screening length for the magnetic field, figure 2.5 show this remark that is the core of the Meissner effect.

The London equations are a set of phenomenological tools, based on Maxwell equations.

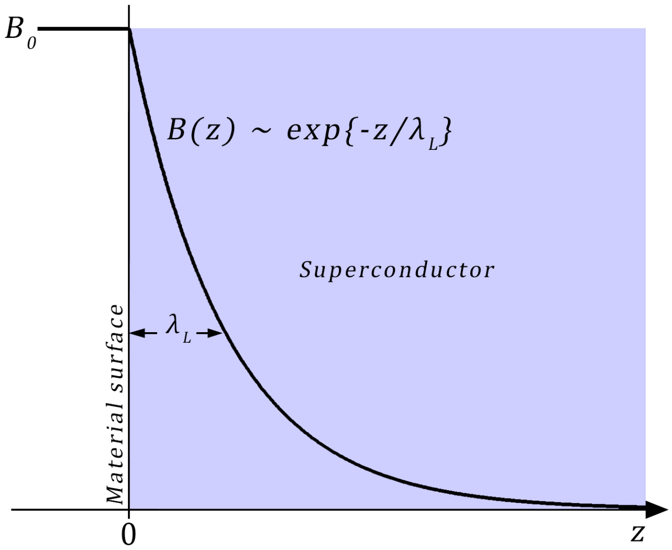

Figure 2.5: *Penetration of the magnetic field in a superconductor. λ_L is the London penetration depth, the screening length of $B_0 = \mu_0 H$. This phenomenon is the core of the Meissner effect.*

2.3.2 Ginzburg-Landau coherence length

The Ginzburg-Landau (GL) theory, published in 1950, expands the London theory by introducing a spatial variation of the Gibbs free energy and a macroscopic wave-function that describes the SC state.

The Gibbs free energy of the SC state, G_s, can be written as a Taylor series of an order parameter $|\Psi(\mathbf{r})|^{\mathbf{2}}$ that approaches zero continuously for $T \to T_c$. Hence, expanding near T_c

$$G_s(T, |\Psi|^2) = G_n(T) + \alpha|\Psi|^2 + \tfrac{1}{2}\beta|\Psi|^4 + \dots \tag{2.13}$$

where G_n is the free energy of the normal state, that is equal to G_s when $\Psi = 0$. The coefficient β should be positive to have a minimum of G_s at a finite value of Ψ. In order to have a stable SC state: $\alpha < 0$ for $T << T_c$, so that $G_s < G_n$ and the minimum is at a non-zero value of the order parameter. The opposite is true for $T >> T_c$: $\alpha > 0 \Rightarrow G_s > G_n$, as shown in figure 2.6. Notice that

$$\begin{aligned} &\alpha = \alpha(T) = \alpha(0)\left(\frac{T}{T_c} - 1\right) \\ &\beta \neq \beta(T) \end{aligned} \tag{2.14}$$

With the GL theory it is possible to obtain the second London equation (2.11) where the density of carriers SC carriers is written with the equilibrium value of the order parameter (taken far from interference): $n_s = |\Psi_\infty|^2 = -\frac{\alpha}{\beta}$. Moreover, another characteristic length arises from the theory: the coherence length ξ_{GL}

$$\xi_{GL} = \sqrt{-\frac{\hbar}{2m\alpha}} \tag{2.15}$$

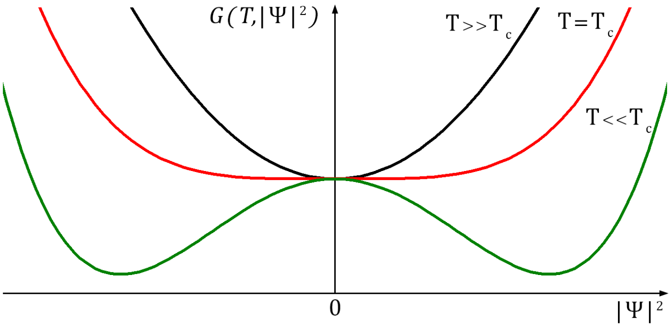

Figure 2.6: *Gibbs free energy as a function of the order parameter* $|\Psi|^2$*. For* $T >> T_c$ G *has a minimum at* $\Psi = 0$*, below* T_c *the SC state is stable and* G *has a minimum for* $\Psi \neq 0$*.*

It represents the characteristic length over which the order parameter varies: for a simple mono dimensional case, see figure 2.7, a real solution for $\Psi(z)$ can be obtained

$$\Psi(z) = \Psi_\infty \tanh \frac{z}{\sqrt{2}\xi_{GL}} \tag{2.16}$$

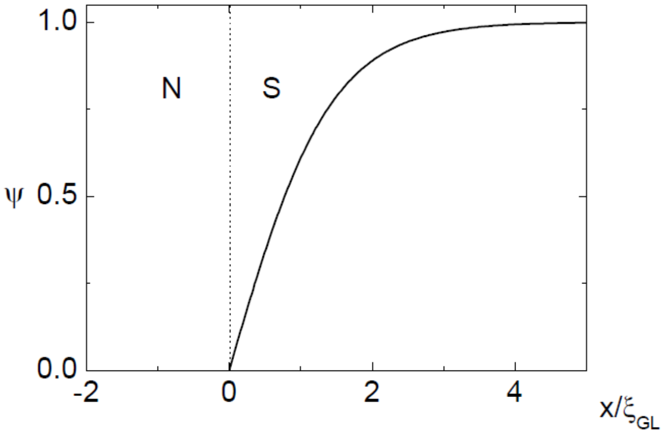

Figure 2.7: *Solution for the order parameter in a mono dimensional case.* Ψ *increases in the superconductor approaching the equilibrium value far inside the material.*

Since both the characteristic lengths are now expressed in terms of $(\alpha(T))^{-\frac{1}{2}}$, they have the same temperature dependence and it is useful to obtain a parameter free of this constraint. The ratio between the London penetration depth and the Ginzburg-Landau coherence length is defined as the GL parameter κ

$$\kappa = \frac{\lambda_L}{\xi_{GL}} \tag{2.17}$$

This parameter allows a categorization of type-I and type-II superconductors

$$\begin{aligned} \kappa < \frac{1}{\sqrt{2}} &\quad \rightarrow \quad \text{type-I} \\ \kappa > \frac{1}{\sqrt{2}} &\quad \rightarrow \quad \text{type-II} \end{aligned} \tag{2.18}$$

In figure 2.8 are reported the two situations described by the above relations.

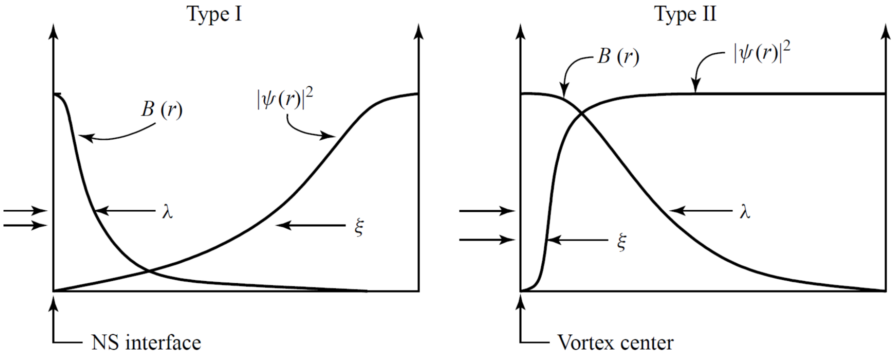

Figure 2.8: *Relations between* λ_L *and* ξ_{GL} *for type-I and II superconductors. The left side corresponds to* $\kappa < \frac{1}{\sqrt{2}}$*; the right side to* $\kappa < \frac{1}{\sqrt{2}}$*.* λ *is the London penetration depth and* ξ *is the GL coherence length. From* [11].

2.4 Cooper pairs and BCS parameters

The BCS theory is the first microscopic, quantum mechanical theory of superconductivity capable to make quantitative predictions. It has been proposed by Bardeen, Cooper and Schrieffer in 1957 and is based on the interaction of two electrons mediated by a phonon. In the superconducting state two electrons, with opposite momenta and spin, interact through the polarization trail they generate in the crystal lattice. Cooper demonstrated how this interaction is energetically favourable, i.e. it overcomes the electrostatic repulsion, hence these electron pairs are referred to as *Cooper pairs.* The particle exchanged in the interaction is a virtual phonon. If a real phonon was exchanged, it would consist in a dissipative process in which energy is transferred to the crystal lattice creating electrical resistance. The interaction distance of the Cooper pair is called BCS coherence length ξ_0, which is about $10^2 \quad - 10^3 \quad nm$. Since this distance is higher than the average distance between two conduction electrons ($\sim 10^{-1}\ nm$), Cooper pairs strongly overlap. This is an important aspect of the BCS theory because in order to maintain the binding, electrons forming Cooper pairs must "change their partner" continuously [19].

In figure 2.9 are represented the polarization, in a static model, of the crystal lattice due to electrons and the electron-electron interaction mediated by phonon.

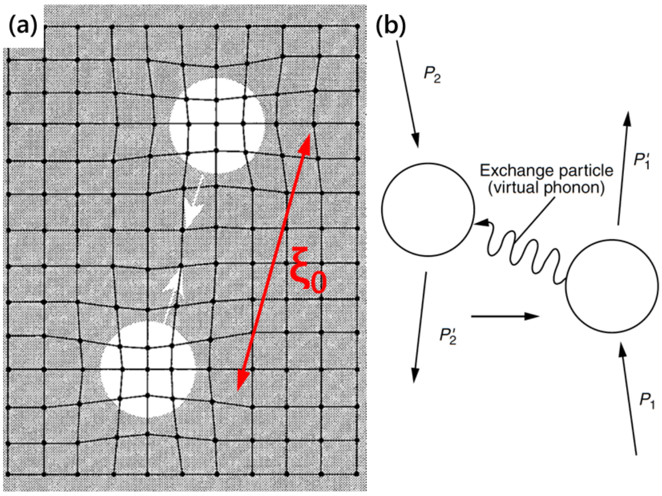

Figure 2.9: *(a) static crystal lattice polarization due to the electrons. The red arrow represent the BCS coherence length. (b) electron-electron interaction mediated by a phonon. From* [13].

2.4.1 Energy gap and BCS ground state

The BCS theory predicts an energy gap 2Δ (between 10^{-3} and 10^{-4} eV) in the SC state between the paired electrons state and the non interacting state, where Cooper pairs are broken into quasiparticles. It arises from the occupation probability of the paired state: a complex quantity $\tilde{\Delta} = \Delta e^{i\varphi}$ appears and is non-zero only for the electrons near the Fermi level, in a range of $\pm\hbar\omega_D$, where ω_D is the characteristic phonon frequency or Debye frequency. $\tilde{\Delta}$ depends on every k-state of the occupied and unoccupied paired state resulting in a collective phenomena of Cooper pairing. The SC energy gap can be considered as the condensation energy for the Cooper pairs

$$E_{pair} = 2E_F - 2\Delta \tag{2.19}$$

where ε_F is the Fermi level. It is important to underline that there is no excited state for Cooper pairs, an exitation would break them into unpaired quasiparticles.

Since the total momentum of a Cooper pair is zero and can be described as a macroscopic matter wave function, they occupy the same quantum ground state and behave as as bosons with spin 0.

2.4.2 BCS parameters relations

From the BCS theory it is possible to derive some important relations between the parameters described

$$2\Delta(0) = 3.5 k_B T_c \tag{2.20}$$

$$\xi_0 = \frac{\hbar v_F}{\pi \Delta(0)} \tag{2.21}$$

$$\lambda(T) = \lambda_L(0) \frac{1}{\sqrt{1 - \left(\frac{T}{T_c}\right)^4}} \tag{2.22}$$

$$n_n(T \to 0) \propto e^{-\frac{\Delta(T)}{k_B T}} \tag{2.23}$$

The last equation predicts that only at $T = 0$ every electron is in the SC state, meaning: $n_n = 0$, or alternatively $n_s = 1$.

2.5 SRF basis

In this section, the main aspects regarding RF conductivity and superconductivity (SRF) are presented.

2.5.1 Normal conductors in AC fields

For normal conductors in an AC field the skin depth δ represent the penetration length of the electric field in the material

$$\delta = \sqrt{\frac{2}{\mu \sigma \omega}} \tag{2.24}$$

where $\mu = \mu_0 \mu_r$ is the magnetic permeability, σ is the normal conductivity and $\omega = 2\pi\nu$ is the frequency of the AC field. The induced currents on the surface shields the rest of the material from the field. The impedance of a conductor Z is an imaginary quantity: the real part R_s is the surface resistance and the imaginary part X_2 is the reactance

$$Z = R_s + iX_s \tag{2.25}$$

$$R_s = \frac{1}{\sigma \delta} = \sqrt{\frac{\mu \omega}{2\sigma}} \tag{2.26}$$

At low temperatures the skin depth can be smaller than the electron's mean free path ℓ since σ increases, and consequently $\delta \propto \sigma^{-1/2}$. In this case, only the electrons with velocity almost parallel to the surface contribute to conduction. This is called the anomalous skin effect and leads to the definition of an effective conductivity $\sigma_{ef} = \frac{\sigma}{\ell}$. This limits the surface resistance even of pure conductors operating in AC fields. Notice that the above relation for R_s (eq 2.26) is not valid in the anomalous skin effect regime, instead the dependence is $R_s \propto \omega^2 \sigma$.

2.5.2 Superconductors in AC fields

Superconductors have surface resistances orders of magnitude lower than normal conductors, for example copper has $R_s(4\ K) \sim m\Omega$, while NbTi has $R_s(4\ K) \sim \mu\Omega$. This makes them an optimum choice for applications in SRF. The BCS theory predicts a null surface resistance for $T = 0$, because the density of NC electrons is zero (equation

(2.23)), but empirically it has been found that a finite residual resistance R_0 appears [20]

$$R_s(T) = R_{BCS}(T) + R_0 \tag{2.27}$$

$$R_{BCS} \propto \omega^2 \sigma_n e^{-\Delta(T)/k_B T} \tag{2.28}$$

where ω is the field frequency and σ_n is the NC conductivity.

2.5.3 Resonant cavities

Resonant cavities are a region of space enclosed within conducting walls where resonant electromagnetic modes can be excited. The geometry of the cavity determines the excitation efficiency of a particular mode that can be described as a RLC circuit [20]. A simple resonant cavity is often described as a *pill-box cavity*, a simple cylindrical structure, depicted in figure 2.10. The mode represented is the TM$_{010}$, which is the one often used in particle accelerators because it has the electrical field maximum at the center and minimum on the cylindrical surfaces, allowing to transfer energy to a charged particle moving along the axis. Instead, the magnetic field has its maximum value on the surfaces and its minimum at the center. Note that it has parallel field lines.

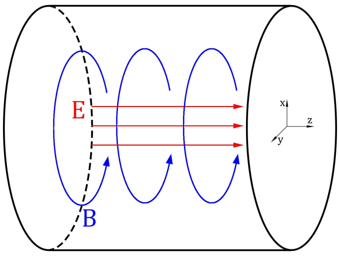

Figure 2.10: *Pill-box resonant cavity. The field lines for the TM_{010} mode are represented: in blue the magnetic field and in red the electric field.*

A fundamental parameter of these resonators is the quality factor Q_0, defined as the ratio between the stored energy and the energy dissipated per unit cycle in the cavity walls

$$Q_0 = \frac{\omega_0 \mu_0}{R_s} \frac{\int_V |\mathbf{H}|^2 dv}{\int_S |\mathbf{H}|^2 ds} \tag{2.29}$$

where ω_0 is the resonant frequency of the mode. It is also represented as the ratio between the peak frequency and its Full Width at Half Maximum (FWHM), $\Delta\omega$, assuming a lorentzian shaped peak profile

$$Q_0 = \frac{\omega_0}{\Delta\omega} \tag{2.30}$$

When coupled to a receiver, the quality factor is affected by the coupling factor β_L: $Q_L = Q_0(1 + \beta_L)^{-1}$, where Q_L is the loaded quality factor. In conditions of critical coupling $\beta_L = 1$: the reflected signal is minimized and the power transmitted is maximized.

2.6 Fluxoids

As already mentioned, type-II SC materials allow partial magnetic field penetration in the Shubnikov phase. This happens because vortexes of supercurrents are created in the material. The vortexes - or fluxoids - generate normal conducting regions trough which a quantized magnetic flux can flow; the quantum unit of flux is

$$\phi_0 = \frac{h}{2e} = 2.07 \times 10^{-15}\ Tm^2 \tag{2.31}$$

Recalling figure 2.8 (right side), it is possible to see that a vortex has a diameter of $\sim 2\xi_{GL}$, so the Cooper pair density is null at the center of the vortex. Moreover, the magnetic field extends in the SC region, restored after a length $\sim \xi_{GL}$, according to (2.12). In an ideal superconductor the vortexes are arranged in a triangular lattice, figure 2.11.

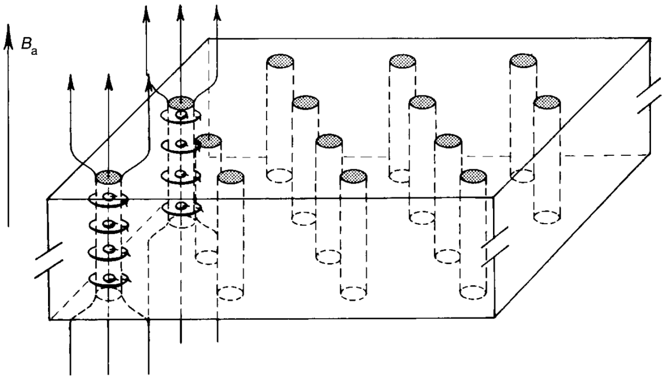

Figure 2.11: *Vortexes lattices arrangement. B_a is the external applied magnetic field. From* [13].

2.6.1 Flux flow resistance

Fluxoids are cause of energy dissipation due to their motion under the influence of a current density in the material **J**. In fact, the resulting Lorentz force exerted on the flux line $\mathbf{F}_L = \mathbf{J} \times \boldsymbol{\phi}_0$ accelerate them until it equals the opposing viscous force. The field lines' movement generates a spatially varying magnetic field, hence an electric field $\mathbf{E} = -\mathbf{v} \times \mathbf{B}$ is induced, **v** is the velocity of the fluxoid, in the direction of **J**. The NC electrons are subject to this electric field and they dissipate energy due to ohmic losses, this resistive behaviour, called *flux flow resistance*, limits the operational regimes of the material.

2.6.2 Pinning

By preventing flux motion it is possible to bypass this problem, often occurring in high quality materials. A force that opposes $\mathbf{F}_L$ has to be introduced: the *pinning force* $F_P = J_c\phi_0$, where J_c is the critical current density. Flux pinning, or just pinning, arises from spatial inhomogeneities in the superconductor: the flux lines are bounded to these defects and their displacement is disfavoured, at least, until when F_L overcomes the pinning force, in which case the fluxoid is depinned.

The pinning defects can be either intrinsic of the material, like point defects, dislocations, grain boundaries, secondary phases and so on, or they can be introduced *ad hoc* through doping or incorporating hetero structures. Effective artificial pinning is done by introducing defects the size of ξ_{GL}. Superconductors with strong pinning are called *hard superconductors.*

The depinning can be also thermally activated, making the depinning less abrupt. Three regimes of flux motions are possible due to the relation between the forces: the flux flow regime, already described, the flux creep regime happens when $F_L \simeq F_P$ and the thermal flow when $F_L \simeq F_P$ at $J = 0$.

Increasing the magnetic field corresponds to a greater number of fluxoids generated in the material that allow permeation, so the lattice is more compact and they can even "share" pinning centers. In this sense, the upper critical field $B_{c2} = \frac{\phi_0}{2n\xi_{GL}^2}$ can be seen the field at which the NC regions of the fluxoids overlap. Another limiting parameter is the field over which the flux lines exceed the capability of pinning, leading to free flux motion.

2.6.3 Microwave regime

In the microwave (MW) frequency regime, the response of the vortex system is simplified with respect to lower frequencies. The oscillation amplitude of the vortexes are small enough to treat the whole system in a local limit, taking in analysis only one fluxoid [21]. The force equation for the fluxoid motion is

$$\eta\dot{\mathbf{x}} + k_p\mathbf{x} = \mathbf{F}_L + \mathbf{F}_T \tag{2.32}$$

where $\mathbf{F}_T$ is the force that determines thermal depinning effects, $\eta\dot{\mathbf{x}}$ is the drag force (η is the viscous drag coefficient), $k_p\mathbf{x}$ is the pinning force that recall the fluxoid to its equilibrium position at the pinning center in the approximation of small displacements. k_p is the pinning coefficient and is related to the strength of the pinning potential (curvature of the pinning potential well) [22].

It is possible to determine the crossover frequency at which this elastic regime is valid. It is called (de)pinning frequency

$$\omega_p = \frac{k_p}{\eta} \tag{2.33}$$

In particular, It is important to underline that these parameter are temperature and field-dependent.

3

Materials for SRF applications

For more than 50 years, bulk niobium has been the SRF community's go-to material. Extensive research activities during these decades pushed its performance close to the theoretical limit. Only recently, new strategies and alternative materials are being investigated with great effort to overcome Nb performances and reducing the costs of the RF systems. An example of a new, promising strategy is that of Nb deposited on copper (both thin and thick films) [23, 24]. It aims to offers the advantage of having the same RF performance of bulk Nb and transferring the structural stability to a cheaper material with higher thermal conductivity. Better performing materials than Nb offer the advantages of a higher T_c and Hc, which allows to reduce the cryogenics costs by working at LHe temperature or even above. Also, they could be deposited on an adequate substrate taking advantage of its thermal properties (the best substrate candidate is copper) [25].

In the following, an overview of the two materials objective of this work will be presented.

3.1 NbTi alloy

The NbTi alloy is widely used for SC magnets [26–28] thanks to its desirable metallurgical and SC properties. It is in fact very ductile, which allows it to be strained into thin filaments and embedded in a copper matrix forming multifilamentary cables, in figure 3.2 is represented the cross section of a NbTi wire. It is a type-II superconductor and its critical parameters depends on the composition; the T_c ranges between $8 - 10\ K$ and the upper critical field has a maximum of $\simeq 12\ T$ for a 50% in weight of Ti, see figure 3.1. It has a *bcc* crystal structure (space group Im$\bar{3}$m) with a lattice parameter of 3.286 Å. NbTi is commercially available as sputtering target in different compositions and shapes, making it a strategic choice for PVD techniques.

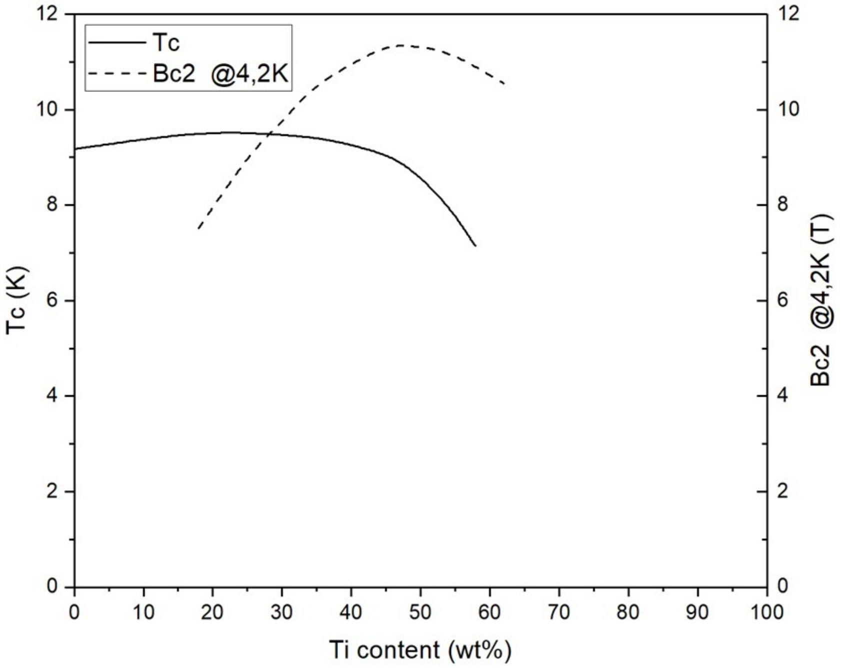

Figure 3.1: *Critical temperature and upper critical field of NbTi as a function of the weight percent of Ti. The composition around 50% of Ti offers the highest critical field at the expense of a lower* T_c *. Adapted from* [29].

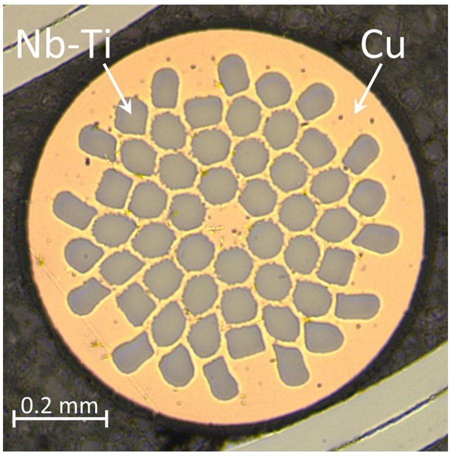

Figure 3.2: *Cross section of a multifilamentary SC cable made with NbTi strands embedded in a copper matrix. From* [30].

3.2 Nb$_3$Sn: an A15 material

Nb$_3$Sn is an intermetallic binary compound of the A15 family with compound formula A$_3$B, where A is a transition metal (like Nb or V) and B usually is a non transition metal (like Si, Ge, Sn). This class of materials present a typical cubic β-tungsten structure, Pm$\bar{3}$n space group, shown in figure 3.3. The B element constitutes the *bcc* lattice and two A atoms are placed in the faces of the cube forming three orthogonal linear chains in the directions $\langle 100 \rangle$. The superconductive properties are related to the linear chains of A. Taking as example the Nb$_3$Sn compound, it is found that in the A15 structure the distance between Nb atoms (0.265 *nm*) is reduced compared to nearest neighbour in *bcc* niobium, which is 0.286 *nm*. This causes a high density of states near the Fermi level.

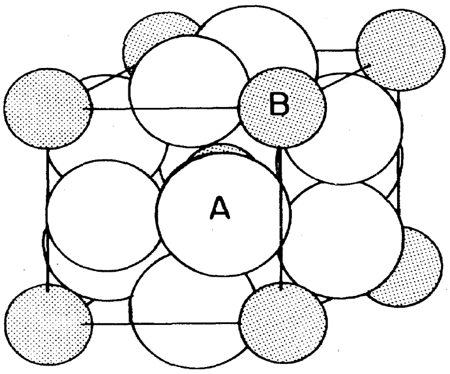

Figure 3.3: *The A15 or β-tungsten crystal structure. The element B forms the bcc lattice, A forms three linear chains in the cube's faces. From* [31].

The Nb-Sn phase diagram proposed by Charlesworth *et al* [32], see figure 3.4 present three main stable phases, namely Nb$_6$Sn$_5$, NbSn$_2$ and Nb$_3$Sn . The first two phases present SC behaviour at temperatures too low for any practical application (both T_c are below 3 K). On the other hand, Nb$_3$Sn present SC properties that makes it interesting for substituting Nb and NbTi due to its high critical fields and T_c that will be later discussed.

The phase of interest for SC application is $Nb_{1-\beta}Sn_{\beta}$ which is stable in a under-stoichiometric range $0.18 < \beta < 0.25$. Tin vacancies are occupied by the excess of Nb atom, this is believed to affect the DOS peak because it breaks the continuity of the Nb chains, thus degrading the SC properties. The lattice parameter for the stoichiometric composition $\beta = 0.25$ is 5.290 Å.

3.2.1 Tin content variations

The tin content β is related to the modification of the phase's properties like the lattice parameter a, T_c and H_{c2}.

The lattice parameter has been related to the tin content by Devantay *et al.* [34] and shown in figure 3.5. The empirical linear dependence is

$$a(\beta)[nm] = 0.0136\beta + 0.5256 \tag{3.1}$$

In the figure is also reported a linear dependence extrapolated by considering a metastable Nb$_3$Nb system.

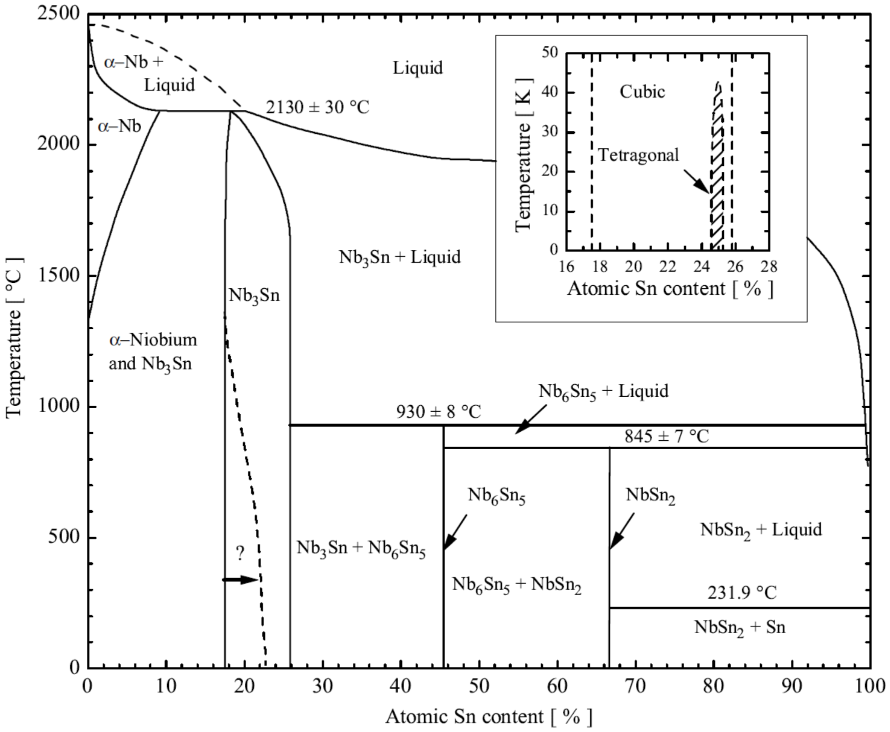

Figure 3.4: *Binary phase diagram for the Nb-Sn system proposed by Charlesworth et al. In the region between 18 and 25 atomic % of tin the Nb_3Sn A15 superconductor can exist. From* [33].

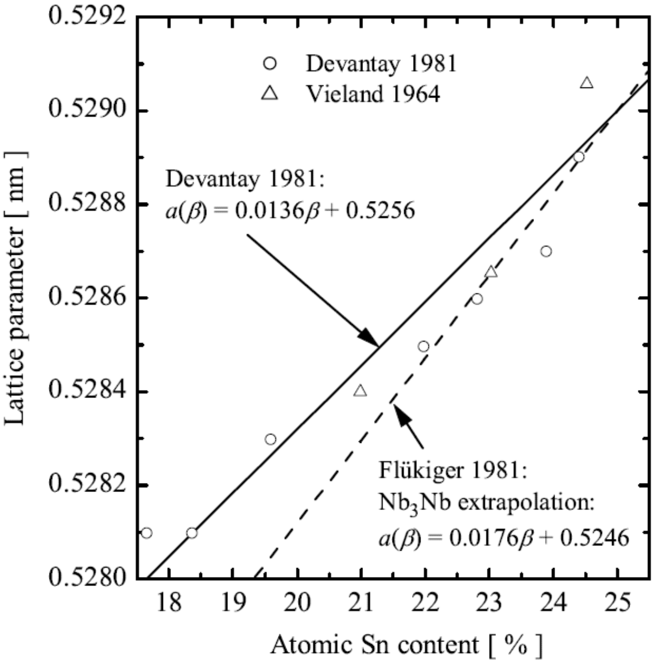

Figure 3.5: *Lattice parameter dependence from the tin content. From* [33].

The critical temperature and the upper critical field are also related to the stoichiometry. The following relations are extrapolated by experimental data [33] and are represented in figure 3.6

$$T_c(\beta) = \frac{-12.3}{1 + exp^{\frac{\beta - 0.22}{0.009}}} + 18.3 \tag{3.2}$$

$$\mu_0 H_{c2} = -10^{-30} exp\left(\frac{\beta}{0.00348}\right) + 577\beta - 107 \tag{3.3}$$

The first is a Boltzmann sigmoidal function and assumes a maximum of T_c of 18.3 K, which is the highest value obtained for Nb$_3$Sn . Comparing the two plots in figure 3.6 it is possible to notice that the highest critical temperature is obtained at a stoichiometric composition yet the upper critical field, at 0 K, has a maximum of 30 T for β slightly above 0.24. At $\beta \simeq 0.245$ the A15 phase undergoes a shear transformation around 43 K resulting in a tetragonal crystal structure, it can be seen in the inlet of the phase diagram (fig 3.4).

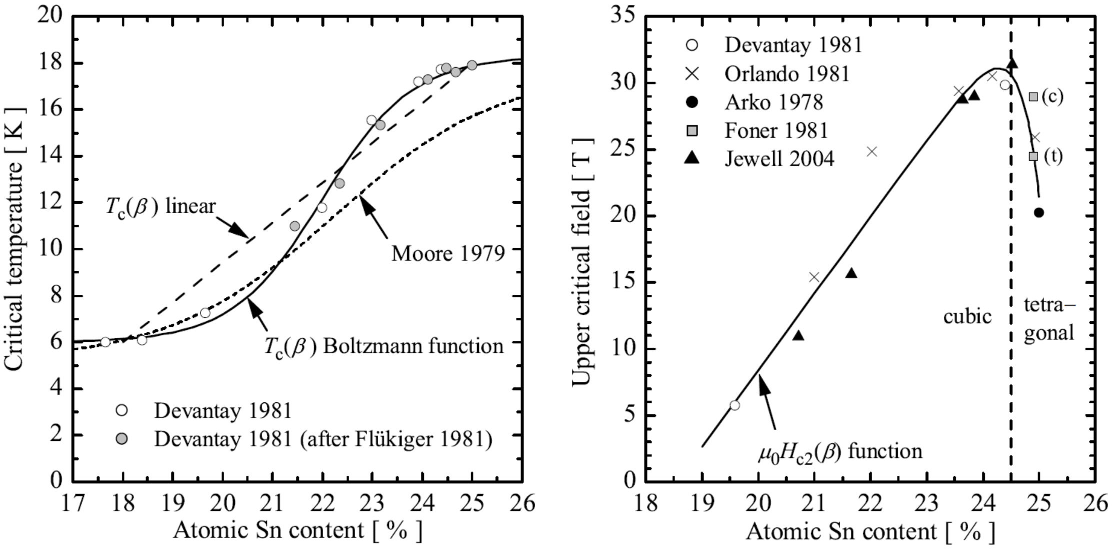

Figure 3.6: *T_c (left) and $H_{c2}(0)$ (right) as a function of β. From* [33].

3.2.2 Nb$_3$Sn production methods

This A15 material is widely used in SC wires as alternative to NbTi wires. For this application, the production is mostly based on solid-state reactions between Nb and Sn, but due to its extremely brittle nature it is impossible to produce bulk complex structures feasible for SRF devices [35]. For this reason different methods for fabricating a Nb$_3$Sn layer onto the inner surface of a SRF cavity have been investigated through the years. Now, the goal of the SRF community is to optimize the Nb$_3$Sn on copper technology.

Tin Vapour Diffusion

An extensive research on the production of SRF accelerating cavities in Nb$_3$Sn has been carried out at Wuppertal University during the 80s and 90s by improving the work started at Siemens [36]. The method used is that of Tin Vapour Diffusion (VTD) where an uniform layer of metallic tin is deposited on the inner surface of the bulk niobium cavity, previously anodized (~ 500 Åof Nb_2O_5), by evaporating $SnCl_2$ at 500°C. The tin pressure is about 10^{-3} $mbar$. By raising the temperature above 600°C the oxide disintegrates and the interface Nb-Sn is created, then, at 1050-1250°C the Nb_3Sn layer of few microns is formed. This method has recently gained renewed interest and the work has been continued mostly at Thomas Jefferson National Accelerator Facility [37] and at Cornell University [38]. The Q_0 for a 1.3 GHz Nb_3Sn /Nb cavity at 4 K is higher than that of a bulk Nb one at 2 K - at least for accelerating fields up to $\sim 15\frac{MV}{m}$ [39].

Liquid Tin Diffusion

The Liquid Tin Diffusion (LTD) technique creates a Nb_3Sn layer on a Nb substrate dipped in a molten tin bath and subsequently annealed, the process is done in a UHV furnace [40]. This process has been developed at LNL as a variation of the TVD which bypasses the need of the toxic tin dicloride as tin source. Recently [41, 42], it has been improved by implementing a nucleation step carried out with Sn vapours and a coating step, always in the presence of Sn vapour, similarly to the TVD. Also, the impact of the niobium's anodization has been investigated. The thickness obtained is of the order of tens of microns, which could be enough for the production of single-use PVD targets, to be used for coating copper substrates.

PVD methods

TVD and LTD allows to grow Nb_3Sn only on niobium, so to use different substrates other methods are necessary. PVD techniques are an effective strategy to coat the complex SRF cavities' surfaces, although they could require *ad-hoc* target geometries - which are not readily available - to obtain an uniform film.

A possible strategy is that of a multi-layer coating of Nb and Sn by sequential sputtering. The A15 phase is then obtained by intermixing Nb and Sn through an annealing process [43]. A more straightforward approach is to directly use a stoichiometric target. An early attempt [44] showed promising results on sapphire substrate using DC magnetron sputtering (DCMS). Now, international groups are active in this field, with the focus on copper substrate.

Valizadeh *et al* [45] (STFC Daresbury, UK) showed good results for the films grown onto copper at 650°C, lower temperatures produced poorer performances and films deposited at room temperature showed no superconductive behaviour - although it was observed after an annealing but with the worst performances of the samples' series. They also investigated the effect of a niobium inter-layer between the copper substrate and the Nb_3Sn film, aiming to simulate the bulk niobium conditions that produced excellent results with the TVD. In this case, inhomogeneous zones were found and attributed to copper diffusion.

At CERN, Ilyna *et al* [46] studied the effect of two different thermal process routes on film deposited via DCMS on polished copper substrates and on sapphire. The first approach involves the film's deposition at room temperature followed by an annealing performed at temperatures ranging from 600 to 800°C. The as deposited samples showed no A15 phase and a highly disordered morphology, while after the high temperature annealing the correct phase is obtained and a grainy pattern emerges but the surface exhibit cracks due to releasing of stresses. The second approach used heated substrates

during the deposition. The samples prepared with this method presented the A15 phase, but in order to promote further improvements on the film morphology the samples should be kept at high temperature after the coating for a few hours.
The relation between working gas (Ar) pressure and composition showed that a higher P_{Ar} leads to a higher tin content, at the cost of a rougher surface - undesirable for RF application since the could lead field emitting features. So lower P_{Ar} produce denser and smoother films but with a lower tin content. The films grown on copper substrates showed lower T_c than those grown on sapphire, also, during the prolonged heat treatment Cu can diffuse into the film and reach the surface. To avoid this problem, an appropriate inter-layer of Nb or Ta could be adopted.

Overall, these results show that it is possible to synthesize Nb$_3$Sn onto copper from a stoichiometric target with the DCMS technique.

A comparative table for the SC parameters of Nb, NbTi and for Nb$_3$Sn is shown below

Parameter	Nb	NbTi	Nb$_3$Sn
T_c (K)	9.2	9.6	18.3
$B_{c2}(0\ K)$ (T)	0.4	13	30
λ_L (nm)	390	300	100
ξ_{GL} (nm)	39	4	3

Table 3.1: *SC parameters of Nb, NbTi and for Nb$_3$Sn .*

4

Axions and axion haloscopes

In this chapter, a brief illustration of the scientific context regarding axions is given, as well as an overview of the more relevant experiments focused on the detection of these particles, with an emphasis on the ones that use resonating cavities. General references for this chapter are [47, 48].

4.1 The strong CP problem

The theory of Quantum Chromodynamics (QCD) describes the strong nuclear force, one of the three fundamental interactions of the Standard Model: electromagnetic, weak and strong. This short range interaction is responsible for the stability of nuclei: at the length scale of nucleons ($\sim 10^{-15}$ m), it prevails on the electromagnetic repulsion of protons by approximately 100 times and is mediated by particles called mesons [49]. At a smaller scale ($\sim 10^{-16}$ m), it is the force that binds together quarks inside nucleons, this time, carried by different particles called gluons [50, 51].

In the framework of particle physics, a modification in a particle state can be described by three symmetries: Charge or charge conjugation (C), Parity (P) and Time (T). C inverts the charge, P flips the coordinates (or turns left-handed in right-handed) and T reverses the direction of time. Until 1950s, it was believed that they could not be broken. But in 1957, P violation was discovered in the weak interaction observing the β-decay of ^{60}Co nuclei [52]. In the following years, new violations of these symmetries have been discovered, except for the CP symmetry in the strong interaction.

The combination Charge+Parity symmetry (CP) asserts that the physical laws remain unchanged if a particle is changed with its antiparticle (C) and its coordinates are inverted (P). In the Standard Model, the violation of CP symmetry is allowed and it has been observed in some processes, the first example being in the weak interaction [53]. However, contrary to what was expected, CP violation has yet to be observed in the strong interaction. This represent the famous *strong CP problem*, which remains a puzzling open question.

4.2 Axions to the rescue

Axions have been theorized as solution to the strong CP problem. In 1977, Peccei and Quinn [1] proposed a model based on the introduction of a new symmetry called PQ, mathematically equivalent to a rotation around an axis, which as later pointed out Weinberg and Wilczek [54, 55], it gives rise to a new light particle: the axion. For precision of terminology, in literature the axion is often referred to as *QCD axion* to underline the fact that it is a possible solution to the problem described above and to distinguish it from other axion-like particles. In this work there will not be the need of such clarity, since it lies beyond its scope; thus, from here on, axion will be intended as *QCD axion*.

Axions interact with many particles of the standard model, but with a small coupling constant (g_i) that strictly depends on a parameter f_a related to the energy scale at which the PQ symmetry breaks down; it also defines the axion mass m_a. Theoretical considerations and cosmological observations set bounds for the axion mass between $10 \mu eV$ and $10^3 \mu eV$.

$$g_i \sim \frac{1}{f_a} \propto m_a \tag{4.1}$$

Axions are originated in the early universe and are bosonic, non-relativistic, light particle almost non interacting with ordinary matter and governed by gravity, which makes them cluster in so called *halos*: regions of inhomogeneity of the axion's scalar field $a(t, x)$. An observer from earth would see a wind of axions due to the solar system motion through such galactic halos. For these reasons they are good candidates for cold dark matter.

4.3 Search for axions

In 1983 Sivike proposed to exploit the coupling of the axion field to electromagnetism ($a\mathbf{B} \cdot \mathbf{E}$) to detect these elusive particles [56]. The underlying principle is the Primakoff effect. Through this mechanism, an axion interacts with an intense magnetic field (a virtual photon) and is converted into a photon with frequency matching its mass

$$a(t) = a_0 e^{-i\omega_a t} \tag{4.2}$$

$$\hbar\omega_a = m_a c^2 \tag{4.3}$$

leading to the axion's frequency ν_a, or analogously the generated photon's frequency

$$\nu_a = \frac{m_a c^2}{h} \tag{4.4}$$

Another coupling mechanism is that of axions to spins of fermions. The axion interact with a magnetized material causing a time dependent modulation of the magnetization when the Larmor frequency of the fermions is tuned to the axion's mass by means of a polarizing magnetic field.

4.3.1 Resonant cavities

The photon generated through the inverse Primakoff effect can be detected with a resonant cavity called *haloscopes* tuned to match the frequency ν_a typically with the TM_{010} mode. The mass range probed is in the order of $10 - 10^3 \mu eV$, hence the frequency is in the range of radio-frequency wave. The power of the signal is

$$P \propto g_{a\gamma\gamma}^2 V \frac{\rho_a}{m_a} B^2 Q_0 \tag{4.5}$$

where $g_{a\gamma\gamma}$ is the coupling constant to the electromagnetic field, V is the cavity's volume, ρ_a is the local axion density, m_a is the axion's mass, B is the magnetic field and Q_0 is the quality factor of the cavity - note that to be more precise it should be the loaded quality factor, but as previously described $Q_0 \propto Q_L$. The power deposited is extremely low, of the order of $10^{-22}\,W$, making necessary to use sensitive amplifiers (Josephson Parametric Amplifier and SQUID) and working temperatures near absolute zero to exclude the system's thermal noise. The operational parameters that can be optimized to improve the signal detection are primarily the magnetic field strength and the quality factor. Note that the volume is constrained by the frequency of interest. A basic representation of the apparatus of these haloscopes is shown in figure 4.1.

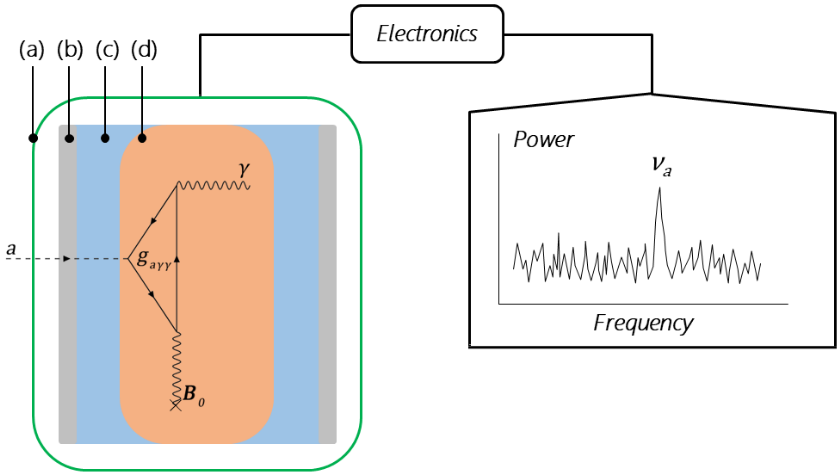

Figure 4.1: *Schematic representation of the apparatus for haloscopes. (a) is the cryostat, (b) is the solenoid that generates the magnetic field (c), (d) is the haloscope. For a more detailed setup description see* [9].

4.3.2 Axion Dark Matter eXperiment (ADMX)

The ADMX collaboration, active since 1995, exploit the Primakoff effect to probe a mass range around $2 - 4\ \mu eV$ with an electrodeposited copper cavity in a 8 T magnetic field generated with a NbTi SC coil leading to a quality factor of $\sim 10^5$ [57, 58].

4.3.3 Cosmic Axion Spin Precession Experiment (CASPEr)

The CASPEr project aims at detecting axion dark matter through the axion-spin coupling using NMR techniques. It is complementary to other project since it will probe a lower mass range that no other projects can achieve [59, 60].

4.3.4 QUaerere AXion (QUAX)

The QUAX project is an INFN LNL-LNF collaboration that aims at detecting axions in the mass range of $35 - 45\ \mu eV$ through the two coupling mechanisms described above. One proposal (QUAX $a-e$) exploits the electron spin coupling. The apparatus consist of a magnetized material, like Yttrium-Iron-Garnet, immersed in a strong magnetic field, when the Larmor frequency is tuned to the axion mass a RF signal is generated and collected with a resonating cavity. Another proposal (QUAX $a - \gamma$) exploits the Sivike configuration, hence the photon coupling and two different haloscopes are employed: one based on cylindrical sapphire cavity and another based on a SC resonant cavity. [61].

NbTi haloscope

In order to improve the sensitivity of the haloscope, one fundamental parameter that can be optimized is the Q factor. One obvious choice for doing that would be recurring to type-II superconductors, since they can withstand the strong magnetic field necessary for the axion coupling.

In 2019 a 9GHz copper haloscope coated with NbTi has been developed and tested at 4 K in a 2 T magnetic field, giving a quality factor of 4.5×10^5 for the TM_{010} mode [9]. The SC film increases Q_0 of about one order of magnitude with respect to a pure copper cavity, which barely reaches 10^5 and experimentally is set to be $\gtrsim 10^4$ [62].

The haloscope is composed of a OFHC body divided in two semicells to facilitate the coating procedure of the cylindrical internal part. To overcome the external magnetic field screening due to the superconductor, the two semicells will be separated by a thin copper layer. This would interrupt the supercurrents and thus allowing more magnetic flux in the inner part. One coated semicell and the simulation of the TM_{010} mode are reported in figure 4.2.

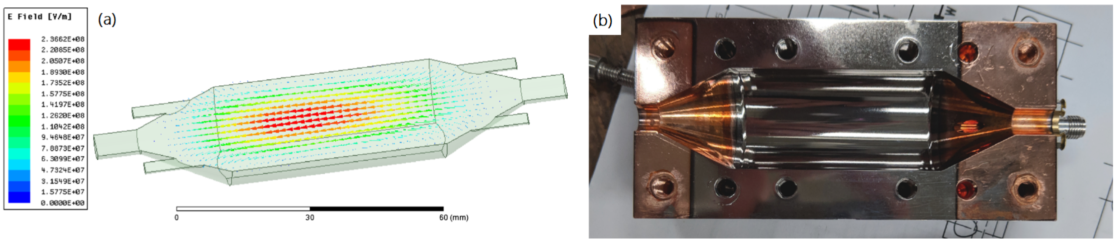

Figure 4.2: *(a) electric field simulation for the TM_{010} mode and (b) one haloscope semicell coated with NbTi. From* [9].

4.3.5 Relic Axion Detector Exploratory Setup (RADES)

The RADES experiment at CERN [63] uses superconducting cavities for the axion search in the mass range above $30\mu eV$. The SC materials of choice were Nb_3Sn and ReBCO - a high T_c superconductor: $ReBa_2Cu_3O_{7-x}$ where Re is a rare earth element, commonly Y, Gd or Eu. The Nb_3Sn has been deposited on the cavity via PVD technique and the ReBCO has been applied as a commercial tape. The resulting Q_0 as a function of the applied magnetic field, compared to the copper reference $Q_0 \simeq 4 \times 10^4$, showed a higher value for the Nb_3Sn cavity at low field but with a strong decrease at higher field providing even lower Q_0 than copper. The ReBCO cavity, on the other hand, showed a greater $Q_0 \simeq 7 \times 10^4$ which remains constant at high field up to 11 T. A picture of the ReBCO cavity is reported in figure 4.3(a).

4.3.6 SC haloscope at IBS

At the Center for Axion and Precision Physics (CAPP) - part of the Institute for Basic Science in Korea (IBS) - another SC haloscope has been fabricated and tested by Ahn *et al* [64]. They used a polygonal cavity coated with a commercial YBCO ($YBa_2Cu_3O_{7-x}$) tape. The resulting $Q_0 \simeq 3 \times 10^5$, after an abrupt drop at low magnetic field, remains constant up to 8 T. A picture of the cavity is shown in figure 4.3(b) and (c).

4.3.7 Other projects

In the extreme conditions of the Sun, axions can be produced by the Primakoff effect resulting in a solar-axion flux. These solar axions have a spectral distribution around $1-10\ keV$ and can be converted back to photons when interacting with an electromagnetic field. One of the most famous experiments looking at solar axions is the CERN Axion Solar Telescope (CAST), that uses a decommissioned LHC dipole magnet to generate up to 9 T coupled to x-ray detectors. The *helioscope* is oriented towards the Sun and look for an excess of x-rays, the background is measured in non-alignement periods [65].

A series of experiment in axion search do not rely on cosmological source. An interesting example of "purely laboratory experiments" uses the principle of photo regeneration, or Light Shining through a Wall (LSW): a coherent light source is shone to an optical barrier where the photons are converted to axions. They would now be able to permeate the barrier and be reconverted to photons behind it. The overall phenomenon would be precisely what the name suggests. A main LSW experiment is CERN Resonant Weakly Interacting sub-eV Particle Search (CROWS) [66].

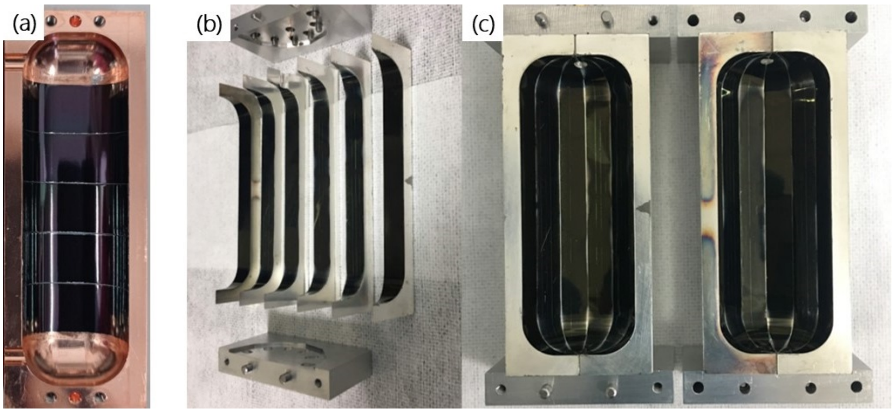

Figure 4.3: *(a) ReBCO haloscope half-cell produced at CERN for the RADES experiment, from* [63]. *(b) and (c) YBCO polygonal haloscope produced at CAPP, from* [64].

5

Experimental Methods

5.1 PVD processes

Among the vast world of physical vapour deposition (PVD) techniques, many are used in industrial applications and research activities due to their versatility regarding the coating material type and purity and the type of substrate. In this category of process, a material is vaporized and transported through a vacuum environment to the substrate where it grows in a condensed structure.

In a sputtering process the coating material (target) is in a bulk form. A plasma, typically of a noble gas, is ignited from a cathodic potential applied to the target: free electrons are accelerated and collide with the neutral gas atoms which are then ionized. This is an avalanche process because for each incident electron, one more is generated by the ionization of the neutral atom: $\mathrm{e}^- + \mathrm{A} \longrightarrow 2\,\mathrm{e}^- + \mathrm{A}^+$. A sputtering process operates in the abnormal glow discharge regime, where the bombardment covers the entire cathode surface [67].

The plasma is generated in a vacuum of about 10^{-2} to 10^{-3} *mbar* in order to have a high mean free path of the particles and avoid energy losses. The high energy particles (ions) bombard the target causing its vaporization [68].

5.1.1 DC magnetron sputtering

In DC magnetron sputtering (DCMS) a magnetic field confines the secondary electrons emerging from the target, after the ion collision, close to its surface. This causes an enhancement of the plasma density, hence, a higher deposition rate. Different configurations of this technique are possible, depending on the substrate geometry and the coating material. Moreover, magnetron sputtering is exploited in AC regimes and in variation of the DC mode as in High Power Impulse Magnetron Sputtering (HiPIMS). As the name suggests, this methods uses high intensity short pulses ($\sim 100\ \mu s$) of current that allows to ionize a fraction of the sputtered atoms that are accelerated to the substrate through a bias voltage. As a consequence, the film obtained is denser and smoother, a desired feature for SRF applications [69, 70].

The planar DCMS configuration, represented in figure 5.1, consist of a target planar to the anodic (usually grounded) sample holder.

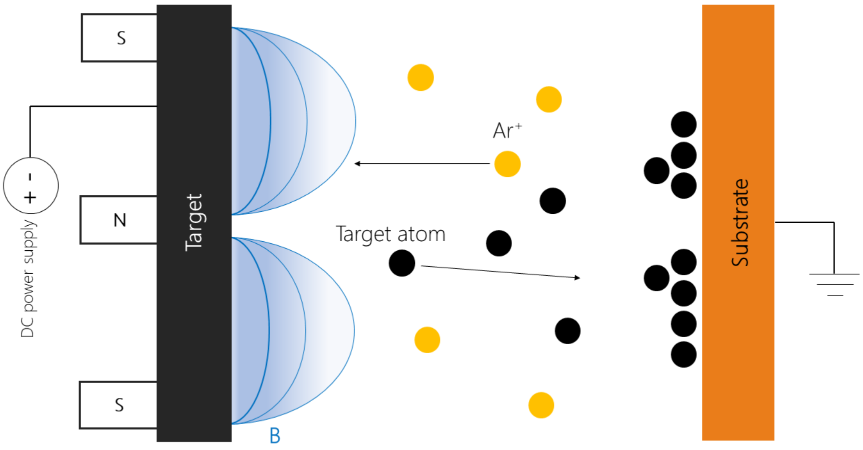

Figure 5.1: *Schematic representation of a planar DCMS configuration.*

The source of the magnetic field can be permanent magnets placed below the target and arranged in order to have magnetic field lines parallel to the target surface that form a closed elliptical shape; in figure 5.2 are represented the applied electrical and magnetic fields to a rectangular target [67]. The continuous plasma bombardment makes the target's active cooling an essential need to avoid overheating it and the magnets. The magnetic field can also be generated by electromagnets.

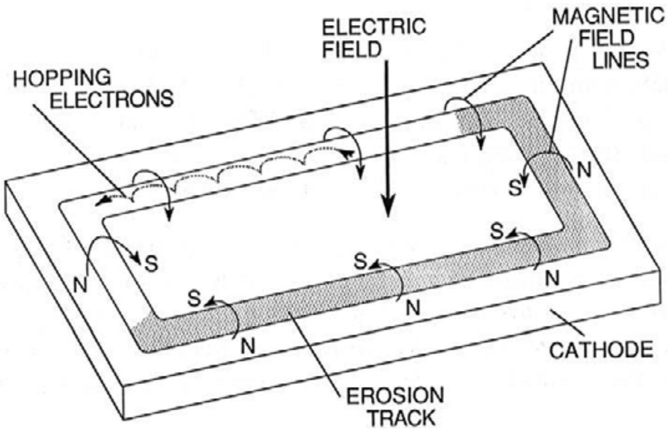

Figure 5.2: *Applied electrical and magnetic fields to a rectangular target. From* [67].

5.1.2 Description of the sputtering sources

In this work two planar magnetron sputtering sources, of 4 inch (10,16 cm) in diameter, have been used. The NbTi system has a commercial "MeiVac 4" MAK UHV Sputter Source" magnetron, where the target is easily put in place with a centering magnet mounted behind it. In order to do this, a threaded hole has to be machined behind the target, limiting its use to materials with good mechanical properties (like most pure metals and alloys). That is not the case for Nb_3Sn , which is too brittle and fragile to attempt making such machining. For this reason, the Nb_3Sn system in equipped with a magnetron developed at LNL [71] which makes use of concentric electromagnets to generate the magnetic field and the target is held by a steel ring to the base-plate in a uniform way. In figure 5.3 the magnetron used are shown.

For NbTi, an old target obtained from a slab with a composition 44 $wt\%$ of Ti, has been used for running a test with similar parameters to that used to deposit a 9GHz axion cavity in 2019; also the magnetron used was the one developed at LNL. This target was not optimized for the depositions: after several processes it became too thin and bent, with the result of having a poor electrical and thermal contact. With the new sputtering source, a new bulk (5 mm thick) target, with a composition 47 $wt\%$ of Ti has been purchased and used. For Nb_3Sn , a stoichiometric target (99,9% purity) has been used.

The power supply used for both systems is an "ADL GS 30/800" with maximum DC output of 3 kW, 800 V and 5.3 A. For every deposition, the power supply has been controlled by limiting the current output.

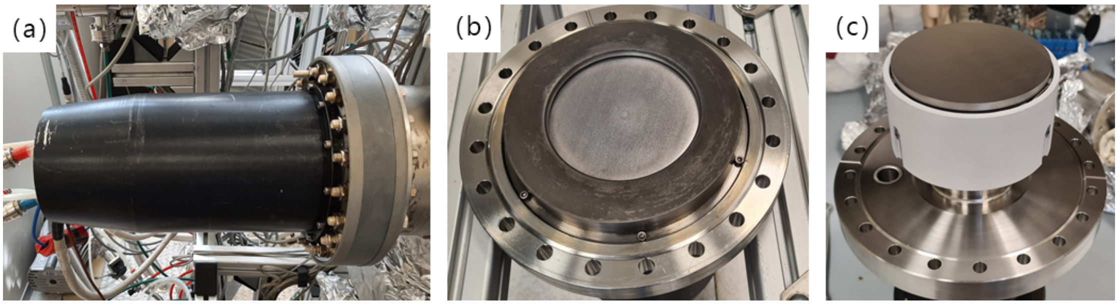

Figure 5.3: *4 inch planar DCMS sources used. (a) and (b): Nb_3Sn "in-house" magnetron; (c) NbTi commercial magnetron.*

5.2 New vacuum systems for SC haloscopes coating

In this work, a new UHV system dedicated to Nb_3Sn coatings has been set up as part of a general upgrade of the the vacuum systems present at LNL. The previous configuration, shown in figure 5.4, presented limited access to all the parts and limited space for upgrades, whereas the new design is more versatile and easy to work on because it allows to keep 4 vacuum systems independent and easily adaptable. The upgraded stand with the vacuum systems is presented in figure 5.5.

5.2.1 Description of the vacuum systems

To deposit SC materials an UHV coating systems is desired due to the need of having a clean environment free of contaminants and reactive species that might undermine the quality of the material. Dry vacuum pumps are commonly used in order to avoid oil back-streaming in chamber. Moreover, to improve the vacuum level (lowest pressure achievable) and the vacuum quality, namely the residual gas content, the system is heated for several hours. This process is named *baking*, which increase the degassing and desorbing rates from the chamber walls. The heating is done by means of bands located around the CF flanges, the temperature can be set to different values in three

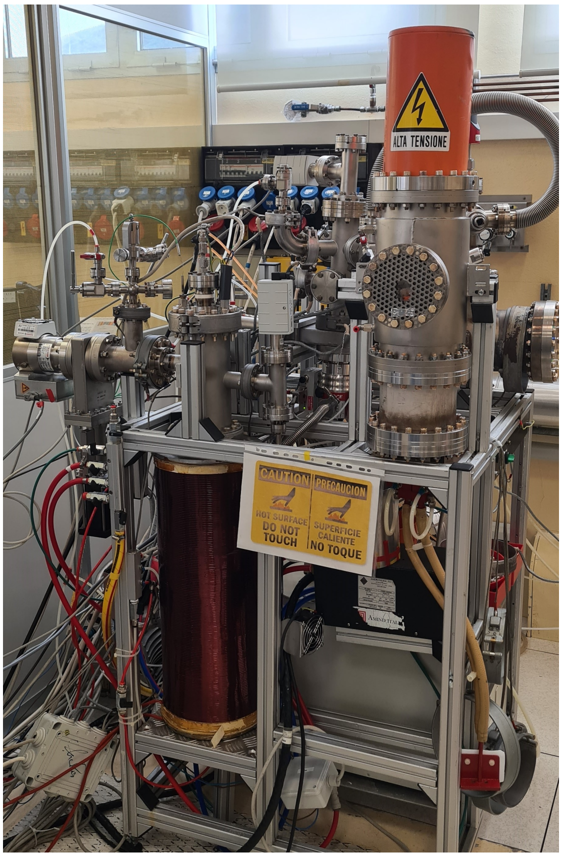

Figure 5.4: *Old configuration of the vacuum systems.*

Figure 5.5: *The three coating systems at LNL and their controllers. They are dedicated to (from left to right): 6GHz accelerating cavities (not used in this work), Nb_3Sn and NbTi. In the far right side there is the induction heating chamber equipped with a RGA.*

different zones. The baking in the main chamber is done at 200°C; near vacuum gauges, valves and parts with Viton® O-Rings the temperature is 120°C. Also, the sample holder is designed to be baked, see section 5.2.2. The two systems used in this work are designed to satisfy these requirements.

One system is dedicated to Nb and NbTi, the other is used exclusively for Nb_3Sn. Both are connected to an Edwards nXDS10i dry scroll primary pump to create a rough vacuum, about $10^{-}2$ $mbar$. An electro-pneumatic valve allows to insulate the pump from the systems and a manual angle valve allows to bypass the pump during the leak tests. For simplicity, just the Nb_3Sn vacuum system is described in the following, since the NbTi system is conceptually analogous.

A Pfeiffer HiPace® 80 turbo-molecular pump is connected to the primary pump and allows to reach UHV, it can be insulated by a CF100 gate valve. The turbo pump is connected to the main chamber through a CF100 90° curve section and CF100 to CF150 transition. The main chamber is a CF150 cross where the sample holder and the DCMS source are directly connected. Several devices are connected through a CF35 cross transition: a nitrogen gas line, for the venting, and an argon gas line, for the sputtering process. The gas lines are insulated with shut-off valves and the argon is introduced in the UHV region through a leak valve to control the sputtering working pressure. Moreover, a safety valve and two vacuum gauges, one Pfeiffer Compact FullRange$^{\mathrm{TM}}$ BA gauge and one Pfeiffer capacitive CMR364 are also connected. In addition to these features, the NbTi system has a separate chamber that can be insulated by a CF63 shut-off valve, equipped with a Residual Gas Analyzer (RGA) and an induction system for heat treatments on 6GHz accelerating cavities [72]. In figure 5.6 the diagram of the Nb_3Sn vacuum system is shown.

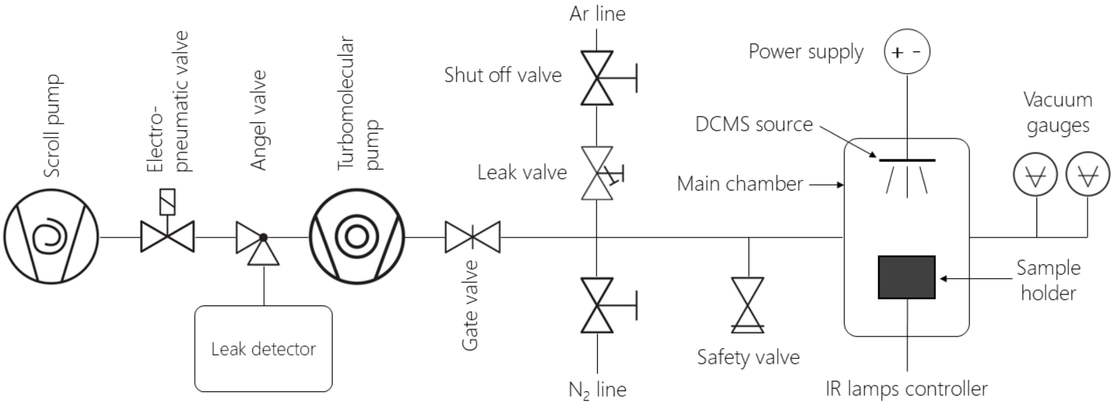

Figure 5.6: *Schematic diagram of the Nb_3Sn vacuum system. Adapted form* [73].

5.2.2 The sample holder

The sample holder is designed to heat the samples during the deposition; this is done with 500 W infrared lamps placed beneath the plate. The temperature is monitored by a thermocouple pressed on top of the plate (near the samples). During this work the Nb_3Sn sample holder has been upgraded from a steel plate and lamps shield to a niobium plate and a copper lamps shield. The motivation resides in avoiding the copper samples from sticking to the steel plate and, since copper partially reflect IR radiation, the copper shield allows a more efficient operation of the IR lamps: a lower power was required to achieve the set-point temperature and only two lamps were necessary instead of the three needed in the ”steel configuration”. Additionally, a collapsable folding fan screen (shutter) is placed on top of the samples to cover them during the sputtering process' first minutes. It can be opened, exposing the samples to the sputtered atoms, by a rotating manipulator. In figure 5.7 the steel sample holder and the upgraded one are shown. The sample holder for the NbTi system is analogous to the Nb_3Sn upgraded one.

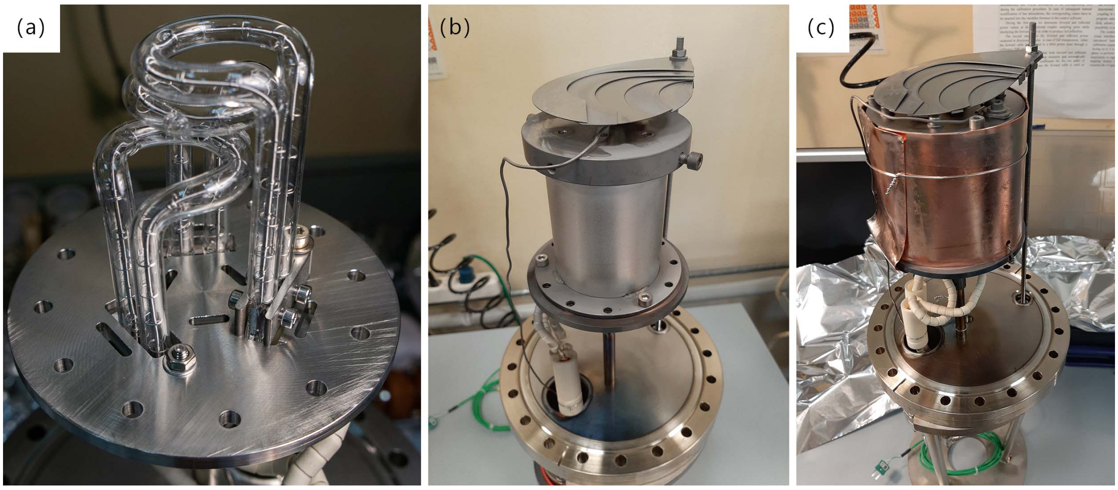

Figure 5.7: *Sample holders used in the Nb_3Sn system. (a) IR lamps; (b) ”steel configuration” sample holder and (c) upgraded configuration.*

5.2.3 Deposition procedure

A coating process requires different passages to be successful. In the following, a brief description of the general procedure implemented in this work is presented. Note that the steps are the same for both NbTi and Nb_3Sn processes where not specified otherwise.

1. mounting the samples on the sample holder's plate;
2. mounting the sample holder on the main chamber;
3. vacuum generation, first with primary pump to at least 10^-1 *mbar* then with turbo-molecular pump;
4. leak-test;
5. baking with heating bands starts when the pressure is sufficiently low (at least 10^-4 *mabr*) ;
6. baking with IR lamps starts when the temperature and the pressure are stabilized (after about 30 minutes);
7. band heaters switch-off and IR lamps set to deposition temperatures: end of baking;
8. leak test;

9. sputtering process;
    (a) (for Nb_3Sn) *in-situ* annealing;
    (b) (for Nb_3Sn) controlled cool down;
10. venting when room temperature is reached.

The baking is carried out for 24 to 60 hours at a higher temperature than the coating process. When the baking has ended, the temperature is left to stabilize and the pressure to drop.

The leak test is performed with a PHOENIXL 300 leak detector, shown in figure 5.8. It consist of a primary pump and a quadrupole detector set to 4 He mass. The device is connected to the vacuum system in analysis bypassing its primary pump and is left pumping until it reaches the lower detection limit of 1×10^{-12} $mbarLs^{-1}$. The detection gas (helium) is then sprayed near every flange.

The first leak test is not strictly necessary, but it is useful to detect leaks at room temperature because, if found, they can be readily closed. Note that often a leak can appear between two CF flanges and if it happens, the copper gasket must be replaced. This involves venting of the vacuum chamber, which cannot be done while baking because the samples at high temperature would oxidize rendering them unusable. However, the leak test done right before the deposition process ensures that the UHV environment is sealed and free of pollutants.

Figure 5.8: *The PHOENIXL 300 leak detector.*

5.3 Samples preparation

Different substrates have been used in this work, namely: ceramics (9x9 mm quartz and 10x10 mm sapphire), Oxygen Free High Conductivity (OFHC) copper, from here on it will be referred to only as copper, and niobium deposited on copper (Nb/Cu) with two different thicknesses.

Ceramics substrates are cleaned and degreased with an ultrasonic bath (Branson 5510) in a solution of Rodastel 30 (industrial surfactant agent) for 30 minutes. After, they are rinsed and placed again in the ultrasonic bath in deionized water for 15 - 30 minutes. Finally, they are rinsed with ethanol, dried with a nitrogen flux and stored in 95% RPE grade ethanol.

Copper substrates are treated in a similar way as ceramics, but the surfactant agent is now GP 17.40 SUP. Moreover, they undergo a chemical polishing in order to achieve a smoother surface, the solution used is SUBU5 which was developed at CERN for LEP2 [74]. It consist of a solution containing: sulfamic acid (H_3NSO_4 5 g/L); ammonium citrate ($C_6H_{11}NO_7$ 1 g/L); hydrogen peroxide (H_2O_2 30%, 50 mL/L) and n-buthanol ($C_4H_{10}O$ 50 mL/L). The solution is kept at a constant temperature of 72 ± 2 °C and agitated with a magnetic stirrer, the treatment lasts few minutes and removes around 50 μm. They are stored in 99.9% RPE grade isopropanol.

Nb/Cu samples are prepared via DCMS. The polished copper substrates are placed in the NbTi system - equipped with a Nb target - and are coated following the procedure described in section 5.2.3. They are stored in a low vacuum vessel. In figure 5.9 the substrates are shown.

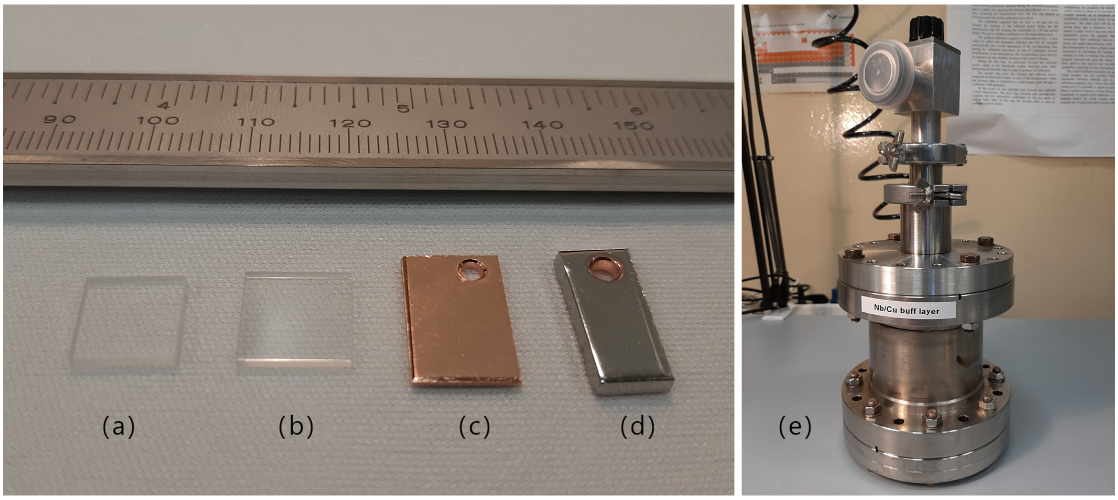

Figure 5.9: *Substrates used: (a) quartz 9X9 mm, (b) sapphire 10X10 mm, (c) copper, (d) Nb/Cu and (e) the low vacuum vessel in which Nb/Cu are stored.*

5.4 Axion cavity preparation

The haloscopes are composed of two identical half cells and are machined from a OFHC copper piece. They present a cylindrical part that is coated with the SC film and two conical endcaps that remain uncoated to reduce the current dissipation in the MW regime. The quality factor of this hybrid (SC and NC) cavity is

$$\frac{1}{Q_0} = \frac{1}{Q_0^{NbTi}} + \frac{1}{Q_0^{Cu}} \tag{5.1}$$

The maximum value that can be obtained with this geometry is limited to approximately 10^6 by the uncoated copper cones, since the cylindrical part is assumed to have $Q_0^{NbTi} \longrightarrow \infty$. The 9GHz cavity has a volume of 36.4 cm^2 and the cylindrical part of 26 mm in diameter and 50 mm long. To avoid the deposition of the conical parts, two conical masks are employed; they have been previously with a NbTi layer to avoid copper-copper contact, that, at high temperature, would cause the bonding of the cones to the cavity. They are displayed in figure 5.10.

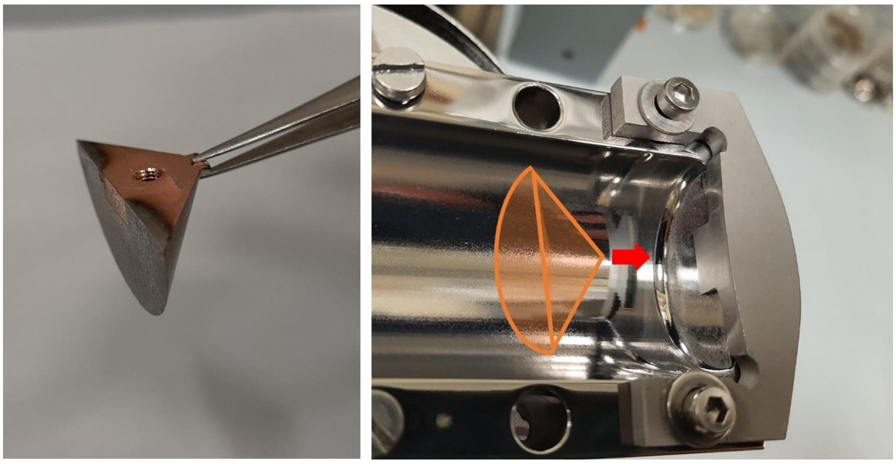

Figure 5.10: *Axion cavity cones used to mask the conical part of the half cell.*

Surface preparation is of extreme importance in the RF performance of a resonator [75, 76]. Damages and defects remaining after the machining have to be eliminated in order to obtain a smooth surface and minimize the roughness.

During this work four axion cavities have been coated with NbTi: two with resonance frequency of about 9GHz and other two of about 7GHz. One 9GHz haloscope had been already coated and tested in 2019 [9], so it had to be stripped from the existing film; the 7GHz have never been coated, so the chemical treatments are the same except from the stripping step.

The stripping process consist in removing the NbTi coating without etching the copper substrate. This has been with an industrial solution based on the industrial chemical "strip AID" and a HF:HBF$_4$ solution. It is found that in 3-4 hours approximately 4 μm of film are removed and the attack on copper is negligible.

Afterwards, the electro-polishing is performed. This process consist in the removal of copper from the damaged surface to decrease its roughness. The half-cell is placed in an electrolytic solution of phosphoric acid and buthanol in a 3:2 ratio. The half-cell is at anodic potential and a copper cathode is placed near the cylindrical surface, shown in figure 5.11 (a). In this step between $100 - 200$ μm are removed [77, 78]. Following, a chemical polishing is carried out. The procedure uses the chemical solution SUBU5, as for the planar samples. Finally, the half-cell is treated with a jet of deionized water at high pressure (HPR) to remove chemical residues an particles and rinsed with ethanol. Note that the polishing and HPR steps are performed just prior to mounting the half-cell in the vacuum chamber. The final result of the polishing steps is shown in figure 5.11 (b).

5.5 Characterization methods

The samples prepared in this work are characterized with the available instruments at LNL. In the following, the methods used are briefly outlined.

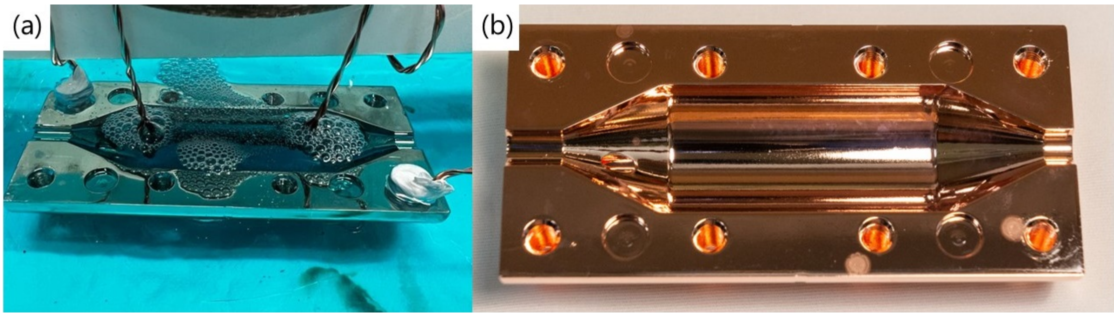

Figure 5.11: *(a) 9 GHz axion cavity half-cell undergoing electro-polishing. (b) the same half-cell after the polishing steps.*

5.5.1 Profilometer

The Veeco Dektak 8 is a profilometer used to measure the thickness of the film and calculate the deposition rate. Flat and low roughness substrates, like ceramics as quartz and sapphire, are preferable for these measurements. An uncoated region is used as reference for the profile of the film. The thickness is estimated by averaging the values obtained in three or four different places of the sample, the estimated error is about 0.3 μm. In figure 5.12 the profilometer station is shown.

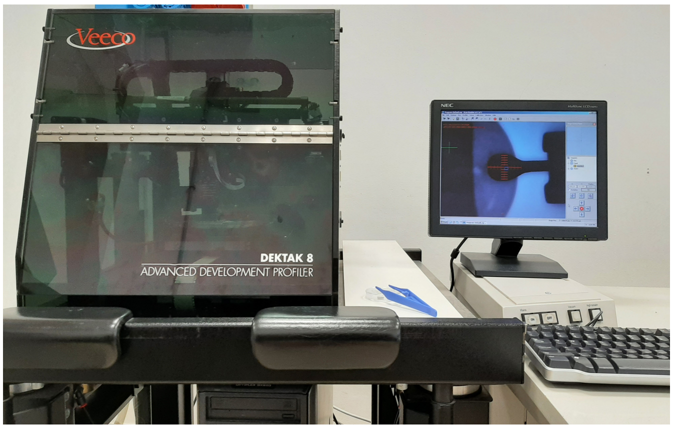

Figure 5.12: *The Veeco Dektak profilometer used at LNL.*

5.5.2 SEM-EDX

Electrons have a De Broglie wavelength shorter than visible light and they are used in microscopy techniques to achieve higher spatial resolution, hence, higher magnifications than with visible microscopy. A Scanning Electron Microscope uses a beam of electrons, typically generated by a tungsten filament (via thermo-ionic emission) or a field emission gun, to obtain an image of a sample's surface. The beam is accelerated, and passes through electromagnetic lenses that focus it before scanning the surface of interest. These primary electrons interact with the core electronic levels of atoms in the specimen and the process generates a series of signals that can be analyzed to reconstruct an image or to obtain an elemental characterization. The interaction volume has a drop-like shape an grows when increasing the electrons energy.

Secondary electrons are commonly used to visualize the morphology, they escape from a thin superficial layer with energies below 50 eV. Also back-scattered electrons are useful to obtain an image with atomic mass contrast. Auger electrons and x-rays are generated when a core vacancy (caused by a primary electron) is compensated by a higher level electron, the energy difference can be either released as a x-ray photon or transferred to another electron which escapes the material. Both are specific of every element and can be used for an elemental characterization.

Energy Dispersive X-ray Spectroscopy (EDX-EDS) analyzes the characteristic x-rays emitted from a sample. From the ratio of the peaks intensity it is possible to calculate the atomic, or weight, percent of the elements in the sample [79].

In this work a Coxem CX-200Plus SEM equipped with an EDX Bruker X-Lash Detector 410-M have been used; shown in figure 5.13. The reported images are taken with secondary electrons at magnification of X500 and X1000. The EDX analysis for the film composition have been done in regions without defects. Other features of the samples have been analyzed locally with an accelerating voltage (AV) of 10 kV, in order to obtain a signal as close as possible to the surface.

To estimate the composition of both NbTi and Nb_3Sn, reported in weight percent of Ti and atomic percent of Sn, multiple parts of the samples have been analyzed and the reported values are the mean of the ones taken with AV at 10 and 15 kV. This is done to have information about the near surface, since the AC field only penetrates in the surface. The error is taken as mean error.

The depth profiles of copper contamination have been obtained by changing the AV from 10 to 25 kV. The EDX dedicated software reports the interaction depth once the composition has been determined. The values reported are the average, and the standard deviation, of the ones taken in different regions of the samples.

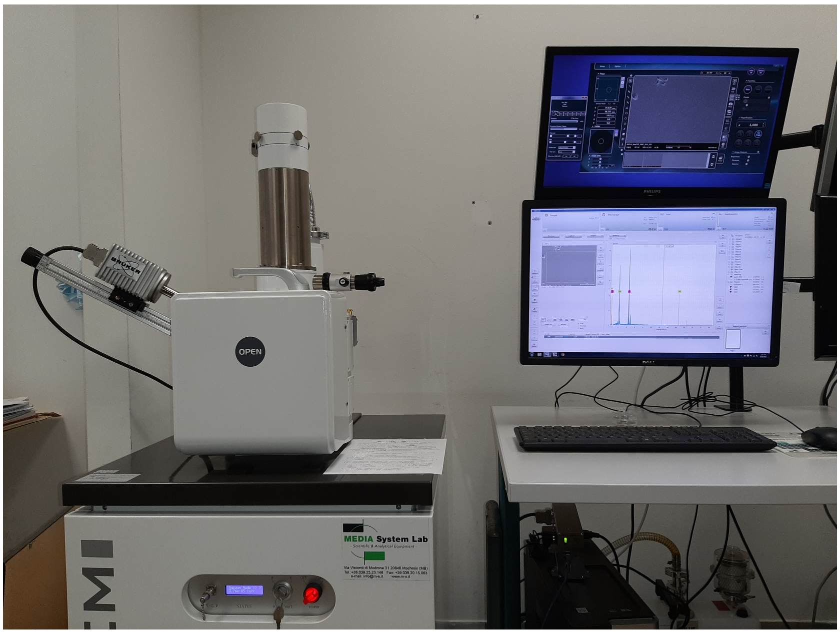

Figure 5.13: *The COXEM CX-200Plus SEM.*

5.5.3 X-ray diffraction

X-rays with wavelength of the order of 1 Åare a useful tool to investigate the structural properties of solids via a diffraction technique: X-ray Diffraction (XRD). Diffraction occurs in crystals because the interatomic distances have the same order of magnitude of x-rays wavelength. More precisely, a monochromatic beam of x-rays is scattered by each atom's electronic density in a crystal plane and the scattered waves interfere with each other. The famous Bragg's law describes the conditions necessary to have constructive interference

$$n\lambda = 2d_{hkl}\sin\theta \tag{5.2}$$

where n is an integer, λ is the x-ray's wavelength, d_{hkl} is the distance between planes orientated in the (hkl) direction in the reciprocal lattice and θ is the diffraction angle. With this it is possible to determine the crystal structure and the dimension of the unit cell.

The broadening of the diffraction peaks are caused by deviation from an ideal single crystal. The Sherrer equation correlates the broadening to the grain size L in a polycrystalline specimen

$$\beta = \frac{K\lambda}{L\cos\theta} \tag{5.3}$$

where K is a shape factor equal to 0.94 for cubic structures, λ is the wavelength of the radiation, L is the grain size and θ is the diffraction angle [80].

In this work, the XRD profiles of NbTi and Nb_3Sn thin film samples have been acquired with a Cu (K_α) radiation source Philips X'Pert diffractometer and analyzed with Malvern Panalitical's HighScore Plus software. The incident angle is fixed at 5° in order to have a X-ray penetration depth, calculated with the MAC tool of the software, of about $1.2\mu m$ for Nb_3Sn and about $1.8\mu m$ for NbTi. The 2θ angle is scanned from 30° to 90°: a range in which Nb_3Sn and NbTi exhibit their major reflections. In figure 5.14 the workstation and the diffractometer used are shown.

Figure 5.14: *The Philips X'Pert diffractometer at LNL.*

5.5.4 Critical temperature

The critical temperature gives information on the quality of SC films. At LNL, it can be measured by detecting the resistance drop with a four point probe or with an inductive method. However, the former is applicable only to films deposited on insulators, otherwise the resistivity of the NC substrate, like copper, would render invisible that of the SC film.

The inductive method exploit the Meissner effect: the sample is placed between two coils one of which, named *drive coil*, generates an AC magnetic field that permeates the sample; the other, named *pick-up coil*, collects the induced voltage signal. This system allows to measure the T_c of samples deposited also to NC substrates.

A sinusoidal signal is generated by a current source Keithley 6221A, the pick-up coil signal is measured by a Ametek 7270DSP lock-in amplifier. These two signals can be monitored by a Tektronix DPO 3052 oscilloscope. The temperature is monitored by a Cryocon18c. These instruments are interfaced with a dedicated software [81]. In figure 5.15 the inductive system is shown.

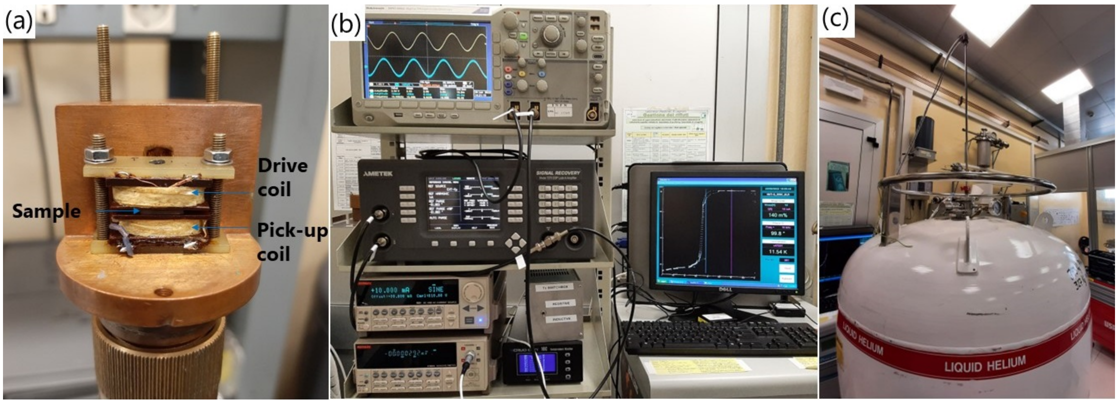

Figure 5.15: *Inductive T_c measurement system at LNL. (a) coils and sample placement, (b) instrumentation (c) dip-stick inserted in the LHe dewar.*

In the used configuration, the sample is placed with the coating facing the drive coil and the substrate is in contact with the Cernox® thermometer located in the pick-up coil. The coils, the thermometer and the sample are placed in a copper head that is then inserted and lowered in the liquid helium (LHe) dewar to cool down with the He vapours without an applied field - to avoid flux trapping in possible defects present in the material. Once a sufficiently low temperature is reached, the system is left to stabilize for several minutes, then, the measurements begins. The acquisition rate is set to 5 Hz and, depending on the substrate, the parameters for the sinusoidal signal generation are set, reported in table 5.1. The temperature is raised manually by moving away the copper head from the LHe bath, the gradient obtained is approximately 1 K/min.

A low frequency is necessary for the copper substrates in order to avoid the screening of the field by means of eddy currents. At 100 Hz the skin depth of copper is around 7000 μm, so it is an appropriate frequency for 4 mm thick samples.

The dataset extrapolated from the software after a T_c measurements consist of the temperature measurements and the pick-up coil voltage, both are related through a *time-stamp*, which is the time reference. Through this, the plot of voltage as a function of the temperature is obtained.

Substrate	Peak current (mA)	Frequency (kHz)
Dielectric	20	10
Copper	50	0,1

Table 5.1: *Parameters for the inductive T_c measurement on the two types of substrate. For the Nb/Cu samples, the same parameters as "Copper" have been used.*

The most common method for analyzing the transition curve is the 10-90% criterion, but there is not a well established methodology for it [82]. Since the software used for the measurement has revealed to be unreliable in the determination of T_c and ΔT_c, in this work a particular 10-90% procedure has been adopted. Referring to figure 5.16, three linear interpolation can be done in the transition curve: one in the normal conducting region (a), one in the superconducting region (b) and a last one in the transition region (c). The number of points used for the interpolation is arbitrary. The "intensity" of the transition, set to be 100%, is determined by the ordinates' difference of the intersection points between $a-c$ (P) and $b-c$ (Q). The fit curves a and b are then translated to 90% ($a_{90\%}$) and 10% ($b_{10\%}$) of the transition - basically recalculating their intercept. The width of the transition ΔT is determined by the abscissae's difference of the intersection points between $a_{90\%} - c$ (P') and $b_{10\%} - c$ (Q')

$$\Delta T = x_{P'} - x_{Q'} = T_{90\%} - T_{10\%} \tag{5.4}$$

Finally, the value of T_c is calculated as the midpoint of the transition

$$T_c = T_{10\%} + \frac{\Delta T}{2} \tag{5.5}$$

The system's temperature error is calculated as the difference between the maximum and minimum value read a in a time-span of 30 seconds, resulting in a $\delta T \simeq \pm 6\ mK$, see figure 5.17.

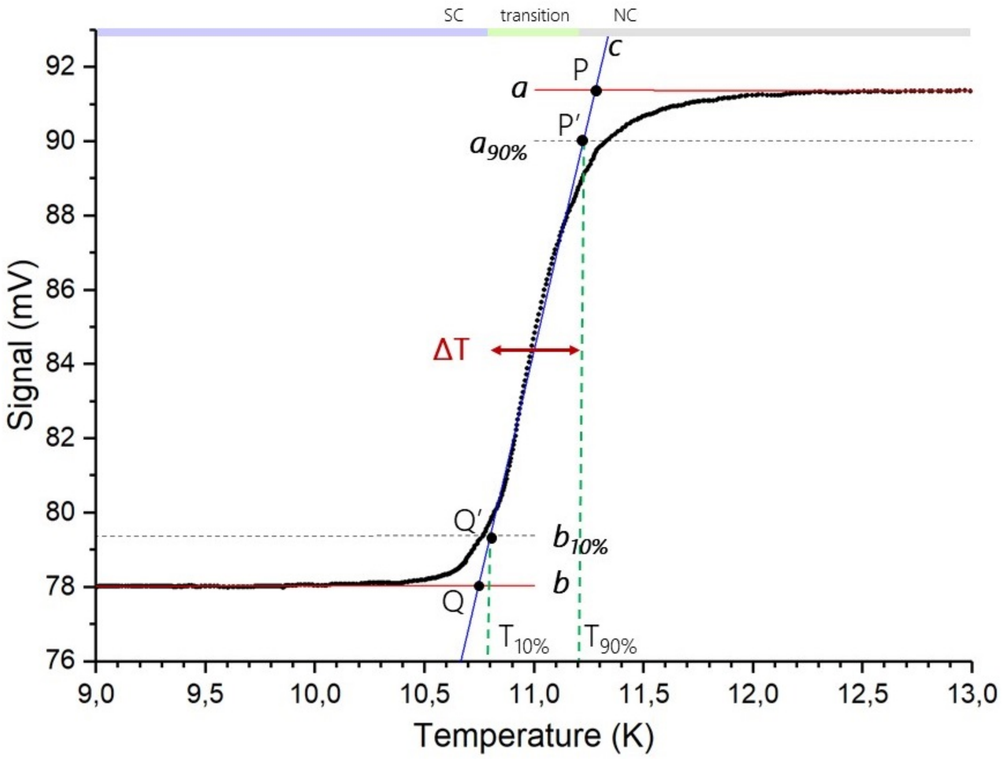

Figure 5.16: *Example of SC transition curve with explicit linear regression plots and points of interest for evaluating the critical temperature T_c and its width ΔT.*

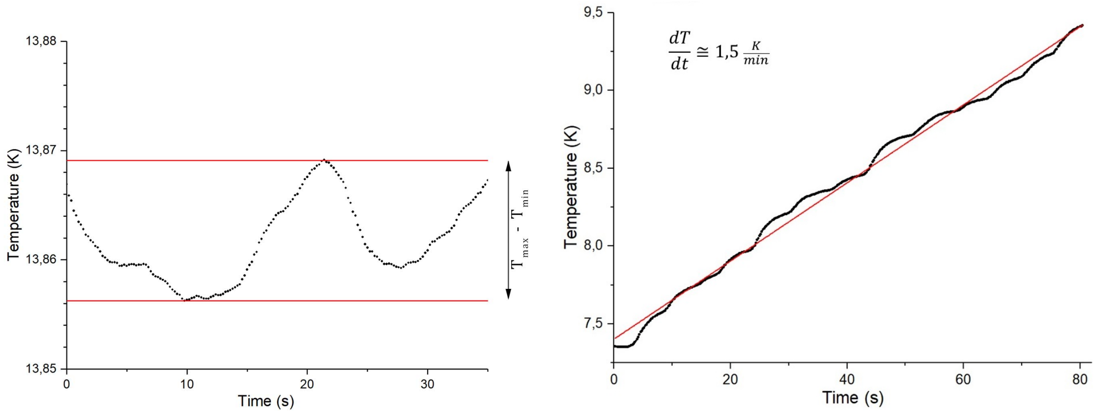

(a) **(b)**

Figure 5.17: *(a) inductive T_c system temperature error, it results to approximately $\delta T = \frac{T_{max} - T_{min}}{2} \simeq \pm 6\ mK$. (b) temperature gradient used during a T_c measurement: $\frac{dT}{dT} \simeq 1.5\ Kmin^{-1}$.*

6
Results and discussion

In this chapter, the results obtained from the performed analyses are reported and discussed. The chapter is divided in two main sections: the former regards the NbTi coatings on planar samples and haloscopes and the latter the Nb_3Sn coatings.

Some NbTi and Nb_3Sn samples were sent to Helmholtz Zentrum Dresden Rossendorf (HZDR), Germany, for RBS and PIXE characterization in the framework of the I.FAST international project. The data reported are kindly provided by Dr. Zhou Shengqiang. Both techniques use high energy ions - in the order of MeV - impinging on the material in analysis. The Rutherford Backscattering Spectrometry (RBS) analizes the incident ions scattered at high angles, typically 170°. The ion-nucleus interaction is considered as elastic scattering and is governed by the Rutherford cross section $\sigma(\theta) \propto (\frac{Z_a Z_b}{E_0})^2 sin^{-4}(\theta/2)$, where Z is the atomic number of the ion and nucleus respectively, E_0 is the incident ion energy and θ is the scattering angle. The energy of the scattered ion E_1 depends on the scattering constant K: $E_1 = K(m_a, m_b, \theta)E_0$ which depends only from the mass of the ion and nucleus interacting and from the scattering angle. The Particle Induced x-ray Emission (PIXE) analyzes the characteristic X-ray lines emitted from the inner shells of ionized atoms by energetic ionized particles. The emission of x-rays is related to the fluorescence yield: the probability of having a radiative relaxation process relative to all the possible transitions [83]. The RBS and PIXE signals have been collected simultaneously with He^{++} ions accelerated at 1.7 MeV. Moreover, cross-sections created with the Focused Ion Beam (FIB) of the samples are in program at HZB. This technique allows to obtain a clean section of the films without mechanical machining that can cause cross contamination.

6.1 NbTi coatings

In this work, some tests on planar samples - quartz, copper and niobium on copper (Nb/Cu) - have been done to optimize the coating procedure for axion haloscopes. In total, four haloscopes have been coated with NbTi, two with a nominal frequency of 9GHz and two with frequency of 7GHz. Moreover, one of the former has been coated with a $1\mu m$ thick Nb interlayer.

In the following, the results for the NbTi coating development are reported. First the results for the planar samples are discussed, then some results for the haloscopes produced are reported.

6.1.1 Planar samples

A first deposition have been performed with the in-house magnetron in order to simulate the conditions used to coat a 9GHz haloscope in 2019. The old target was thinned and bent through the many sputtering processes it had undergone, this comported a non uniform contact with the magnetron's base-plate, hence poor electrical and thermal conductivity. As a result, the power supply reached its upper voltage limit and could not ignite the plasma with the current set to 1.0 A (the current value used in 2019); so it was lowered to 0.5 A. After that process, the new magnetron equipped with the new target was installed. The parameters of the depositions are summarized in table 6.1. The deposition time varies with the deposition rate, so it is adjusted to obtain a the desired film thickness. On average, 40 minutes were sufficient to deposit about 2.5 μm.

For conciseness, the samples are identified by the coating parameters: substrate temperature and magnetron current.

	OldTGT (2019)	OldTGT (2022)	NewTGT
Current (A)	1.0	0.5	1.5
Current density ($mA\ cm^{-2}$)	12	6	19
Ar Pressure ($mbar$)	8×10^{-3}	8×10^{-3}	6×10^{-3}
Substrate temperature (°C)	550	550	450 500 550
Baking time (h)	> 24		
P pre-deposition (mbar)	$< 9 \times 10^{-8}$		
Base P (mbar)	$< 9 \times 10^{-9}$		

Table 6.1: *Coating parameters for the NbTi planar samples.*

Quartz substrates

From the SEM micrographs on quartz substrate 6.1, the films appear smooth and almost free of defects. In figure 6.2 is reported the critical temperature in function of the composition for the quartz samples. The composition, determined by EDS, ranges between 46 and 53 wt% of Ti, which is in the eligible range for the highest B_{c2}. An old sample - coated in 2019 with the old target - was analyzed, resulting in the lowest Ti content. The sample coated in similar conditions presents a higher Ti content even though the used current density is lower. The samples coated with the new configuration at different temperature present a similar composition between *52 and 53 wt%* of Ti. It can be seen form these samples that the temperature seem to have little to no effect on the T_c . Overall the critical temperature measurements are in good agreement with the predicted values [29].

In the XRD diffractograms reported in figure 6.3, only the NbTi phase is visible. The sample coated in 2019 (550°C 1.0A) present the (011) and (002) reflections dampened, but the (022) peak has an intensity similar to the other samples. This is strange since the (022) is oriented in the same crystallographic direction as the (011) but with half

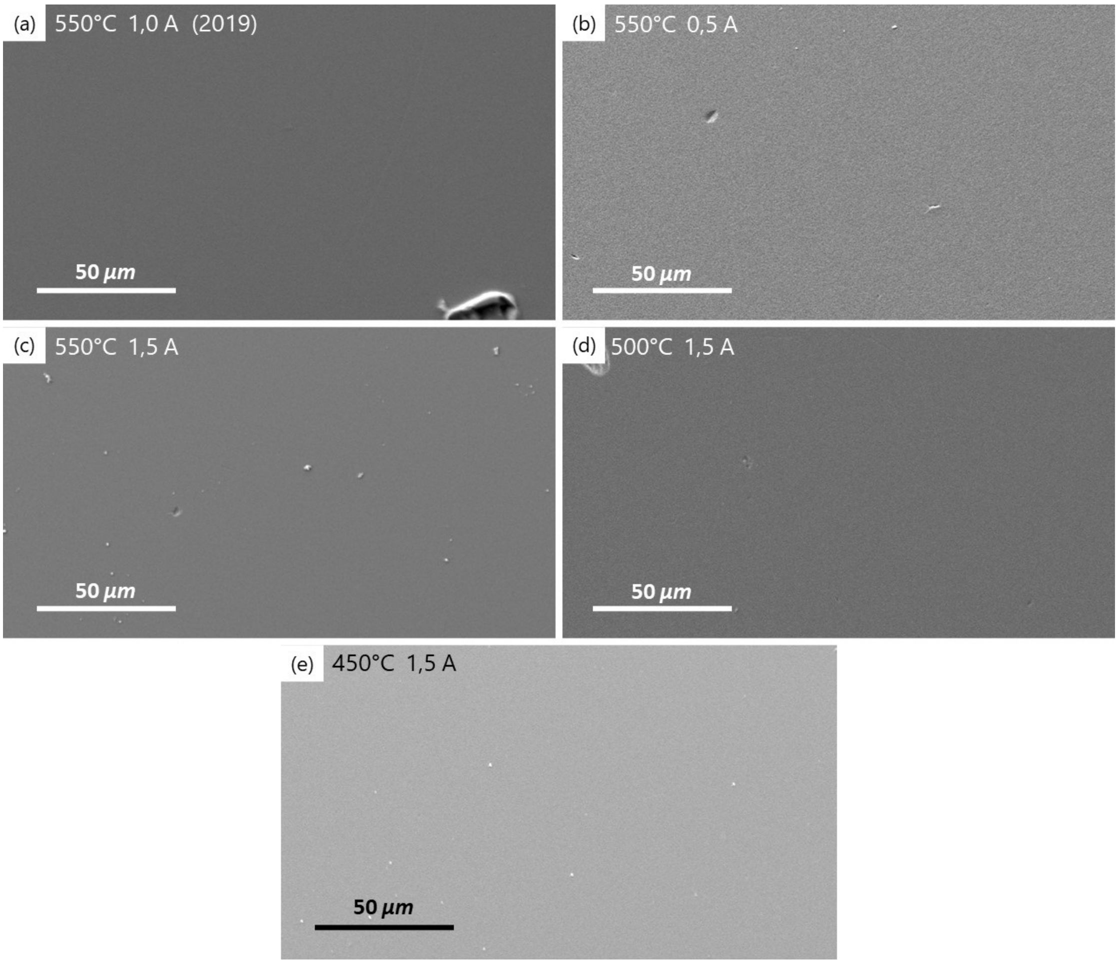

Figure 6.1: *SEM micrographs of the NbTi on quartz samples. (a) 550°C 1.0 A (b) 550°C 0.5 A (c) 550°C 1.5 A (d) 500°C 1.5 A (e) 450°C 1.5 A. The films appear smooth and almost defect free.*

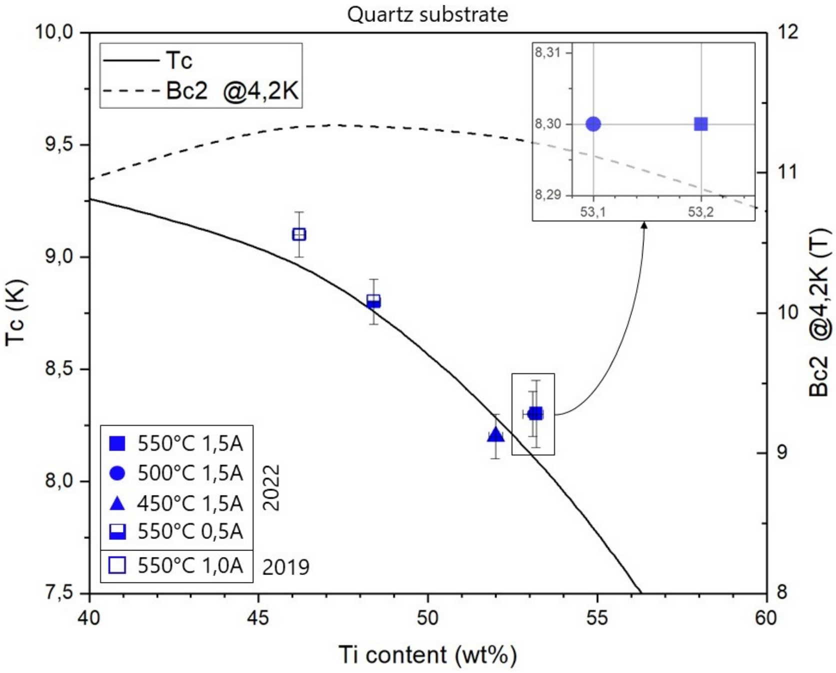

Figure 6.2: *Critical temperature as a function of the composition (weight percent) of the planar samples of NbTi deposited on quartz. The two points in the left part are coated with the older target, the ones on the right are coated with new target. The* T_c *and* B_{c2} *trends are adapted from* [29].

lattice distance and is visible at high angles ≃ 83°, whereas the (011) is the most intense peak in NbTi and visible at ≃ 39°. This could be caused by the different deposition conditions used. Overall, the peaks of every samples are shifted at higher 2θ suggesting that the film is under compressive strain.

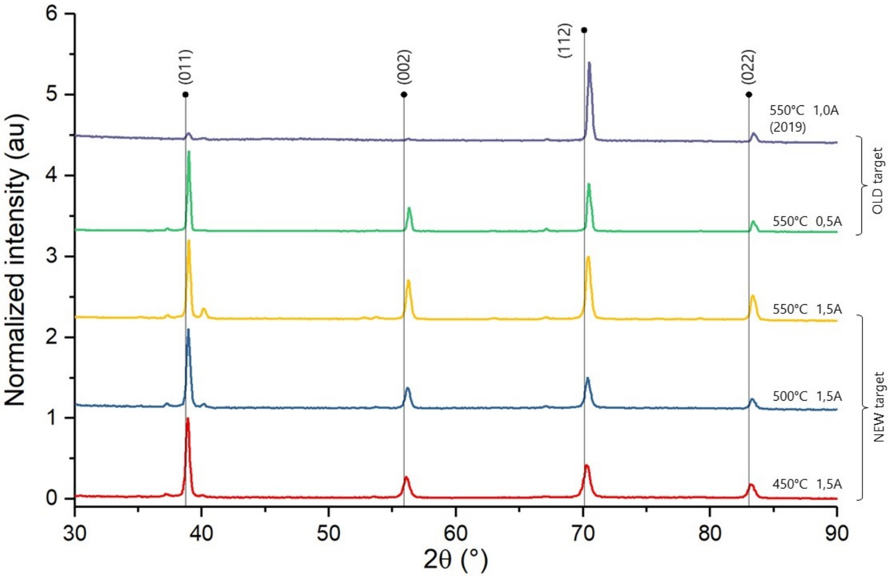

Figure 6.3: *XRD diffractograms of the quartz planar samples. The black dots represent the NbTi peaks. The sample coated in 2019 present the (011) reflection dampened probably due to the different coating conditions.*

Copper substrates

On copper substrate, figure 6.4, the films appear rougher than on quartz but do not present signs of delamination. The roughness is caused by the substrate, which had been only lightly polished with a chemical polishing, as described in section 5.3. On the sample deposited at 450°C - with the new target - figure 6.4(d), some spots are visible. An EDS analysis reveals that they do not differ in composition from the film and no Cu inclusions, or other contaminants, are present.

In figure 6.5 is reported the critical temperature in function of the composition for the copper samples. No samples from 2019 were available but the Tc has been extrapolated in [84] to be 8 K; the composition is considered similar to that measured in the quartz sample: 46 *wt%* of Ti (see previous paragraph). The one made with similar parameters present a Ti content of about *47.5 wt%*, in line with the quartz sample coated in the same run. However, no T_c was detected. The samples coated with the new target are in the same range of composition and critical temperature - between *8 and 8.5 K* - as the quartz ones. Also, the Tc of the 7GHz axion cavity coated in this work has been measured to be 8.3 K (see paragraph 6.1.3), which is in line with the measurements on the planar samples; also in this case, since it was not possible to perform a direct measurement of the composition, it is considered in the range of the copper samples measured. The T_c -composition trend is respected although more scattered compared to the quartz substrate. On copper, the deposition temperature seem to have an impact on both the composition and T_c : an increase in temperature results in a higher Ti content and T_c . However, since this is not observed on quartz - which allows to discriminate the quality of the film alone, without the influence of the copper - this could be a substrate effect caused by imperfections in the copper.

Given the high deposition temperature, interdiffusion of the two layers is expected. As it can be seen in figure 6.6 every film deposited on copper present Cu contamination starting from approximately 1 μm from the surface. The profiles of the 550°C 1.5A

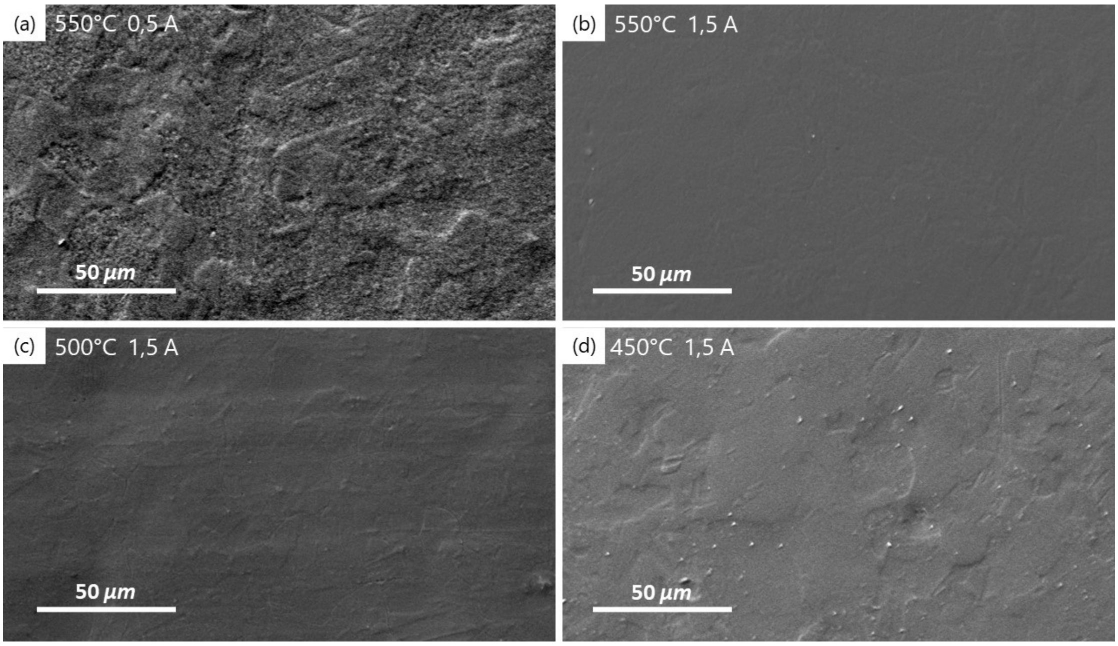

Figure 6.4: *SEM micrographs of the NbTi on copper samples: (a) 550°C 0.5 A (b) 550°C 1.5 A (c) 500°C 1.5 A (d) 450°C 1.5 A. The films appear rough, probably caused by the substrate.*

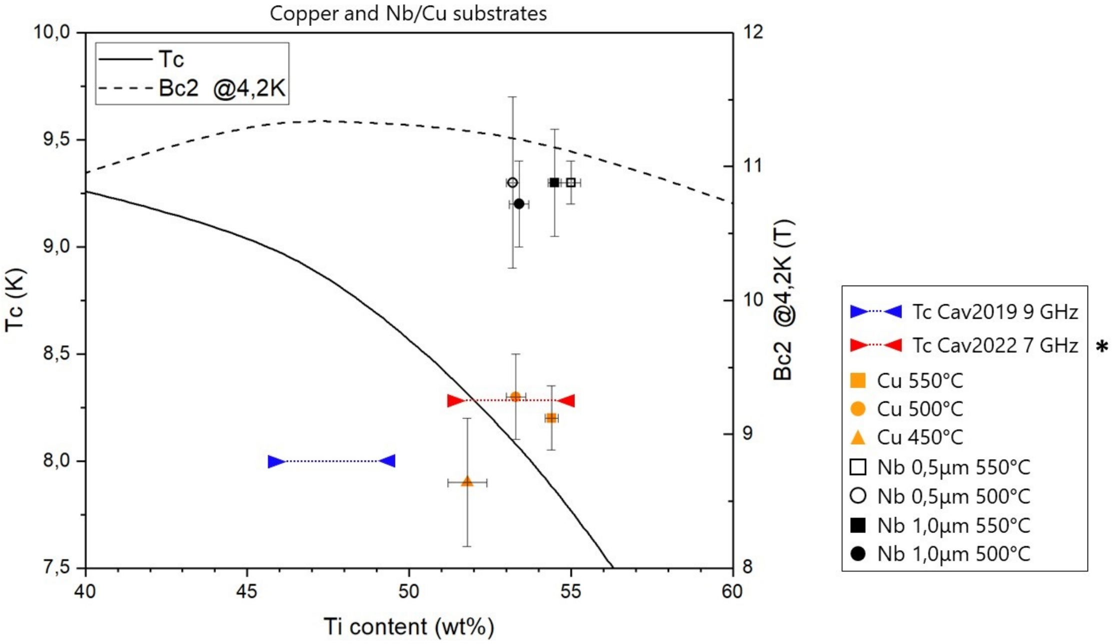

Figure 6.5: *Critical temperature as a function of the composition (weight percent) of the planar samples of NbTi deposited on copper (orange) and Nb/Cu interlayer, of* $0,5$ μm *(black, open symbols) and* 1 μm *(black, closed symbols). The Tc of the haloscope coated in 2019 and the 7GHz one are also reported; blue line and red line respectively, the composition is assumed in the range of other samples. * from* [84]. *The Tc and* B_{c2} *trends are adapted from* [29].

sample show a higher concentration of copper than the 500°C one, but the 450°C sample do not have a lower concentration, on the contrary it has a profile similar to the 550°C 1.5A. The 550°C 0.5A sample present a profile in between the others, meaning that the current, hence the deposition energy, is contributing to the diffusion: a lower current results in less energetic vaporized atoms that collide on the substrate's surface.

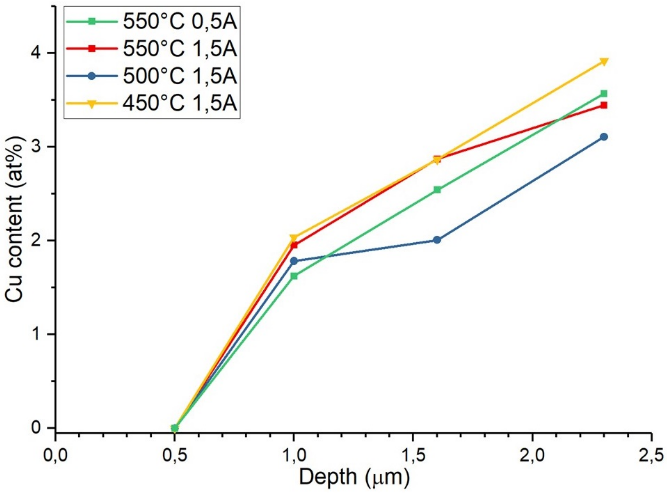

Figure 6.6: *Copper interdiffusion profiles for the samples deposited on copper. The film thickness is approximately* 2.5 μm.

The depth profiles are obtained changing the SEM accelerating voltage and a signal from 0.5 μm is generated by $10 kV$ for NbTi. Note that at a depth of 0.5 μm, no copper is detected by the EDS. Since the most intense x-ray emission line for Cu is its $K_\alpha \simeq 8\ keV$ - which is close to the exciting electrons' energy - the signal could be too low to be detected. A more surface-sensitive technique (*i.e.* XPS or RBS) would be appropriate to quantify the surface's composition.

The XRD diffractograms are reported in figure 6.7. In every sample the NbTi reflections are visible, but also those of copper. This confirms the presence of Cu in the film, and the need of a diffusion barrier. The 450°C sample shows an extremely intense copper reflection at 43° - even more intense than the NbTi (011) - which is in line with the unexpected copper content detected with the EDS. The NbTi peaks are shifted at lower 2θ, so the film is now under tensile strain: the opposite case as observed on quartz. This is due to the smaller lattice parameter compared to the Cu substrate: NbTi has $a_{NbTi} = 3.286$ Å whereas ($a_{Cu} = 3.617$ Å). Overall, the preferred orientation is the same as the quartz sample: the (011) plane.

To resolve Cu diffusion problem, the approach of an interlayer that acts as diffusion barrier has been adopted. The material used was niobium, which has already been proved to avoid the formation of Cu-Ti intermetallic compounds during the heat treatment of fine filament NbTi wires in copper matrix [85].

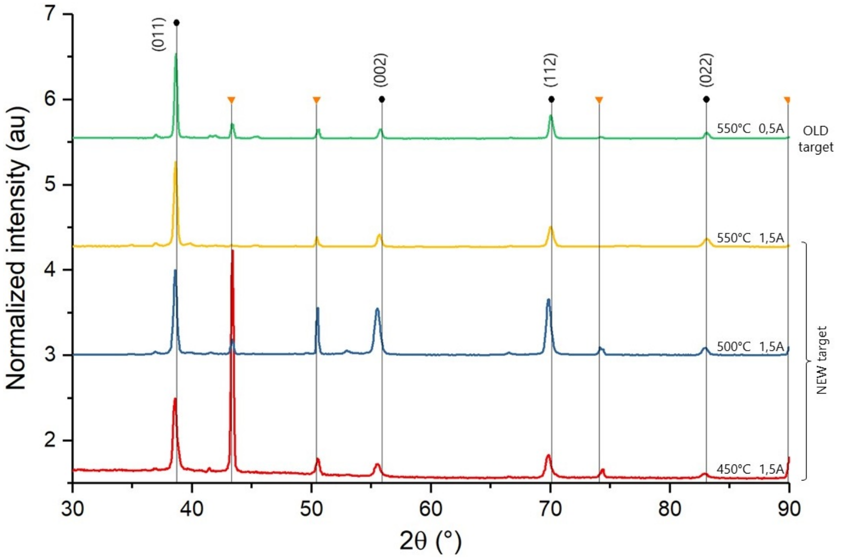

Figure 6.7: *XRD diffractograms of the copper planar samples. The black dots represent the NbTi peaks and the orange triangles the copper peaks.*

Nb/Cu substrates

The niobium diffusion barriers consist of a film of niobium deposited via DCMS in the vacuum system used for the NbTi coatings with the same sputtering source. Two thicknesses have been investigated: 0.5 μm and 1.0 μm, the deposition parameters are reported in table 6.2.

Baking time (h)	> 24
P pre-deposition (mbar)	$< 9 \times 10^{-8}$
Base P (mbar)	$< 9 \times 10^{-9}$
Current (A)	1.5
Current density ($mA\ cm^{-2}$)	19
Ar Pressure ($mbar$)	6×10^{-3}
Substrate temperature (°C)	550

Table 6.2: *Coating parameters for the Nb diffusion barrier layer.*

The NbTi films have been deposited on the Nb/Cu interlayer at two temperatures: 500°C and 550°C. From the SEM micrographs, figure 6.8, the films are not delaminated and the roughness is again caused by the copper substrate. On the sample coated with the 0.5 μm Nb interlayer at 500°C, some spots are visible. They present a different composition with a lower content of Ti (about 35 wt%).

In figure 6.5 the critical temperature in function of the composition is reported. The Ti content is in line with that of the copper samples: for the one coated at 500°C about 53 wt% and for the 550°C 55 wt%. The critical temperature, on the other hand, is higher than the predicted value for that composition. It is actually very similar to the T_c of pure niobium (9.3 K) and in the T_c measurements for NbTi a double transition is not visible, meaning that the transition of the Nb interlayer masks that of NbTi. A more detailed discussion on the critical temperature measurements is reported in section 6.3.

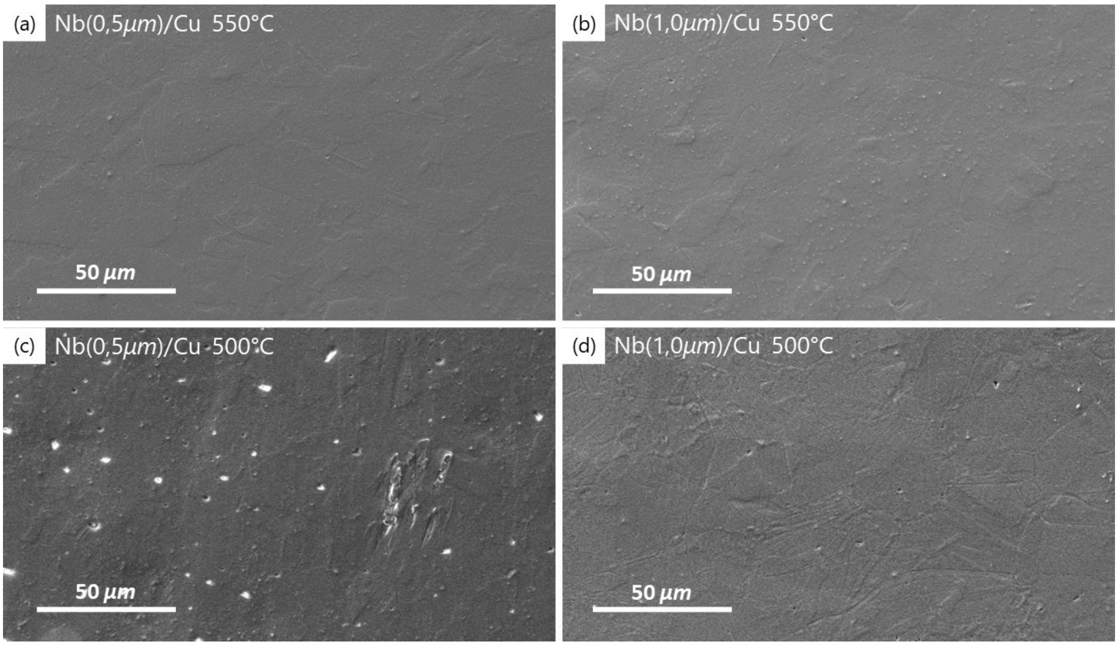

Figure 6.8: *SEM micrographs of the NbTi on Nb/Cu samples. The interlayer thickness and the deposition temperature are: (a)* 0.5 μm *550°C (b)* 1.0 μm *550°C (c)* 0.5 μm *500°C (d)* 1.0 μm *500°C. The films do not appear delaminated, the roughness is caused by the copper substrate.*

The copper depth profiles reported in figure 6.9 show that the copper diffusion is mitigated with the interlayer of niobium. For both deposition temperatures a higher thickness reduces the copper content, also it can be seen that a higher temperature results in a higher Cu content near the surface. The best result is given by the sample deposited at 500°C on 1.0 μm thick Nb layer: no copper is detected by the EDS at 1.0 μm from the NbTi surface. This could be sufficient for RF applications since the penetration depth of NbTi is about 300 nm.

The XRD diffractograms are reported in figure 6.10. They show the presence of the NbTi phase and the peaks are shifted to lower 2θ, as for the copper substrates, resulting in tensile stress of the film. The sample deposited on Nb/Cu at 550°C Present a different preferred orientation: the most intense reflection is the (002) instead of the (011) as all the other samples. Moreover, two (002) reflections related to two different emission lines are visible in between 50° and 55°. One, at 50°, is caused by the Cu K_β. The other, at 53°, is caused by the tungsten L_α line: the prolonged use of the x-ray tube caused the evaporation of W from the electron source filament that deposited on the copper anode, this makes possible the emission from the tungsten $L_\alpha = 8.40\ keV \simeq 1.476$ Å. The lattice reflection associated to this line are more visible at low angles from intense peaks and appear at lower 2θ than the analogous produced by the Cu K_α.

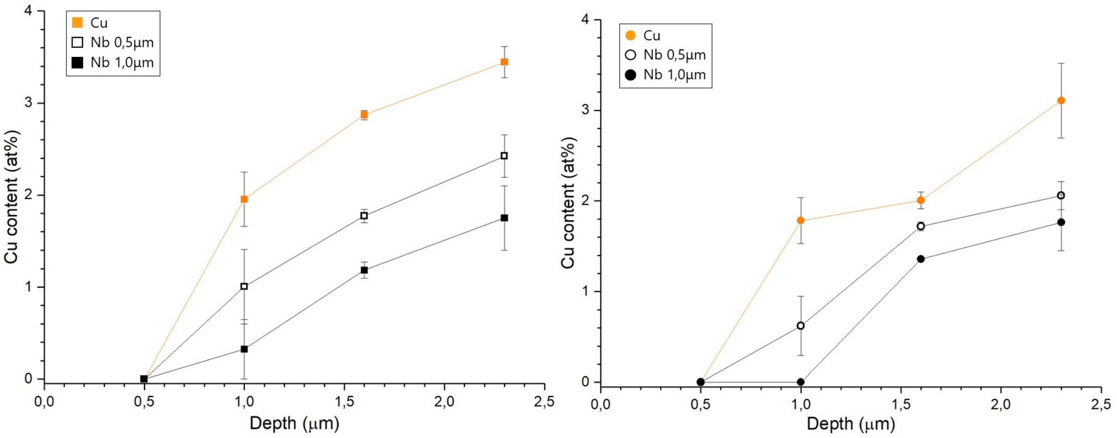

(a) Cu and Nb/Cu at 550°C **(b)** Cu and Nb/Cu at 500°C

Figure 6.9: *Copper interdiffusion profiles of the Nb/Cu samples. (a) coated at 550°C and (b) coated at 500°C. The film thickness is approximately* 2.5 *µm.*

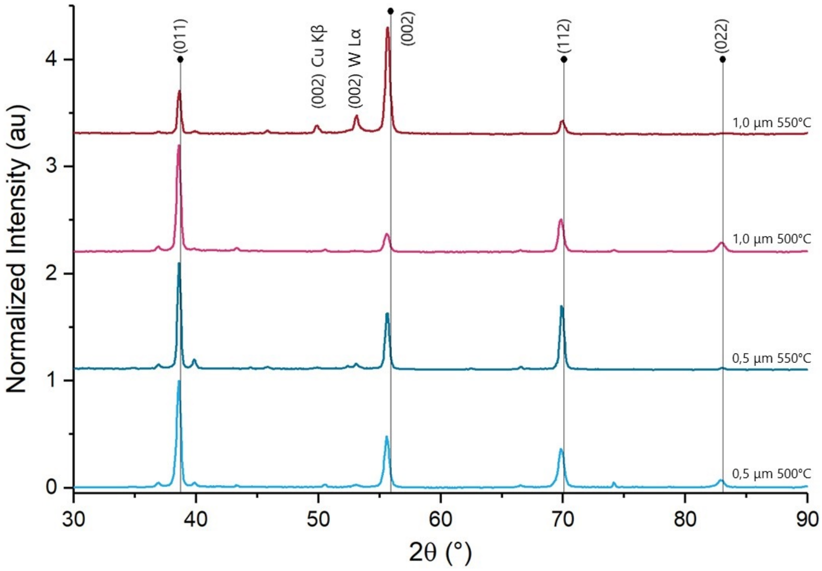

Figure 6.10: *XRD diffractograms of the Nb/Cu planar samples. The black dots represent the NbTi peaks.*

6.1.2 RBS and PIXE analysis

The samples coated at 500°C on copper and the two Nb interlayers were characterized with RBS and PIXE analysis at HZDR. In figure 6.11 the RBS and PIXE spectra are reported. It can be seen that no copper signal is visible in the RBS spectra: if a high concentration of copper, about 5 to 10 % is present in the top 500 - 1000 nm of the sample, a step at 750 keV should be visible. From the RBS peaks intensity ratio it is possible to determine the composition, given $\mathrm{Nb}_a\mathrm{Ti}_b$

$$\frac{b}{a} \propto \frac{Y_{Ti}}{Y_{Nb}} \simeq 2.6 \left(\frac{Z_{Nb}}{Z_{Ti}}\right)^2 \tag{6.1}$$

It corresponds to an atomic Ti content of 72% which is in line with the EDS measurements of 69 at%.

In the PIXE spectra, the Cu($K\alpha$) line is visible although the signal is several orders of magnitude lower than the Nb and Ti lines. This can be explained by the high sensitivity of the technique, in the ppm range, and the small thickness of the film: the PIXE signal may arise from few microns in depth, hence the copper substrate may be excited. The signal at 7 keV is an artifact caused by the pile-up of the Nb and Ti lines and do not represent a contaminant.

From these analysis it is possible to confirm that copper does not contaminate the films surface.

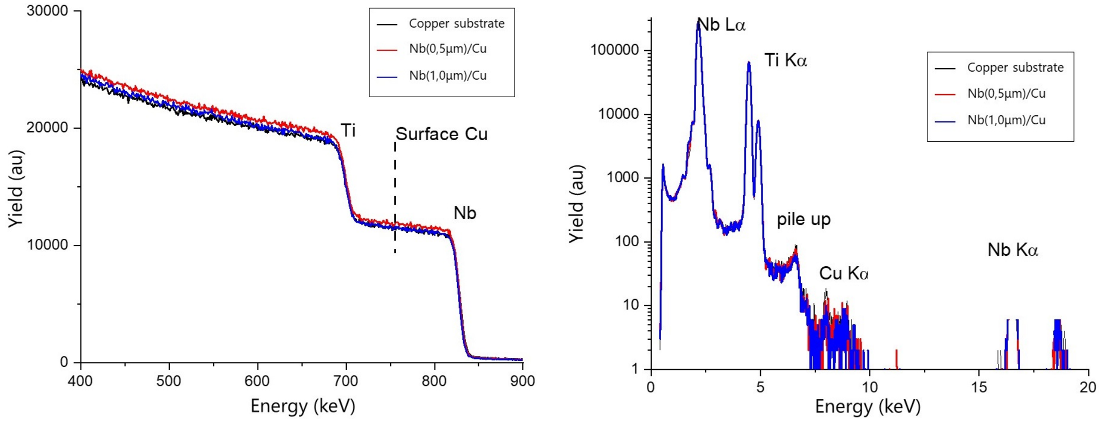

(a) RBS **(b)** PIXE

Figure 6.11: *RBS (a) and PIXE (b) spectra of the NbTi samples deposited on copper and the two niobium interlayers at 500°C. Courtesy of Dr. Zhou Shengqiang. The RBS spectra do not present the Cu signal and in the PIXE the Cu signal comes from the substrate.*

6.1.3 Axion cavities and high-B RF characterization

Each haloscope is composed by two identical half cells and have been coated one at a time. The half cell is mounted on the sample holder just after the chemical treatments to preserve the quality of the copper surface. The deposition procedure is that described in section 5.2.3; the baking temperature setpoint is reached more slowly than with other samples due to its greater mass and thermal inertia and the duration was > 48 hours. The coatings parameters are the ones in table 6.1, column "NewTGT"; the temperature chosen was 500°C. Overall, for every process, the pressure reached before the deposition was about 3×10^{-8} $mbar$ and the base pressure - after the deposition at room temperature - about one order of magnitude lower. In figure 6.12 pictures of the haloscopes' half cells are reported.

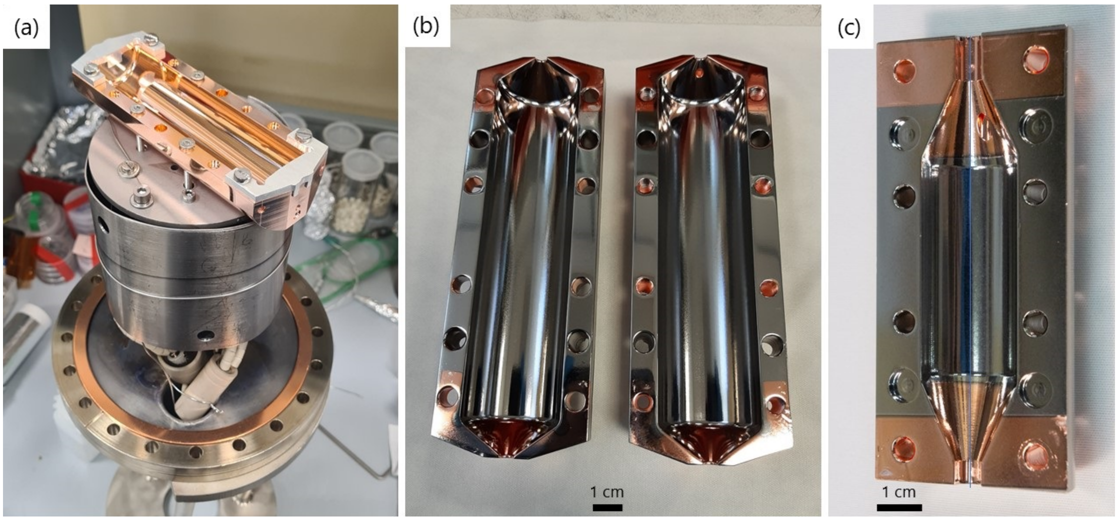

Figure 6.12: *Pictures of the haloscopes' half cells. (a) one 7GHz half cell mounted on the sample holder before the deposition; (b) both 7GHz half cells coated; (c) one 9GHz half cell coated.*

The first 7GHz haloscope has been tested in cryogenic environment and with a static magnetic field up to 11 T. The data reported have been kindly provided by Prof. Caterina Braggio and Prof. Giovanni Carugno, and have been analyzed by the author. The 9GHz haloscope coated in this work has been tested at the "COLD" lab at the National Laboratories of Frascati (LNF); the data reported has been kindly provided by Prof. Alessio Rettaroli.

The quality factor Q_0 of the 7GHz resonator has been measured as a function of the temperature and the applied magnetic field as described in [9]. In figure 6.13, the Q_0 is plotted against the temperature, without magnetic field applied ($B = 0\ T$). The intersection with the temperature axis provides an estimate of the critical temperature which is about 8.3 K. Such value is in line with the T_c measurements of the copper planar samples, figure 6.5.

As discussed in chapter 4, the quality factor is of great importance for the axion search experiments. In figure 6.14(a) the Q_0 of the 7GHz cavity is reported in function of the applied magnetic field at various temperatures. The highest value of Q_0 is $\simeq 3\times10^6$ at 4.2 K and at zero field. This value is coherent with the limits set by the copper conical parts, as discussed in section 5.4. The degrading effect of $T > 0$ is due to higher fraction of NC electrons and to the inertia of Cooper pairs in a RF electromagnetic field. These parameters are expressed in the BCS surface resistance: equation (2.27).

Another source of dissipation comes from the vortexes motion in a high magnetic field. This phenomenon is dominating the mixed state dissipation at $T \ll T_c$, where the NC fraction of electrons is negligible. In order to observe the vortex motion effect on the resonator's properties, the surface impedance can be measured. The surface impedance is field dependent: $\Delta Z_s = \Delta R_s + i\Delta X_s = Z_s(B) - Z_s(0)$ and is related to the microscopic quantity: the vortex motion resistivity ρ_{vm}. This is in turn proportional to the magnetic

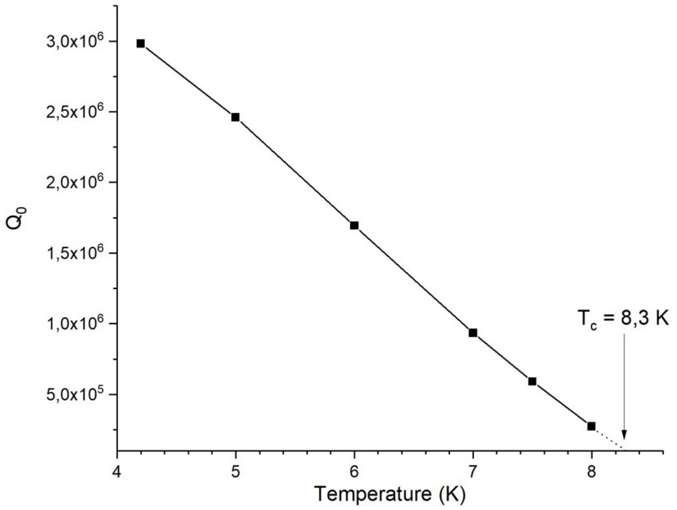

Figure 6.13: *Quality factor of the 7GHz cavity versus temperature at zero field. The extrapolated T_c is about 8.3 K.*

field B, through the Gittleman - Rosenblum model [84]. This can explain the Q-slope: an increase in the impedance - both resistance and reactance - with the magnetic field results in a lower Q_0.

In figure 6.14(b) the quality factors of different cavities is compared with the 7GHz and to the 9GHz one coated in this work; the Nb, NbTi (2019) and Cu data are taken from [84]. It is first worth to notice that the niobium cavity presents an abrupt drop in Q_0 at low field. This is of course expected since its critical magnetic field is about 0.4 T. The 7 and 9GHz (2019) NbTi cavities have a similar behaviour, the main difference being at zero field where $Q_0^{7GHz}/Q_0^{9GHz} \simeq 2$. The 9GHz (2022) cavity present worse performance than its 2019 twin: at both zero field and 5 T, it has a Q_0 almost 2 times lower, but the values are in the same order of magnitude.

Comparing the two better performing NbTi cavities with the copper reference, the improvements are clearly visible: they both present a quality factor 10 times higher at 2 T and 6 times higher at 5.5 T than copper. Also the 9GHz 2022 cavity, albeit its lower Q_0, is better performing than copper.

A key figure of merit that contributes to the detectable signal of the axion-photon coupling, recalling equation (4.5), is the product B^2Q_0. In figure 6.15 is reported such factor in function of the magnetic field. It can be seen that the 7GHz NbTi haloscope present its peak performance at 8 T (at *4.2 K*), enhancing the power signal by a factor of 10^7, approximately an order of magnitude higher than copper.

In the framework of the SAMARA collaboration, several samples have been sent to the laboratories of Roma 3 and Frascati (LNF) for high magnetic field characterization.

A sample of NbTi deposited on quartz, has been sent to the laboratories of Roma 3 for the surface impedance measurement [21]. The resulting pinning frequency for NbTi is about 7GHz, which is in line with other materials, but since there is little data in literature, supplementary studies are needed.

Another sample deposited on copper has been sent to the "COLD" lab at LNF for third harmonic AC magnetic susceptibility measurements [86], measured exposing the sample to an alternating magnetic field H_{AC} of frequency 1070 Hz and amplitude $|H_{AC}| = 10\ G$. This analysis allows to distinguish the different SC phases in the sample

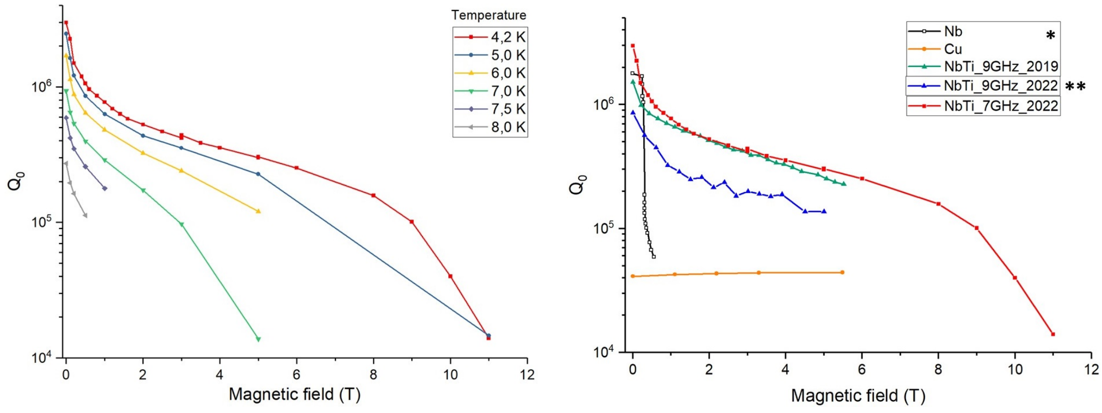

(a) **(b)**

Figure 6.14: *Q_0 versus B of (a) NbTi 7GHz cavity and (b) of various cavities for comparison at 4.2 K. * from* [84]*. ** courtesy of Prof. Alessio Rettaroli.*

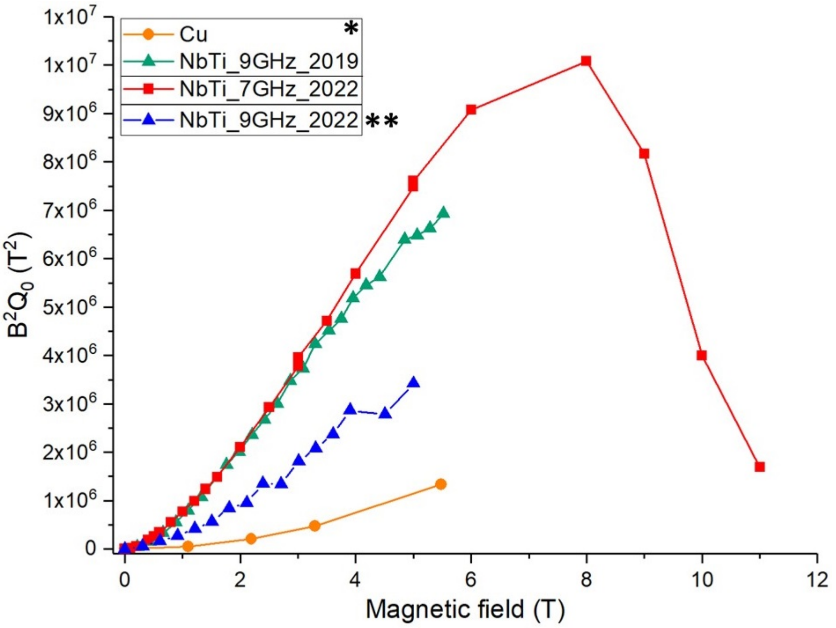

Figure 6.15: *Axion-photon coupling factor B^2Q_0 versus the applied magnetic field of various cavities for comparison at 4.2 K. * from* [84]*. ** courtesy of Prof. Alessio Rettaroli.*

as different peaks in the $|\chi_3|$ measured in function of the temperature, as it can be seen for a sample of Nb_3Sn (not part of this work) in figure 6.16(a). In figure 6.16(b) it can be seen that there are not SC phases other than NbTi, but the critical temperature estimated at zero field is lower than the inductive measurement reported above for the copper samples (figure 6.5).

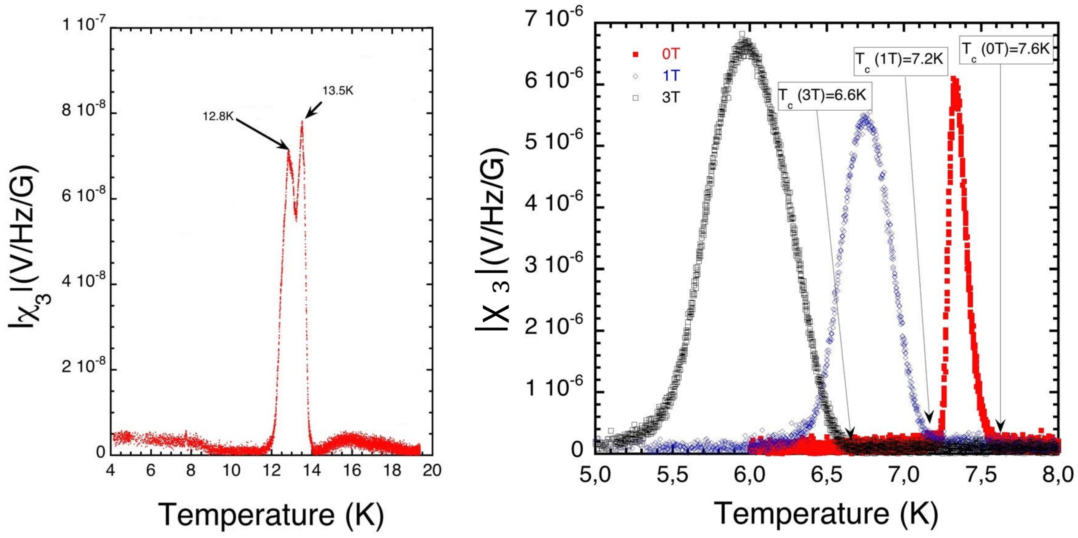

(a) Nb_3Sn **(b)** NbTi

Figure 6.16: *Third harmonic AC magnetic susceptibility of (a)* Nb_3Sn *(not part of this work) and (b) NbTi. Courtesy of Prof. Daniele Di Gioacchino.*

6.2 Nb_3Sn coatings

In this section, the results obtained from several depositions of Nb_3Sn on planar samples will be presented. Due to the necessity of high temperatures for prolonged periods of time (baking, deposition and annealing lasted from 50 to 75 hours), the vacuum system has been optimized to support such stress. In the process of doing so, some tests did not terminate successfully due to formation of leaks and to failure of the heating electronic system.

The coating parameters of the Nb_3Sn coatings are reported in table 6.3. For every process the annealing temperature is the same as the deposition. Except for the tests annealed at 750°C, for which the deposition has been done at 730°C. This was done to obtain a lower pressure before the deposition. A low current has been adopted due to the fragility of the Nb_3Sn target, which at high currents could overheat - even if cooled - and break. The deposition lasted 90 minutes and the thickness obtained is about 1.5 μm.

Baking time (h)	≥ 24
P pre-deposition (mbar)	$< 5 \times 10^{-7}$
Current (A)	0.25
Current density ($mA\ cm^{-2}$)	3
Ar Pressure ($mbar$)	3×10^{-3}, 7×10^{-3}, 2×10^{-2}
Deposition time (min)	90
Annealing temperature (°C)	550, 600, 650, 750
Annealing duration (h)	24, 48
Annealing pressure ($mbar$)	$< 9 \times 10^{-8}$
Cool-down gradient (°C/h)	30
Base pressure ($mbar$)	$< 1 \times 10^{-8}$
Thickness (μm)	1.5

Table 6.3: *Coating parameters investigated for Nb_3Sn . The annealing temperature is equal to the substrate temperature except for 750°C, where the coating T is 730°C.*

Unfortunately, after the first tests, sapphire samples were not available anymore and quartz has been used instead. But, as it will be discussed below, such samples did not present superconducting properties and the films were delaminated. The dielectric substrates are useful to eliminate the effect of a metallic substrate, however, since the objective of this work is the deposition on a metallic substrate - as a resonant cavity is - the results presented below are focused on the copper and Nb/Cu substrates.

It is known in literature that in order to obtain the correct A15 phase of Nb_3Sn high temperature are necessary even in energetic deposition process, such as DC magnetron sputtering, [45]. Also a subsequent thermal treatment shows improvements on the film morphology [46].

6.2.1 First tests

A first deposition has been done on quartz, sapphire and copper samples without annealing at $7 \times 10^{-3} mbar$ and 730°C.

As it can be seen in figure 6.17, the quartz samples presents a film extremely delaminated. This is due to the $\alpha - \beta$ transition, known as quartz inversion, that occurs on quarts at 575°C. This process is associated to an abrupt chance in volume of about

4% [87], resulting in a severe delamination and cracking of the coating. For this reason, no SC transition has been detected and the quartz substrates are excluded from further investigation.

The copper sample presents Cu inclusions in between the grain boundaries of the substrate and the film appears rough. The sapphire sample, on the other hand, present a crack-free surface without visible defects. The obtained Sn content is about 21.3 *at*% for the three samples and the critical temperature about 11 K for the sapphire and copper sample, even though the latter presents a wide transition: $\Delta T_c = 2\ K$. The quartz sample did not show a significant transition, hence it was not possible to measure the T_c .

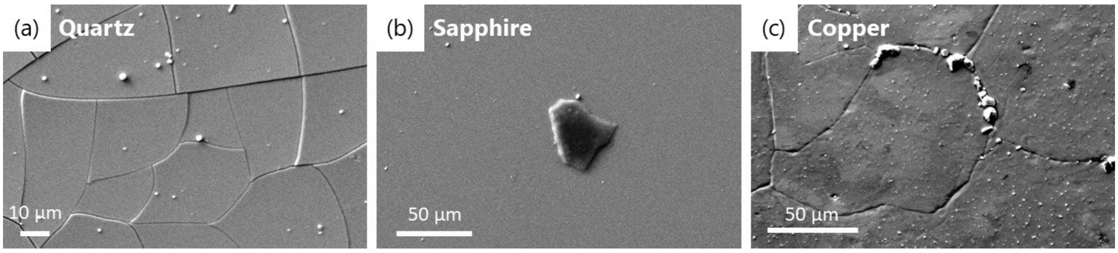

Figure 6.17: *SEM micrograph of the first deposition at 730°C of Nb_3Sn on: (a) quartz (b) sapphire and (c) copper. On quartz the film is extremely delaminated due to the $\alpha-\beta$ transition, on sapphire the film is smooth and defect-free and on copper Cu inclusions between the grain boundaries of the surface are visible.*

6.2.2 Annealing effect

To improve the surface quality, an annealing step performed *in-situ* - without venting the chamber - has been introduced together with a slow, controlled cool-down. The temperature gradient used was *30°C/h.* The test was performed with the same parameters as the first test, with a 24 hours annealing at 750°C. On copper, the grain boundaries of the substrate are still visible but there are not inclusions between them. In figure 6.18(a) the critical temperature is reported in function of the composition for the two tests. The annealing resulted in a slightly improved composition. Also, the T_c has improved and on sapphire it reached about 16 K, which is higher than the predicted value at that composition - note that the trend Tc vs %Sn is calculated empirically from bulk Nb_3Sn samples - but in line with other results obtained on sapphire in literature [46]. The values obtained are in line with the trend predicted from literature [33]. From the XRD diffractograms of the sapphire samples, reported in figure 6.18(b), it can be seen that the only phase present is the desired A15: no other Nb-Sn phases are visible.

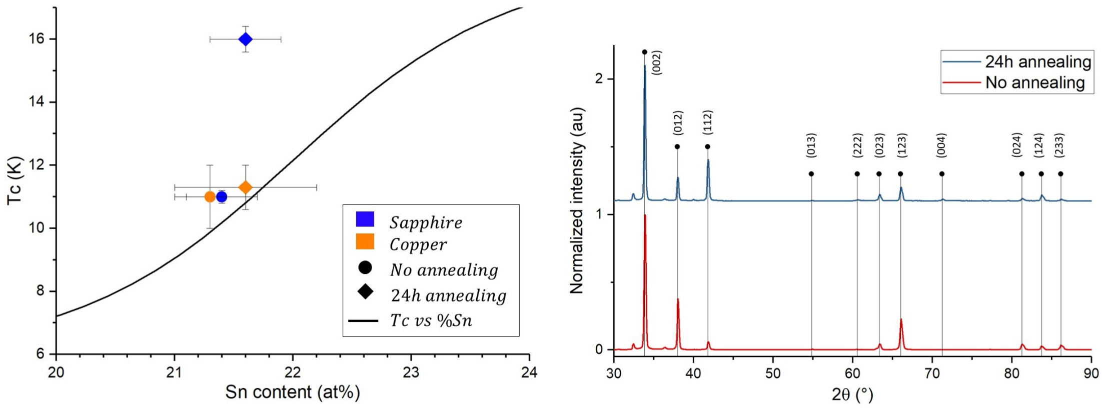

(a) T_c vs %Sn

(b) XRD on sapphire

Figure 6.18: *Results for the tests with and without annealing. (a)* T_c *versus Sn content and (b) XRD diffractograms for the samples deposited on sapphire. The black line in (a) is adapted from* [33]. *Both* T_c *and composition are increased with a 24 hours annealing, the only phase visible is that of* Nb_3Sn *.*

6.2.3 Copper interdiffusion and annealing time

The high deposition temperatures and the prolonged heat treatments cause copper diffusion in the superconducting film. The same approach used for the NbTi coatings - a niobium diffusion barrier - have been implemented. The Nb interlayers of thickness 0.5 and 1.0 μm are deposited as previously described. In figure 6.19 the copper profiles are reported for the films deposited at 730°C and annealed for 0 (no annealing), 24 and 48h. The annealed samples comprehends also the Nb/Cu interlayers. The comparison between the 24 h annealed and not annealed Cu substrate indicate that the former has a lower Cu content, this is probably an effect of the better surface quality obtained during the annealing. The 48 h annealing does not have a significant impact close to the surface - down to 1.0 μm in depth - but, as expected, there is a greater Cu content near the substrate. For both the annealing times, the Nb interlayer reduces the profiles according to its thickness. Moreover, the 1.0 μm thick Nb diffusion barrier seems to produce the best results: no Cu signal is detected from the EDS down to 1.0 μm in depth.

In figure 6.20 the XRD diffractogram for the samples annealed at 24 and 48 hours at 750°C are reported. They show that the A15 phase is obtained in every sample and the other peaks present are either those of copper or those of niobium. The latter are only present in the sample with the 1.0 μm Nb interlayer, mainly on the 24 h annealed - labelled as black diamonds. The one at 38° is partially overlapped with the Nb$_3$Sn (012) reflex, and the one at high angle, 82°, could be a reflection of Nb$_6$Sn$_5$, but since it would be of extremely low intensity and no other - more relevant - peaks associated to this phase are present, it is likely attributed to Nb. At 55° is visible another reflection that is associated either to Nb or to the (013) of Nb$_3$Sn . These peaks are coming either from unreacted Nb regions or, more likely, from the interlayer. Overall, the copper reflections are small intensity except from one anomalous reflection in the $Nb(0.5\ \mu m)/Cu$ 24 h, at 43°. The different annealing time seems to not influence the crystallite size which is about 70 nm. Although the value is in line with other results in literature [46], this result requires more investigation.

In figure 6.21(a) the critical temperature is plotted versus the composition for the

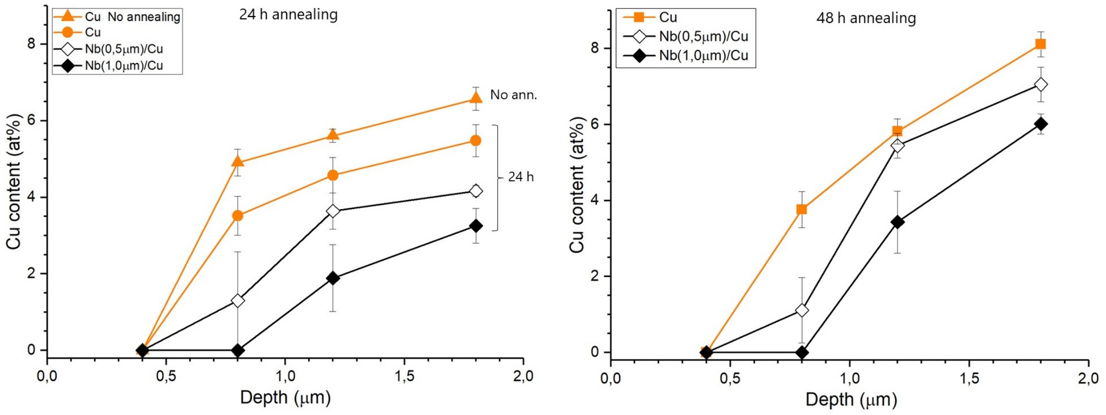

(a) 24 hour annealing **(b)** 48 hours annealing

Figure 6.19: *Copper diffusion profiles at different annealing duration for the copper substrates and the Nb interlayers. The annealing temperature is 750°C and the film thickness is about* 1.5 *μm.*

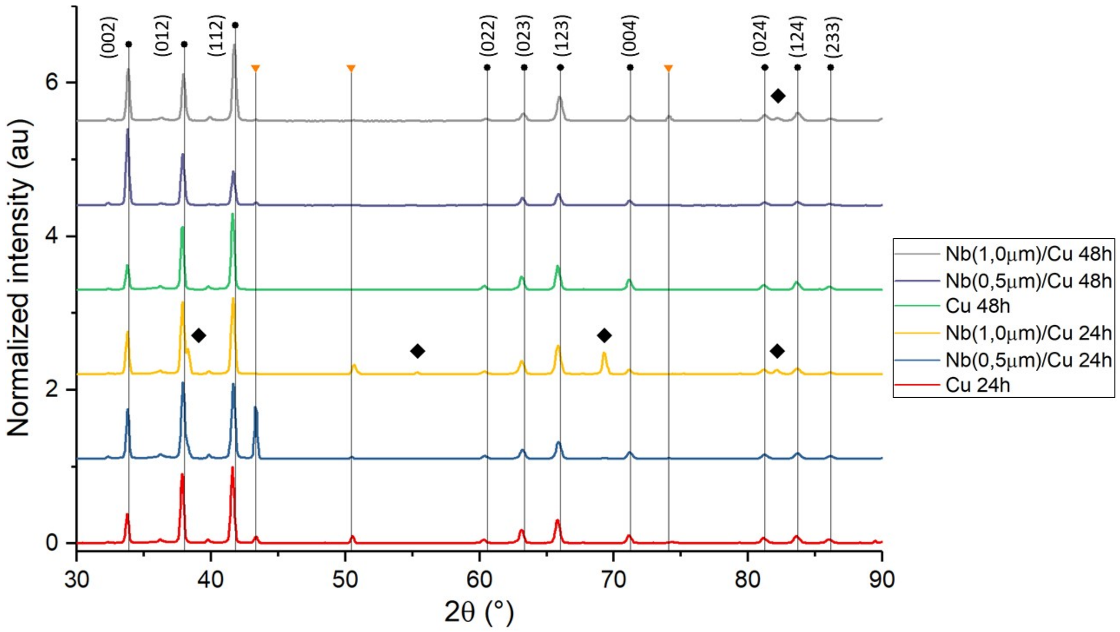

Figure 6.20: *XRD diffractogram for the samples annealed at 24 and 48 hours at 750°C. The black dots are the reflections of Nb$_3$Sn , the orange triangles those of copper and the black diamonds are of niobium.*

samples annealed for 24 and 48 hours. The samples annealed for 24 hours present a T_c higher than the ones annealed for 48 hours. Also, for the 24 hours samples, it is possible to see that an increasing thickness of the Nb diffusion barrier enhances the T_c . The composition of these samples is consistent around 21.5 $at\%$ of Sn. On the other hand, an annealing of twice the time does not seems to make any improvement: the composition is not consistent and the T_c is slightly lower; only the $Nb(1.0\ \mu m)/Cu$ has a comparable T_c to the 24 hours ones, but still lower than its twin annealed for 24 hours. From the SEM micrographs reported in figure 6.21(b) and (c), it can be seen that the effect of the 48 hours annealing does not sensibly improve the surface quality.

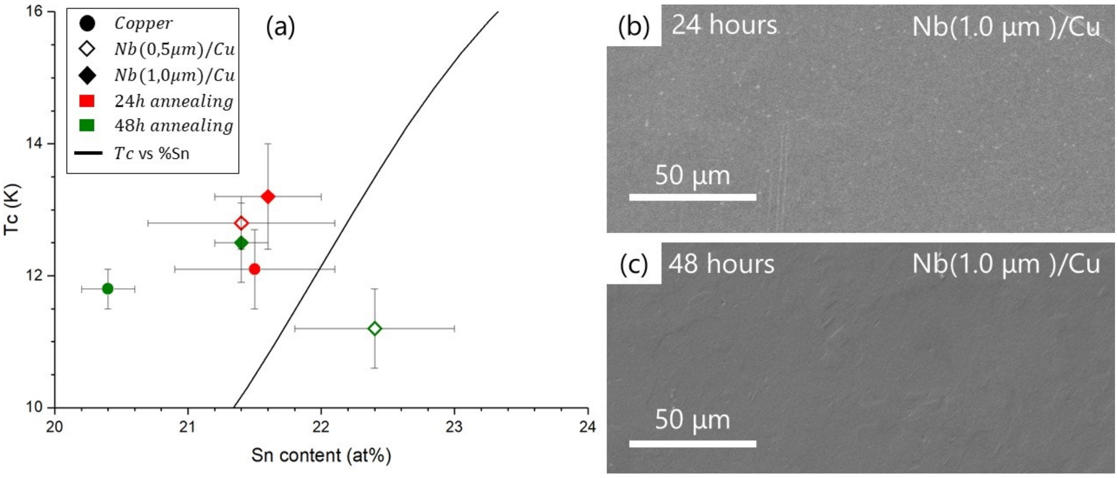

Figure 6.21: *(a) critical temperature versus composition for the samples deposited on Cu and the two Nb/Cu interlayers for 24 and 48 hours and annealed at 750°C. The black line in (a) is adapted from* [33]. *On the right, SEM micrographs of the* $Nb(1.0\ \mu m)/Cu$ for (b) 24 hours and (c) 48 hours of annealing.

Overall, the results obtained with an annealing of 24 hours are promising but a longer time does not have a beneficial impact. Shorter annealing duration will also be investigated.

6.2.4 Coating and annealing temperature effect

The coating and annealing temperatures investigated are 550°C, 600°C, 650°C and 750°C. In figure 6.22 the critical temperature and the composition are reported in function of the annealing temperature. Overall, the T_c increases with the temperature for every substrate, the $Nb(1.0\ \mu m)/Cu$ substrate yields the higher values. Only the T_c of the $Nb(0.5\ \mu m)/Cu$ sample, annealed at 550°C, had been measured, though extremely low: for the other samples, the signal detected did not present any significant transition. It is important to underline that for applications in resonant cavities a lower deposition temperature is preferable, high temperatures could compromise the structural integrity of the copper cavity and later on its RF performance (ie: resonant frequency). So this result suggest that it could be possible to obtain a rather high T_c at lower temperatures implementing a $1 \mu m$ thick niobium layer instead of coating directly on copper. From the graph, it is possible to see that the T_c obtained with the $1 \mu m$ Nb interlayer at 600°C is comparable to the T_c for the copper sample coated at 750°C.

The composition follows the opposite trend: higher temperatures results in a lower Sn content. This is explained in terms of Sn evaporation during the annealing, as reported in [46].

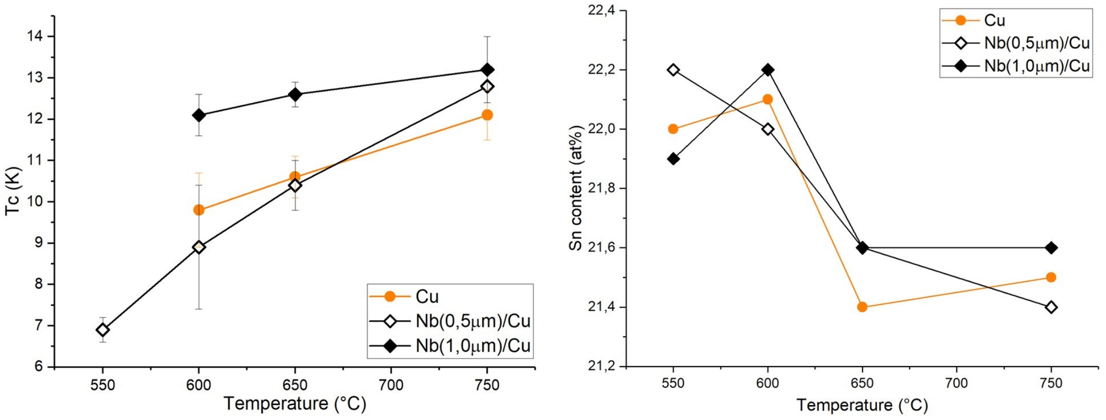

(a) (b)

Figure 6.22: *Critical temperature (a) and Sn content (b) in function of the annealing temperature. The T_c on the $Nb(1.0\ \mu m)/Cu$ interlayer is higher than in other substrates and the temperature dependence weker.*

In figure 6.23 the XRD diffractograms of the $Nb(1.0\ \mu m)/Cu$ samples annealed at different temperatures are reported. The the peaks present are exclusively those of Nb$_3$Sn , except for the Nb reflections present in the 750°C sample as previously discussed. The peak at 50° is labelled is considered as a Cu reflection, it could be associated to a Nb$_6$Sn$_5$ peak but it is unlikely since its relative intensity should be much lower, moreover, no other more relevant Nb$_6$Sn$_5$ reflections are present. The crystallite size is about 100 nm but do not seem influenced by the annealing temperature.

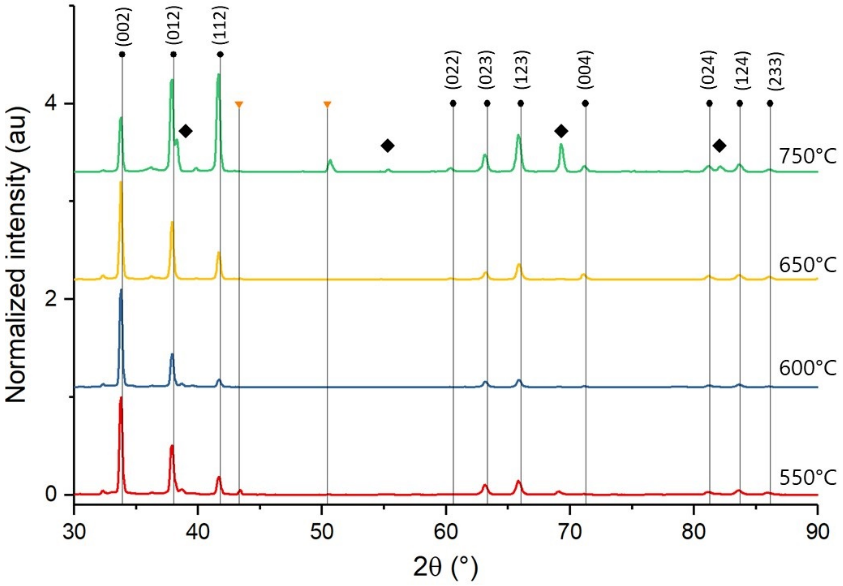

Figure 6.23: *XRD diffractograms of the* $Nb(1.0\ \mu m)/Cu$ *samples annealed at different temperatures. The black dots are the* Nb_3Sn *reflections and the diamonds are Nb reflections coming from either unreacted Nb in the film or, more likely, from the Nb interlayer.*

6.2.5 Pressure effect

Three deposition pressures have been tested: 3×10^{-3}, 7×10^{-3} and 2×10^{-2} $mbar$; a lower pressure is desired to obtain a better surface quality but a higher pressure allows to get a higher Sn content. The results reported are of samples annealed at 650°C for 24 hours.

In figure 6.24 the critical temperature and Sn content are plotted in function of the deposition argon pressure. The T_c of the copper and $Nb(1.0\ \mu m)/Cu$ samples improves at higher pressure; the latter represent the highest critical temperature obtained in this work in a metallic substrate: $T_c = 13.8\ K$ albeit with a rather wide transition: $\Delta T_c = 1.4\ K$. The composition of the $Nb(1.0\ \mu m)/Cu$ sample increases as the pressure increases, but this trend is not observed in the other samples.

In figure 6.25 the SEM micrographs of the samples $Nb(1.0\ \mu m)/Cu$ coated at different pressures are reported. The beneficial effect of a lower pressure is not evident, because they present superficial defects that are partially due to the substrate roughness, like the holes in (c), and structures with a different composition compared to the defect free zones of the film, like those visible in (a) and (b).

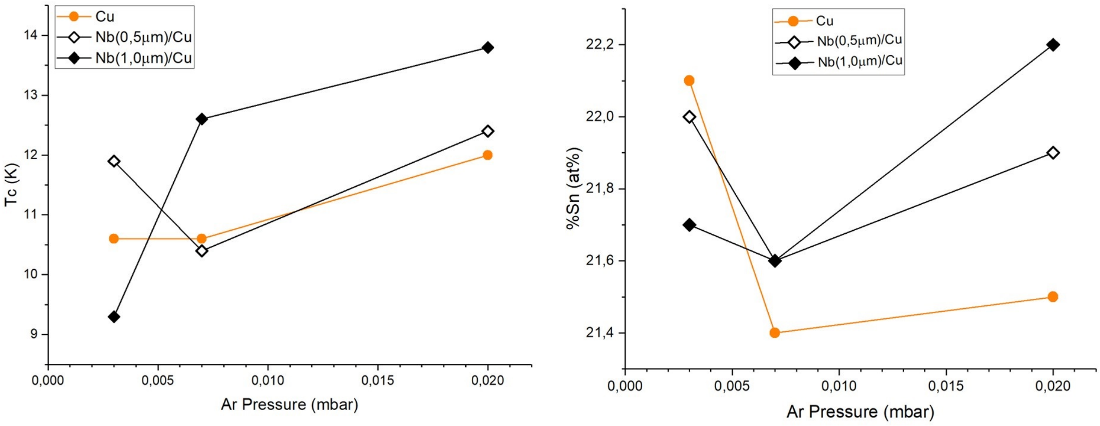

(a) **(b)**

Figure 6.24: *Critical temperature (a) and Sn content (b) in function of the deposition argon pressure for the samples annealed at 650°C for 24 hours. The* T_c *seems to improve at higher deposition pressure, but the Sn content does not follow this trend.*

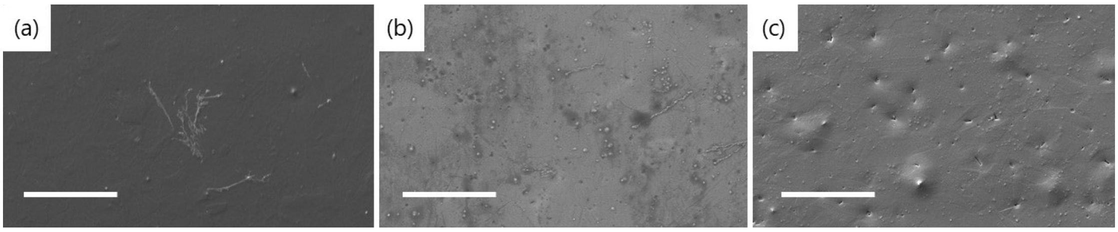

Figure 6.25: *Sem micrographs of the* $Nb(1.0\ \mu m)/Cu$ *annealed at 650°C for 24 hours for different argon pressures: (a)* $3{\times}10^{-3}$ *mbar, (b)* $7{\times}10^{-3}$ *mabr and (c)* $2{\times}10^{-2}$ *mbar. The scale bar is* $50\mu m$.

6.2.6 RBS and PIXE analysis

In figure 6.26 are reported the spectra for the RBS and PIXE analysis performed at HZDR on Nb$_3$Sn samples coated on Cu and the two Nb interlayers at 730°C $P_{Ar} = 7 \times 10-3$ $mbar$ and annealed for 24 hours at 750°C. From the RBS spectra the copper signal is not visible. As discussed for NbTi - paragraph 6.1.2, if a copper concentration is present in the top 500 - 1000 nm of the sample, a step at 750 keV should be visible. Recalling equation (6.1), the atomic composition estimated from the peaks intensity ratio is 24 % of Sn, which is in line with the EDS measurements of 22 at%.

From the PIXE spectra it is possible to see a higher Cu signal for the film deposited directly on copper, instead, for the Nb interlayers the signal is almost one order of magnitude weaker. Like for the NbTi analysis, this Cu signal can be associated to the substrate's excitement due to the low film thickness, and the signal at 5 keV is not a contaminant but an artifact caused by the pile-up of the Nb and Sn lines.

Also in the case of Nb$_3$Sn , no copper is visible in the film's surface.

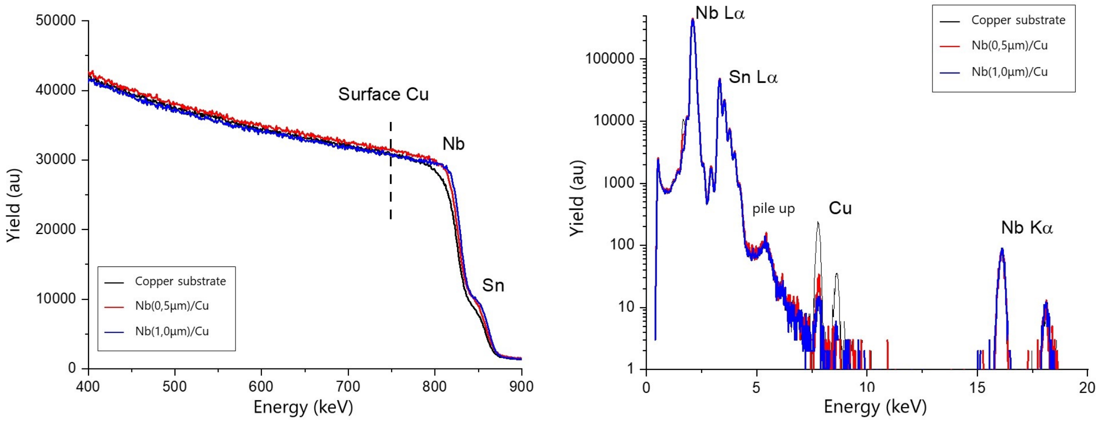

(a) RBS **(b)** PIXE

Figure 6.26: *RBS (a) and PIXE (b) spectra of the Nb$_3$Sn samples deposited on copper and the two niobium interlayers. Courtesy of Dr. Zhou Shengqiang.*

6.2.7 Summary

The most promising results have been obtained for samples deposited at 2×10^{-2} $mbar$ at 650°C and annealed for 24 hours at the same temperature. In figure 6.27, the critical temperature of these samples is reported in function of the composition. It can be seen that a higher thickness of the Nb interlayer improves both T_c and composition. This last effect is caused by blocking Sn diffusion towards the substrate.

Overall, it can be seen in figure 6.28 that the composition of the films ranges between 20 and 22 at% of Sn. The critical temperature measured on copper is about 11 K and improves by adopting a 1.0 μm thick niobium interlayer, reaching 14 K for the film deposited at 2×10^{-2} $mbar$. A lower deposition temperature - such as 3×10^{-3} $mbar$ - results in an inconsistent composition. The Nb interlayer, also eliminates the Cu diffusion issue, by making it invisible from the EDS down to 1.0 μm from the surface of the Nb$_3$Sn film. However, RBS and PIXE analyses did not confirm the presence of Cu in the film. An investigation on the cross-sections of the samples, obtained with the FIB technique, is in program at HZB.

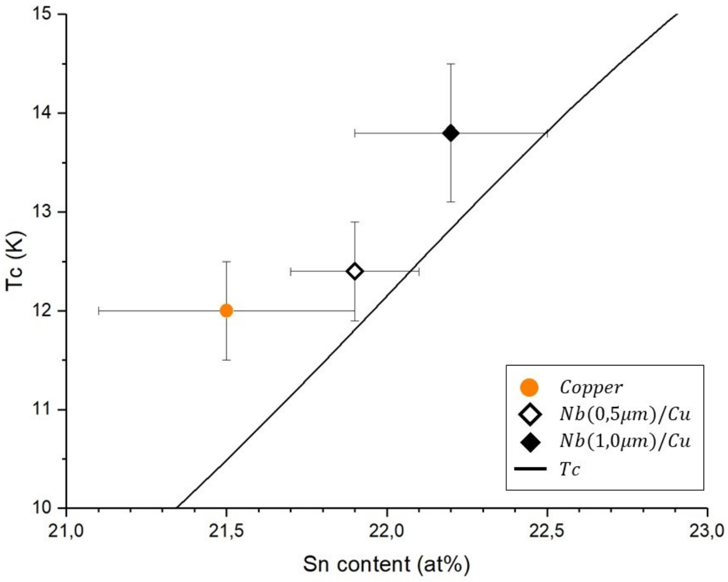

Figure 6.27: *Critical temperature versus composition of the samples coated at* 2×10^{-2} *mbar at 650°C and annealed for 24 hours. The black line in (a) is adapted from* [33]. *It is clear that a Nb interlayer increases both* T_c *and Sn content in the film.*

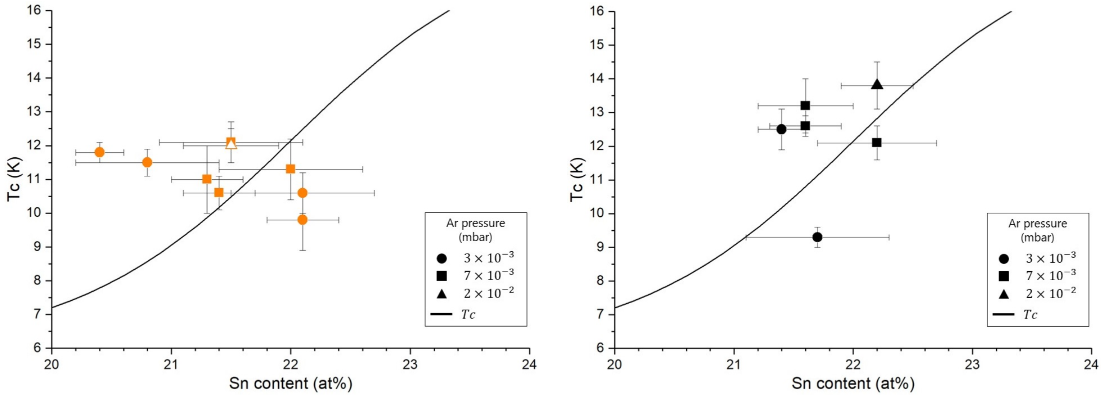

(a) **(b)**

Figure 6.28: *Critical temperature versus composition of the samples deposited on (a) copper and (b)* $Nb(1.0\ \mu m)/Cu$. *With the Nb interlayer, higher* T_c *and higher Sn content are achieveed.*

6.3 Critical temperature measurements

As described in section 5.5.4, the critical temperature measurements consist on the simultaneous acquisition of the temperature and the signal coming from the pickup coil. On dielectric substrates the SC transitions generate a more intense signal compared to the samples on metallic substrates, due to appearance of eddy currents in the latter, figure 6.29(a) and (b). Moreover, the width of the transition is generally narrower. Having a weak signal means that the discrimination of possible multiple transition in the sample, due to different SC phases, is problematic. As an example, in figure 6.29(c) and (d) are reported the T_c curves acquired for the Nb interlayer (1.0 μm) and for the NbTi deposited on an analogous Nb/Cu sample at 500°C. In the latter, a slight change in the signal is present in the transition part of curve (at 9.4 K), but it is probably an artifact and it would still give a higher T_c than expected; hence it is considered as one single transition.

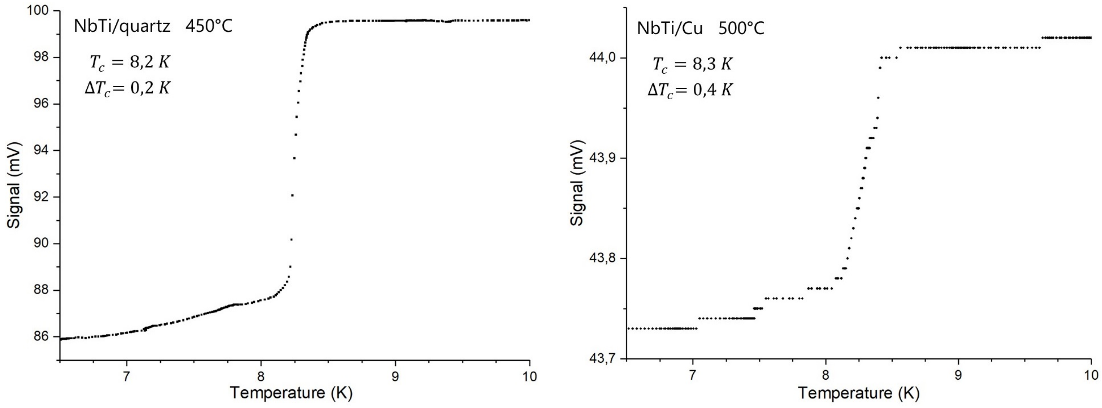

(a) NbTi/Qaurtz **(b)** NbTi/Cu

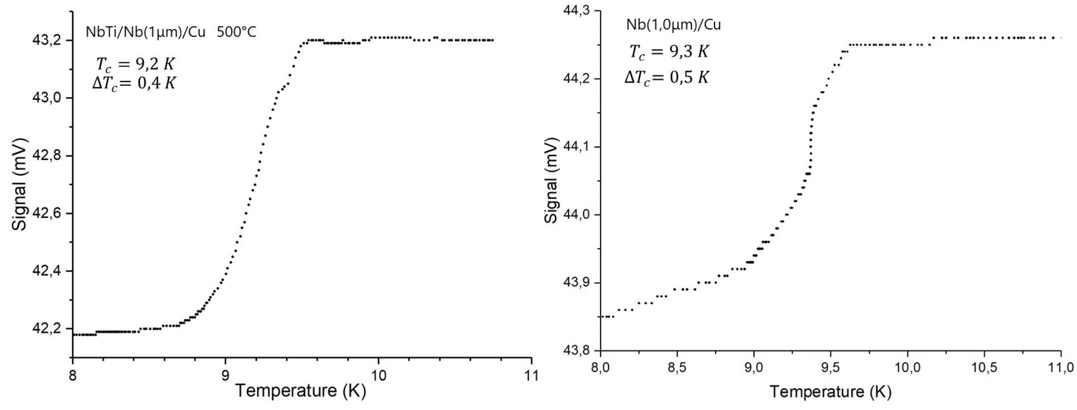

(c) NbTi/Nb(1.0 μm)/Cu @ 500°C **(d)** Nb(1.0 μm)/Cu

Figure 6.29: *T_c curves for NbTi on different substrates (a) quartz, (b) copper (c) NbTi deposited on Nb(*1.0 μm*)/Cu at 500°C. (d) T_c of only the Nb interlayer of* 1.0 μm*. On dielectric substrates the transition is more*

A double SC transition has been observed in a Nb_3Sn sample, figure 6.30, where the critical temperature measurement for the sample coated on $Nb(1.0\ \mu m)/Cu$ and annealed at 650°C for 24 hours is reported. It shows a double transition, one at 12.6 K and another at 9.8 K. The first is associated to Nb_3Sn , while the other could be the

T_c of the niobium interlayer or that of a Nb3Sn phase with a different composition. On the right the collected signal versus the *time-stamp* - time reference - is reported to highlight the onset of the transition at higher temperature. It is not very visible when the signal is plotted versus the temperature because the latter is varied manually during the acquisition, hence, the combination of the two data-sets can alter the transition profile.

Also for Nb3Sn , the transition on dielectric are of grater magnitude, whereas on metallic substrate the signal is weaker.

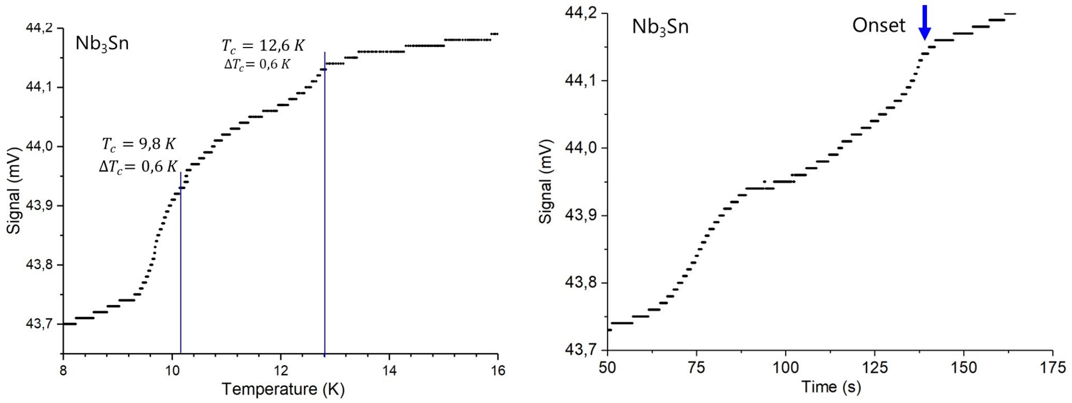

(a) $Nb(1.0\ \mu m)/Cu$ **(b)** $Nb(1.0\ \mu m)/Cu$

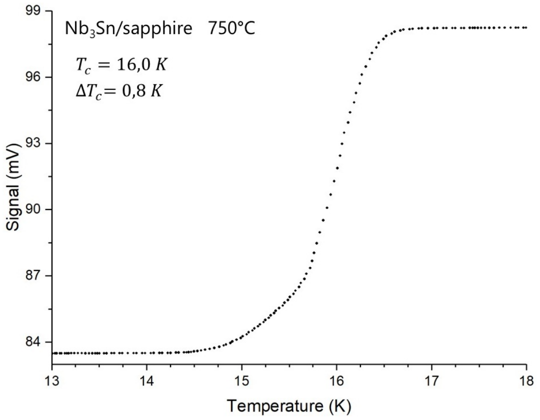

(c) Sapphire

Figure 6.30: *Critical temperature measurements of* Nb_3Sn *samples. (a) coated on* $Nb(1.0\ \mu m)/Cu$ *and annealed at 650°C for 24 h, (b) signal versus time reference of the same sample. It shows a double transition probably due to the presence of two SC phases at different composition. (c)* Nb_3Sn *coated on sapphire and annealed at 750°C for 24 h.*

7

Conclusions

In this work, superconducting coatings of NbTi and Nb_3Sn have been developed by DC magnetron sputtering for SRF cavities for the axion detection. The UHV systems for the coatings have been upgraded: the system for NbTi - and Nb - has been equipped with a new 4-inch DC magnetron sputtering source, and the system dedicated to Nb_3Sn has been set up to operate at high temperature. The substrates used are quartz, sapphire, OHFC copper and Nb coated on copper (Nb/Cu).

For both materials, the films presented copper contamination due to the interdiffusion of the Cu substrate caused by the high deposition temperature. To eliminate this problem, a Nb diffusion barrier layer, of two different thicknesses: 0.5 μm and 1.0 μm, has been adopted. The films grown onto the 1.0 μm Nb layer demonstrated to be effective in avoiding the Cu diffusion near the surface. Rutherford Backscattering Spectrometry and Particle Induced X-ray Emission spectroscopy, courtesy of Dr. Zhou Shengqiang (HZDR), did not confirm the presence of Cu in the film's surface. RBS analyses on the samples, both NbTi and Nb_3Sn , coated on copper and the Nb interlayer showed a composition in line with the EDS measurements.

Overall the best results are obtained with a Nb layer thickness of 1.0 μm. The critical temperature of the interlayer (about 9.3 K) has not been observed in any sample. One Nb_3Sn sample presents a double SC transition, but it could be associated to a phase with different stoichiometry. This suggests that more a deeper investigation on the film-interlayer-substrate interactions is needed. For this reason, analyses on the FIB machined cross-section of the samples is in program as part of a collaboration with HZDR.

NbTi

Part of this work consisted in the deposition of NbTi films onto copper haloscopes. Several tests have been performed on planar samples to optimize the deposition process. The composition of the copper samples is in the desired range for having a maximum upper critical field, around 50 wt% of Ti. The critical temperatures measured with an inductive systems are in line with the predicted values in literature. XRD and third harmonic AC magnetic susceptibility analysis, performed at LNF, show that only a single SC phase is present. The samples coated on the Nb interlayers present a T_c that could be associated to Nb rather than NbTi: due to the weakness of the SC transition signal on metallic substrates the NbTi transition could be masked by that of Nb.

In total, four copper cavities - eight half cells - of resonating frequency 9 and 7GHz have been coated with 2.5 μm of NbTi and delivered to testing their performance in cryogenic environment at high magnetic field. Moreover, one 9GHz haloscope has been coated with a 1.0 μm Nb diffusion barrier, prior to the NbTi deposition.

The 7GHz haloscope presents the best performance of the ones already tested. At 4.2 K and at 8 T the figure of merit relevant to the axion search - the product B^2Q_0 - results 1×10^7 T^2: one order of magnitude higher than a copper cavity. Moreover, the quality factor, measured at 4.2 K and at zero field (3×10^6) has reached the limitations imposed by the by conical parts of the haloscope that are not coated with the SC film. The 9GHz haloscope, instead, have worse performance than an analogous cavity coated in 2019 [9]. Nonetheless, the difference is minimal: both present quality factors in the same order of magnitude and still higher than a copper cavity.

These promising results demonstrate that with the upgraded NbTi coating system it is possible to obtain and reproduce high performance haloscopes.

The future developments of NbTi consists on the tests of the remaining haloscopes, including the one with the Nb interlayer, which has been already sent to LNF, and in more RF characterization in high field. Moreover, the composition of the film could be improved by changing the deposition parameters, argon pressure and magnetron current, to further enhance the upper critical field B_{c2}.

Nb_3Sn

In this work, the production of Nb_3Sn films via DCMS from a stoichiometric target has been investigated. The parameters varied are the coating and annealing temperature, the annealing duration and the deposition pressure.

The films coated on sapphire presented a good quality but were not available for most of the processes. The highest T_c obtained on sapphire is 16 K, in line with other results in literature [46]. The coatings on quartz did not present superconductive behavior due to delamination of the film caused by the $\alpha \longrightarrow \beta$ transition of quartz. On copper substrates, the films resembled the substrate roughness and Cu interdiffusion has been observed with EDS and mitigated with a niobium diffusion barrier - as was done for NbTi. The

A 24 hours annealing of the samples, performed right after the deposition in ultra high vacuum environment, demonstrated to have a key effect on the superconductive properties enhancing the T_c . A prolonged annealing of 48 hours does not seem to have an impact, instead those samples presented a non consistent composition and lower critical temperature than the 24 hours annealing. Thus, the 24 hours annealing seems to be the best strategy.

A higher deposition pressure results in a higher T_c , but more investigation regarding its effect on the composition is needed.

Higher annealing temperatures enhances the T_c on metallic substrates but at the same time produce lower Sn content. An interesting effect arises from the different substrates. The 1.0 μm Nb diffusion barrier weakens the T_c versus annealing temperature dependence: the T_c obtained on such substrate at 600°C is comparable, or even higher, to that obtained directly on copper at 750°C. This is of extreme importance for copper resonant cavities because they cannot tolerate high temperature treatments otherwise the

RF properties would deteriorate. This strategy could be transferred to both haloscopes - objective of this thesis - and accelerating cavities. Moreover, it blocks the tin diffusion towards the substrate increasing the Sn content in the film.

Overall, the composition obtained in this work is around 22 at% of Sn. To achieve better performances, ie: higher critical temperature and critical magnetic field, the composition needs to be optimized. To overcome this problematic, different routes could be explored. A shorter annealing time, less than 24 hours, could result in less Sn depletion. Also, a target more rich in tin could be employed. In the future the possibility of deposition with a pulsed DC power supply will be investigated. This technique allows to use higher deposition peak power but a lower mean power, with the additional benefit of having a better cooling of the target. Other future developments for Nb_3Sn comprehends the optimization of the deposition parameters, RF measurements in high magnetic field on planar samples and the deposition on haloscopes.

Acknowledgements

This work would not have been possible without the constant support of my family who I deeply thank for everything they have done for me. I would like to thank my two close friends Massimo and Martina with whom I shared these wonderful years.

I wish to thank everyone in the Surface Technologies and Superconductivity Laboratories, especially the best lab partner I could have asked for, Dr. Vanessa Garcia, and my supervisor Prof. Cristian Pira who have patiently helped me and taught me throughout the thesis period. I am mostly grateful to Dr. Dorothea Fonnesu for the discussions about the critical temperature measurements, and to Dr. Zhou Shengqiang for the discussion on the RBS and PIXE analyses.

Bibliography

(1) R. D. Peccei and H. R. Quinn, *Phys. Rev. Lett.*, 1977, **38**, 1440–1443.

(2) *ADMX Collaboration*, `https://depts.washington.edu/admx/` (visited on 06/10/2022).

(3) *QUAX Experiment*, `https://www.pd.infn.it/eng/quax/` (visited on 06/10/2022).

(4) *CERN accelerators*, `https://home.cern/science/accelerators` (visited on 06/10/2022).

(5) *ITER magnets*, `https://www.iter.org/mach/Magnets` (visited on 06/10/2022).

(6) *Superconducting Quantum Materials and Systems Center*, `https://sqms.fnal.gov/` (visited on 06/10/2022).

(7) *ASG Superconductors Paramed MRI*, `https://www.asgsuperconductors.com/paramed-mri` (visited on 06/10/2022).

(8) *SCMAGLEV*, `https://scmaglev.jr-central-global.com/` (visited on 06/10/2022).

(9) D. Alesini, C. Braggio, G. Carugno, N. Crescini, D. D'Agostino, D. Di Gioacchino, R. Di Vora, P. Falferi, S. Gallo, U. Gambardella, C. Gatti, G. Iannone, G. Lamanna, C. Ligi, A. Lombardi, R. Mezzena, A. Ortolan, R. Pengo, N. Pompeo, A. Rettaroli, G. Ruoso, E. Silva, C. C. Speake, L. Taffarello and S. Tocci, *Phys. Rev. D*, 2019, **99**, 101101.

(10) *I.FAST WP9*, `https://ifast-project.eu/wp9-innovative-superconducting-thin-film-coated-cavities` (visited on 08/23/2022).

(11) A. Sudbø and K. Fossheim, *Superconductivity: Physics and Applications*, John Wiley & Sons, Ltd, 2004.

(12) P. Seidel, *Applied Superconductivity: Handbook on Devices and Applications*, Wiley-VCH, 2015.

(13) R. Kleiner and W. Buckel, *Superconductivity: Fundamentals and Applications*, Wiley-VCH, 2nd edn., 2004.

(14) C. H. Lees, *Nature*, 1919, **104**, 247.

(15) W. Meissner and R. Ochsenfeld, *Naturwissenschaften*, 1933, **21**, 787–788.

(16) Z.-A. Ren, J. Kato, T. Muranaka, J. Akimitsu, M. Kriener and Y. Maeno, *Journal of the Physical Society of Japan*, 2007, **76**, 103710.

(17) U. Gottlieb, J. C. Lasjaunias, J. L. Tholence, O. Laborde, O. Thomas and R. Madar, *Phys. Rev. B*, 1992, **45**, 4803–4806.

(18) F. London and H. London, *Proc. R. Soc. Lond. A*, 1935, **149**, 71–88.

(19) CAS - CERN Accelerator School : Superconductivity and Cryogenics for Accelerators and Detectors: Erice, Italy 8 - 17 May 2002. CAS - CERN Accelerator School on Superconductivity and Cryogenics for Accelerators and Detectors, CERN, CERN, Geneva, 2004.

(20) H. Padamsee, J. Knobloch and T. Hays, *RF Superconductivity for Accelerators*, Wiley-VCH, 2nd edn., 2008.

(21) N. Pompeo and E. Silva, *Phys. Rev. B*, 2008, **78**, 094503.

(22) E. Silva, K. Torokhtii and N. Pompeo, 2015 IEEE International Instrumentation and Measurement Technology Conference (I2MTC) Proceedings, 2015, pp. 560–565.

(23) S. Calatroni, *Physica C: Superconductivity*, 2006, **441**, 95–101.

(24) V. Palmieri, G. Caldarola, S. Cisternino, C. Pira, H. Skliarova, F. Stivanello and D. Franco-Lespinasse, 2017.

(25) A.-M. Valente-Feliciano, *Superconductor Science and Technology*, 2016, **29**, 113002.

(26) Z. Charifoulline, *IEEE Transactions on Applied Superconductivity*, 2006, **16**, 1188–1191.

(27) F. Liu, H. Liu, Y. Wu, X. Zhang, H. Ma and J. Qin, *IEEE Transactions on Applied Superconductivity*, 2020, **30**, 1–4.

(28) M. Parizh, Y. Lvovsky and M. Sumption, *Superconductor Science and Technology*, 2016, **30**, 014007.

(29) C. Meingast, P. J. Lee and D. C. Larbalestier, *Journal of Applied Physics*, 1989, **66**, 5962–5970.

(30) D. Patel, S.-H. Kim, W. Qiu, M. Maeda, A. Matsumoto, G. Nishijima, H. Kumakura, S. Choi and J. H. Kim, *Scientific Reports*, 2019, **9**, 14287.

(31) L. R. Testardi, *Rev. Mod. Phys.*, 1975, **47**, 637–648.

(32) C. J.P., M. I and M. P.E., *Journal of Materials Science*, 1970, **5**, 580–603.

(33) A. Godeke, *Superconductor Science and Technology*, 2006, **19**, R68–R80.

(34) D. H., J. J., D. M., M. J. and F. René, *Journal of Materials Science*, 1981, **16**, 2145–2153.

(35) E. Barzi and A. V. Zlobin, in *Nb3Sn Accelerator Magnets: Designs, Technologies and Performance*, ed. D. Schoerling and A. V. Zlobin, Springer International Publishing, Cham, 2019, pp. 23–51.

(36) M. Peiniger, M. Hein, N. Klein, G. Muller, H. Piel and P. Thüns, Proceedings of The Third Workshop on RF Superconductivity, 1987.

(37) U. Pudasaini, G. V. Eremeev, J. W. Angle, J. Tuggle, C. E. Reece and M. J. Kelley, *Journal of Vacuum Science & Technology A*, 2019, **37**, 051509.

(38) R. D. Porter, H. Hu, M. U. Liepe, J. Tao, N. Stilin and Z. Sun, North American Particle Acc. Conf, 2019.

(39) S. Posen et al., Proc. SRF'19, Dresden, Germany, JACoW Publishing, Geneva, Switzerland, 2019, pp. 818–822.

(40) S. M. Deambrosis, Ph.D. Thesis, Università degli Studi di Padova, 2008.

(41) M. Zanierato, Master's Degree Thesis, Università degli Studi di Padova, 2020.

(42) M. Zanierato, Master Thesis in "Surface Treatments for Industrial Applications", Università degli Studi di Padova, 2021.

(43) M. N. Sayeed, G. Eremeev, U. Pudasaini, M. Burton, C. Reece, A.-M. Valente-Feliciano and H. Elsayed-Ali, International Conference on RF Superconductivity, 2019.

(44) C. T. Wu, R. T. Kampwirth and J. W. Hafstrom, *Journal of Vacuum Science and Technology*, 1977, **14**, 134–137.

(45) PVD Depostion of Nb3Sn Thin Film on Copper Substrate from an Alloy Nb3Sn Target, JACoW Publishing, Geneva, Switzerland, 2019, pp. 2818–2822.

(46) E. A. Ilyina, G. Rosaz, J. B. Descarrega, W. Vollenberg, A. J. G. Lunt, F. Leaux, S. Calatroni, W. Venturini-Delsolaro and M. Taborelli, *Superconductor Science and Technology*, 2019, **32**, 035002.

(47) F. Chadha-Day, J. Ellis and D. J. E. Marsh, *Science advances.*, 2022, **8**.

(48) P. W. Graham, I. G. Irastorza, S. K. Lamoreaux, A. Lindner and K. A. van Bibber, *Annual Review of Nuclear and Particle Science*, 2015, **65**, 485–514.

(49) H. Yukawa, *Nippon Sugaku-Buturigakkwai Kizi Dai 3 Ki*, 1935, **17**, 48–57.

(50) M. Kawasaki and K. Nakayama, *Annual Review of Nuclear and Particle Science*, 2013, **63**, 69–95.

(51) D. Griffith, *Introduction to Elementary Particles*, Wiley-VCH, 2nd edn., 2008.

(52) C. S. Wu, E. Ambler, R. W. Hayward, D. D. Hoppes and R. P. Hudson, *Phys. Rev.*, 1957, **105**, 1413–1415.

(53) J. H. Christenson, J. W. Cronin, V. L. Fitch and R. Turlay, 1964, **13**, 138–140.

(54) S. Weinberg, *Phys. Rev. Lett.*, 1978, **40**, 223–226.

(55) F. Wilczek, *Phys. Rev. Lett.*, 1978, **40**, 279–282.

(56) P. Sikivie, *Phys. Rev. Lett.*, 1983, **51**, 1415–1417.

(57) S. J. Asztalos, G. Carosi, C. Hagmann, D. Kinion, K. van Bibber, M. Hotz, L. J. Rosenberg, G. Rybka, J. Hoskins, J. Hwang, P. Sikivie, D. B. Tanner, R. Bradley and J. Clarke, *Physical Review Letters*, 2010, **104**, DOI: `10.1103/physrevlett.104.041301`.

(58) J. Hoskins, J. Hwang, C. Martin, P. Sikivie, N. S. Sullivan, D. B. Tanner, M. Hotz, L. J. Rosenberg, G. Rybka, A. Wagner, S. J. Asztalos, G. Carosi, C. Hagmann, D. Kinion, K. van Bibber, R. Bradley and J. Clarke, *Phys. Rev. D*, 2011, **84**, 121302.

(59) D. Budker, P. W. Graham, M. Ledbetter, S. Rajendran and A. O. Sushkov, *Phys. Rev. X*, 2014, **4**, 021030.

(60) P. W. Graham and S. Rajendran, *Physical Review D*, 2013, **88**, DOI: `10.1103/physrevd.88.035023`.

(61) R. Barbieri, C. Braggio, G. Carugno, C. Gallo, A. Lombardi, A. Ortolan, R. Pengo, G. Ruoso and C. Speake, *Physics of the Dark Universe*, 2017, **15**, 135–141.

(62) D. Alesini, C. Braggio, G. Carugno, N. Crescini, D. D'Agostino, D. D. Gioacchino, R. D. Vora, P. Falferi, U. Gambardella, C. Gatti, G. Iannone, C. Ligi, A. Lombardi, G. Maccarrone, A. Ortolan, R. Pengo, A. Rettaroli, G. Ruoso, L. Taffarello and S. Tocci, *Physical Review D*, 2021, **103**, DOI: `10.1103/physrevd.103.102004`.

(63) J. Golm, S. Arguedas Cuendis, S. Calatroni, C. Cogollos, B. Döbrich, J. Gallego, J. García Barceló, X. Granados, J. Gutierrez, I. Irastorza, T. Koettig, N. Lamas, J. Liberadzka-Porret, C. Malbrunot, W. Millar, P. Navarro, C. Pereira Carlos, T. Puig, G. Rosaz, M. Siodlaczek, G. Telles and W. Wuensch, *IEEE Transactions on Applied Superconductivity*, 2022, **32**, 1–5.

(64) D. Ahn, O. Kwon, W. Chung, W. Jang, D. Lee, J. Lee, S. W. Youn, D. Youm and Y. K. Semertzidis, 2020, DOI: `10.48550/ARXIV.2002.08769`.

(65) CAST Collaboration, *Nature Physics*, 2017, **13**, 584–590.

(66) M. Betz, F. Caspers, M. Gasior, M. Thumm and S. W. Rieger, *Phys. Rev. D*, 2013, **88**, 075014.

(67) M. Ohring, *Materials Science of Thin Films*, Academic Press, 2nd edn., 2002.

(68) D. M. Mattox, *Handbook of Physical Vapor Deposition (PVD) Processing*, Elsevier, 2nd edn., 2010.

(69) D. Lundin and K. Sarakinos, *Journal of Materials Research*, 2012, **27**, 780–792.

(70) B. Matthew, P. Ari, R. Charles and V.-F. Anne-Marie, 19th International Conference on RF Superconductivity (SRF 2019), 2019.

(71) W. Gonzalez, Master in Surface Treatements for Industrial Applications, Università degli Studi di Padova, 2008.

(72) A. Rossi et al., 16th International Conference on RF Superconductivity, Paris, France, 2013.

(73) V. A. G. Diaz, Ph.D. Thesis, Università degli Studi di Ferrara, 2021.

(74) C. Pira, C. Antoine, E. Chyhyrynets, X. Jiang, A. Katasevs, J. Kaupužs et al., Proc. SRF'19, Dresden, Germany, JACoW Publishing, Geneva, Switzerland, 2019, pp. 935–940.

(75) G. Wu, M. Ge, P. Kneisel, K. Zhao, J. Ozelis, D. Sergatskov and C. Cooper, 4 pp. Applied Superconductivity Conference (ASC 2010), 2010.

(76) K. Saito, 11th International Conference on RF Superconductivity, Lübeck/Travemünder, Germany, 2003.

(77) V. Palmieri, 16th International Conference on RF Superconductivity, Paris, France, 2013.

(78) A. Awad Abouelata, N. Abdel Ghany and T. Dahy, *Applied Surface Science - APPL SURF SCI*, 2010, **256**, 4370–4375.

(79) J. I. Goldstein and H. Yakowitz, *Practical Scanning Electron Microscopy*, Springer New York, NY, 1st edn., 1975.

(80) C. Suryanarayana and M. G. Norton, *X-Ray Diffraction A Practical Approach*, Springer New York, NY, 1998.

(81) S. Stark, A. A. Rossi and V. Palmieri, *LNL Annual report*, 2012, 185.

(82) S. Murase, K. Itoh, H. Wada, K. Noto, Y. Kimura, Y. Tanaka and K. Osamura, *Physica C: Superconductivity*, 2001, **357-360**, 1197–1200.

(83) L. Feldman and J. Mayer, *Fundamentals of surface and thin film analysis*, 1987, vol. 26, pp. 620–620.

(84) D. Di Gioacchino, C. Gatti, D. Alesini, C. Ligi, S. Tocci, A. Rettaroli, G. Carugno, N. Crescini, G. Ruoso, C. Braggio, P. Falferi, C. S. Gallo, U. Gambardella, G. Iannone, G. Lamanna, A. Lombardi, R. Mezzena, A. Ortolan, R. Pengo, E. Silva and N. Pompeo, *IEEE Transactions on Applied Superconductivity*, 2019, **29**, 1–5.

(85) H. Krauth, International Symposium Niobium, Orlando, Florida, U.S.A. 2001.

(86) T. Ishida and R. B. Goldfarb, *Phys. Rev. B*, 1990, **41**, 8937–8948.

(87) S. Tsuneyuki, H. Aoki, M. Tsukada and Y. Matsui, *Phys. Rev. Lett.*, 1990, **64**, 776–779.

List of Figures

List of Tables